MASTER THESIS

Magnetic properties of CrI_3 monolayers, bilayers and twisted bilayers

---

Author:
Maarten SOENEN

Supervisors:
Prof. Dr. Milorad MILOSEVIC
Dr. Cihan BACAKSIZ

*A thesis submitted in fulfillment of the requirements
for the degree of Master of Science in Physics*

at the

University of Antwerp
Faculty of Science
Department of Physics

August 23, 2021

UNIVERSITY OF ANTWERP

Abstract

Faculty of Science
Department of Physics

Master of Science in Physics

Magnetic properties of CrI_3 monolayers, bilayers and twisted bilayers

by Maarten SOENEN

Since the experimental observation of permanent magnetism in 2D CrI_3 in 2017, the field of 2D magnetic materials has gained a lot of interest within the material physics community. The extraordinary magnetic properties observed in CrI_3 create a lot of opportunities for both the discovery of interesting new physics and the development of innovative spintronic and magnonic device concepts. A current challenge within the field is to achieve perfectly tunable magnetic properties by manipulating the materials. In this thesis, we studied the effect of stacking and twisting of the layers in a CrI_3 bilayer on the properties of the material. The magnetism in the material is described by a Heisenberg spin model. We used a technique called four-state energy mapping, in combination with ab initio calculations using density functional theory, to determine the magnetic parameters that characterize the different terms of the Heisenberg Hamiltonian. These magnetic parameters were determined for the CrI_3 monolayer and for the CrI_3 bilayer in three different stacking orders. Further, we also determined the Curie temperature for all these structures. Our calculations suggest a dependency of the strength of the inter-layer exchange coupling, the presence of spin canting due to the Dzyaloshinkii-Moriya interaction and the Curie temperature, on the stacking order of the layers. In addition, we were able to show that it is possible to tune the intra-layer exchange interaction, the inter-layer exchange interaction and the inter-layer Dzyaloshinkii-Moriya interaction by twisting one of the layers in a bilayer.

UNIVERSITEIT ANTWERPEN

Abstract (Dutch - Nederlands)

Faculteit Wetenschappen
Departement Fysica

Master in de Fysica

Magnetische eigenschappen van CrI_3 monolagen, dubbellagen and gedraaide dubbellagen

door Maarten SOENEN

Sinds de experimentele ontdekking van permanent magnetisme in 2D CrI_3 in 2017, is de interesse in het onderzoek naar de eigenschappen van 2D magnetische materialen aanzienlijk toegenomen. De uitzonderlijke magnetische eigenschappen van CrI_3 scheppen mogelijkheden voor de ontdekking van interessante nieuwe fysica en voor de ontwikkeling van innovatieve spintronica en magnonica applicaties. Een van de huidige uitdagingen in dit onderzoeksveldveld bestaat erin de magnetische eigenschappen van de materialen te kunnen manipuleren. In deze thesis, bestuderen we het effect van de stapeling en het draaien van lagen in een CrI_3 dubbellaag op zijn magnetische eigenschappen. Het magnetisme in het materiaal wordt beschreven door middel van het Heisenberg spin model. We gebruiken de ′four-state energy mapping′ techniek in combinatie met ab initio berekeningen gebaseerd of dichtheids functionaal theorie om de magnetische parameters te bepalen die de verschillende termen in de Heisenberg Hamiltoniaan karakteriseren. De magnetische parameters zijn bepaald voor de CrI_3 monolaag en de CrI_3 dubbellaag in drie verschillende stapelingen. Daarnaast, hebben we ook de Curie temperatuur bepaald voor al deze structuren. Onze berekeningen suggereren een afhankelijkheid van de ′exchange′ interactie tussen de lagen, de mogelijk van de spins om te kantelen als een gevolg van de Dzyaloshinkii-Moriya interactie en de Curie temperatuur, op de stapeling van de lagen. Daarnaast tonen we ook aan dat het mogelijk is om de ′exchange′ interactie binnen eenzelfde laag, de ′exchange′ interactie tussen twee lagen en de Dzyaloshinkii-Moriya interactie tussen twee lagen, te manipuleren door het draaien van een van de lagen in een dubbellaag.

Acknowledgements

Before we start with the actual thesis, I would like to thank a few people whom I had the pleasure to collaborate with during the last couple of months. First and foremost, I want to thank prof. Milosevic for giving me the opportunity to work on an interesting topic and for his useful comments to improve the thesis. Further, I want to thank Cihan for sharing his knowledge and insights on the thesis topic, and for always being available to answer questions or give advice. Also, a big thank you to Rai for his help to get started with the Spirit software and for sharing some useful insights on this matter.

This thesis concludes the fifth and final year of my physics education. Finally, I want to thank everyone, especially my friends and classmates, that made the past five years an unforgettable period of my life (perhaps with the exception of the last year and a half which I would like to forget asap). I will cherish these friendships and memories forever.

Contents

List of Figures

List of Tables

List of Abbreviations

CrBr$_3$	**C**h**r**omium(III)**Br**omide
CrCl$_3$	**C**h**r**omium(III)**Cl**oride
CrI$_3$	**C**h**r**omium(III)**I**odide
hBN	**h**exagonal **B**oron **N**itride
MnSe$_2$	**M**anganese(IV)**Se**lenide
MoSe$_2$	**Mo**lybdenum(IV)**Se**lenide
MoS$_2$	**Mo**lybdenum(IV)**S**ulfide
VSe$_2$	**V**anadium(IV)**Se**lenide
WSe$_2$	Tungsten(IV)**Se**lenide

1D	**One**-**D**imensional
2D	**Two**-**D**imensional
3D	**Three**-**D**imensional
4SM	**Four**-**S**tate **M**apping
AFM	**A**nti-Ferro**M**agnetic
DFT	**D**ensity **F**unctional **T**heory
DMI	**D**zyaloshinskii-**M**oriya **I**nteraction
DOS	**D**ensity **O**f **S**tates
FM	Ferro**M**agnetic
GGA	**G**eneralized **G**radient **A**pproximation
HPC	**H**igh **P**erformance **C**omputing
HT	**H**igh **T**emperature
LCAO	**L**inear **C**ombinations of **A**tomic **O**rbitals
LLG	**L**andau-**L**ifshitz-**G**ilbert
LT	**L**ow **T**emperature
L(S)DA	**L**ocal (**S**pin-)**D**ensity **A**pproximation
MAE	**M**agnetic **A**nisotropy **E**nergy
MOKE	**M**agneto-**O**ptical **K**err **E**ffect
PAW	**P**rojector **A**ugmented **W**ave
PBE	**P**erdew-**B**urke-**E**rnzerhof
RMM-DIIS	**R**esidual **M**inimization **M**ethod - **D**irect **I**nversion in the **I**terative **S**ubspace
SCF	**S**elf-**C**onsistent **F**ield
SIA	**S**ingle-**I**on **A**nisotropy
SOC	**S**pin-**O**rbit **C**oupling
SQUID	**S**uperconducting **Qu**antum **I**nterference **D**evice
TFET	**T**unnel **F**ield-**E**ffect **T**ransistor
VASP	**V**ienna **A**b initio **S**imulation **P**ackage
vdW	**v**an **d**er **W**aals
VSC	**V**laams **S**upercomputing **C**enter
XC	**E**xchange **C**orrelation

Chapter 1

Introduction

1.1 Magnetism in Flatland

The discovery of graphene as the first truly two-dimensional (2D) material sparked a significant interest in single-layered crystals[1]. Over the years, an explosion of new research resulted in a diverse family of materials with a wide variety of properties[2–4]. Magnetism, however, has long been a remarkable absentee on the list of experimentally observed properties. For quite some time, the presence of intrinsic magnetic order had been considered impossible in 2D due to the Mermin-Wagner theorem, which states that long-range order cannot survive temperature fluctuations in an isotropic system[5]. Recently, studies suggested that in certain 2D materials with a strong magnetocrystalline anisotropy, e.g. *Chromium(III)Iodide* (CrI_3)[6,7], the Mermin-Wagner restriction no longer holds, and consequently, that magnetization of materials at non-zero temperatures is allowed after all.

The first demonstration of 2D magnetism occurred in 2017 with the experimental confirmation of permanent magnetic order in atomically thin CrI_3[8]. Huang et al. found evidence for the presence of intrinsic ferromagnetism in mechanically exfoliated CrI_3 flakes by performing measurements based on the polar magneto-optical Kerr effect (MOKE). The MOKE, first described by J. Kerr in 1877, predicts a change in polarization of a beam of plane-polarized light that is reflected off a magnetized surface[9]. The magnetization curves produced in the experiment show a clear signature for magnetic order in all CrI_3 samples, even in the monolayer limit[8].

This discovery marks an important milestone for the exploration of magnetic 'flatland'[10]. Although numerous magnetic monolayers have been discovered since[4], CrI_3 is still one of the most studied systems as it shows great promise for the development of applications. In fact, initial research has already led to the realization of CrI_3 based devices[11,12]. Nevertheless, intrinsic magnetism in CrI_3 has only been observed at very low temperatures[8]. If we want devices that operate in realistic conditions, we need to find materials that preserve their magnetic properties at higher temperatures. Possible candidates are Manganese(IV)Selenide ($MnSe_2$) and Vanadium(IV)Selenide (VSe_2), two materials that show room-temperature ferromagnetism in the monolayer limit[13,14]. Aside from the temperature problem, tunability of magnetic properties has emerged as a second big challenge within the field. In this regard, CrI_3 continues to stand at the forefront of theoretical investigations due to its status as the archetypical- and best understood 2D magnet. The pioneering work done on CrI_3 can pave the road towards the achievement of perfectly tunable and controllable properties in magnetic materials.

In this thesis, we will investigate the magnetic properties of monolayer and bilayer CrI_3. We will determine some magnetic properties of these systems, and analyse if these properties can be tuned through twisting and stacking of the layers.

The goal of this first chapter, is to motivate our interest in CrI_3 through a discussion of its most important properties and the exploration of some emerging device concepts. We start off with a section that summarizes some important background information that the reader might need to develop a good understanding of the phenomena at hand. We give a brief introduction to world of 2D materials and introduce some important concepts like heterostructures and *Moiré patterns*. Afterwards, we list some important facts and figures about CrI_3. Further, we review the interactions that lie at the origin of magnetism in 2D CrI_3, introduce the concept of spin waves and discuss why the existence of 2D magnetism doesn't violate the Mermin-Wagner theorem. In a second section, we demonstrate the relevance of 2D magnetic materials by discussing some prospects for magnetism based applications. In the final section of this chapter, we give a brief overview of how the thesis is organized.

1.1.1 Monolayers, Multilayers and Heterostructures

Crystalline CrI_3 belongs to the family of van der Waals (vdW) solids. This type of crystal features single-atom-thick or polyhedral-thick layers of atoms with covalent- or ionic in-plane bonding[3]. The layers themselves are weakly bound together by short-range vdW forces, hence the name of the material. Due to the weak interaction between the layers, it's relatively easy to produce thin samples or even monolayers using — Scotch tape — mechanical exfoliation[3].

The first truly 2D material that has been produced with the Scotch tape technique is graphene[1]. For their work on graphene, A. Geim and K. Novoselov eventually even won a Nobel prize in 2010. Not long after the discovery of graphene, more and more 2D materials were successfully synthesized. Other notable 2D materials include for instance hexagonal boron nitride (hBN), silicene or the transition metal dichalcogenides, e.g. molybdenum(IV)sulfide (MoS_2). Notice that a material doesn't need to be atomically thick, like graphene or hBN, in order to be considered a 2D material. Monolayers of materials like MoS_2 and CrI_3 actually consist out of three atomic layers but we still call them 2D since they can't be made any thinner than they already are, and they are periodic in only 2D.

Monolayers can be seen as the building blocks to construct other materials. By stacking multiple layers of the same material on top of each other, you can construct multilayer structures. By varying the stacking order of these layers, you change not only the symmetry of the material but you might also change some of its properties. One of the things that we will investigate in this thesis, is how the stacking of a CrI_3 bilayer changes its magnetic properties.

When building new structures by stacking monolayers on top of each other, we don't necessarily need to limit ourselves to layers of the same material. It is possible to build stable structures by stacking layers of different materials on top of each other. In practice, this stacking of layers can be achieved by experimental techniques, e.g. molecular beam epitaxy[15]. Since these newly formed crystals consist out of different materials held together by vdW forces, they are conveniently called *vdW heterostructures*. The combination of materials with different properties in a heterostructure leads to new functionalities to be exploited in experiments or future applications. It's very important to develop a good understanding of the interplay between different materials since 2D materials are, in most realistic applications, integrated in a vdW heterostructure. A phenomenon in which it becomes clear that the functionalities of a layered crystal are heavily influenced by the physical properties of its neighbouring layers, is the magnetic proximity effect. For example, the proximity of a magnetic CrI_3 layer to the semiconductor tungsten(IV)selenide (WSe_2) has

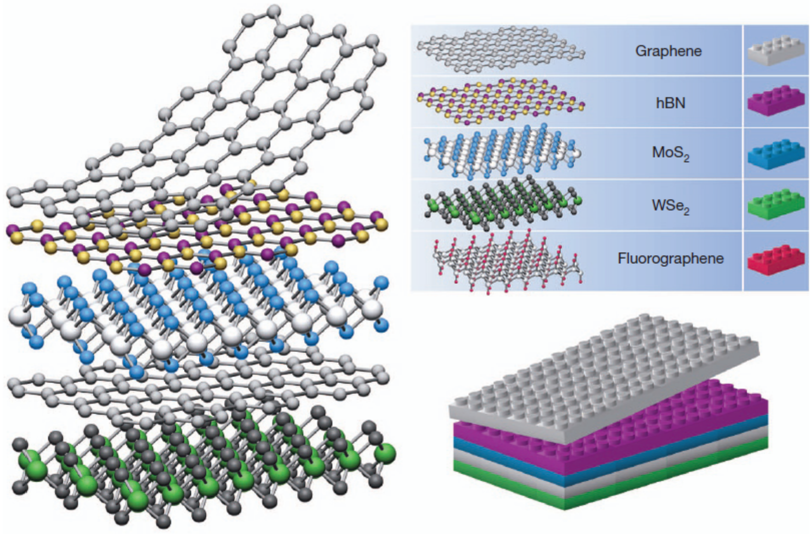

FIGURE 1.1: **Building van der Waals heterostructures.** A vdW heterostructure containing graphene, hBN, MoS_2 and WSe_2 monolayers. The different monolayers are building blocks that can be stacked in a lego-like fashion to create new structures. Figure from: [15].

been shown to result in valley splitting and increased electrostatic control[11]. This type of material design is also known as heterostructure engineering. An example of a vdW heterostructure containing multiple materials is shown in figure 1.1.

The difference in lattice constant between different materials included in a heterostructure, often gives rise to a lattice mismatch. A lattice mismatch is the relative ratio between the lattice constants of both layers. In multilayers or vdW heterostructures, Moiré patterns arise due to a lattice mismatch and/or twisting of layers[16]. 'A Moiré pattern is the geometrical design that results when a set of straight or curved lines is superposed onto another set'[17]. A Moiré pattern introduces additional, large-scale, periodicity to the system over a distance of multiple unit cells. The larger lattice we use to describe this periodicity is called the Moiré superlattice[16]. Moiré patterns result in local-to-local variations of the stacking order, which could result in local differences of material properties. The study of Moiré patterns in vdW heterostructures is a relatively new field, but one that shows a lot of promise. Especially heterostructures based on graphene and hBN raise a lot of interest within the material science community.

The introduction of Moiré patterns in materials can be a way of tuning their electronic properties. This approach to heterostructure engineering is sometimes referred to as twistronics. In recent years, this approach has grown into a hot topic in the field of material science and has led to some interesting results. For example, in twisted — magic-angle — bilayer graphene (see figure 1.2) twisting and additional doping can tune the material from semi-metallic to Mott-insulating and even to superconducting states[18]. In graphene/hexagonal boron nitride (hBN) heterostructures like encapsulated graphene similar opportunities for gap engineering and tunable superconductivity have been discovered[19].

In magnetic materials, the introduction of Moiré patterns are expected to break the inversion symmetry and might, therefore, result in non-collinear spin configurations. In extreme cases, there is a possibility that Moiré patterns could even lead to 'exotic' magnetic states, like for instance *magnetic skyrmions* (see section 1.1.5), that could have utility in spintronic applications[16].

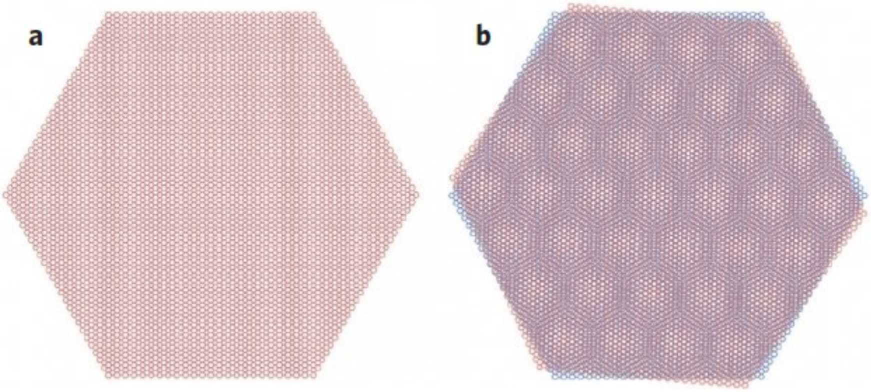

FIGURE 1.2: **Moiré pattern in twisted bilayer graphene.** Crystal structures of bilayer graphene without a twist (a) and with a twist of 1.1°, the so-called magic angle (b). Twisting one of the layers introduces a Moiré pattern in the crystal. Figure from: [20].

1.1.2 CrI_3 in a Nutshell

CrI_3 belong to the transition metal trichalcogenides, these are compounds with a chemical formula of the form MX_3, in which M is a transition metal (e.g. Cr) and X are chalcogen atoms (e.g. I). Like the formula suggests, the atoms occur in a 1:3 ratio in the crystal. Other transition metal trichalcogenides include for example chromium(III)bromide $CrBr_3$ and chromium(III)chloride $CrCl_3$.

As mentioned earlier, CrI_3 is a vdW material with a layered structure. The structure of bulk CrI_3 is depicted in figure 1.3b. The bulk structure consists out of many monolayers stacked on top of each other. A monolayer consists out of a layer of chromium atoms sandwiched between two layers of iodine atoms. Each chromium atom is octahedrally coordinated to six iodine atoms. Notice that there are only bonds between the chromium and iodine atoms, i.e. there are no Cr-Cr and I-I bonds. Each iodine atom is bound to two chromium atoms. The Cr-I-Cr bond angle is approximately $\approx 90°$. Since, the layers are only bound by relatively weak vdW forces, it's not too hard to produce CrI_3 flakes using mechanical exfoliation. A flake that has been produced in an actual experiment is shown in figure 1.3a. On the optical contrast map on the right of this figure, the thickness of the flake is numbered. A fairly big part of the flake is only one layer thick, this proves that single-layered CrI_3 is a stable compound.

For bulk CrI_3, there are two stable crystal structures that have been successfully synthesized and studied in experiments. At low temperature (LT), i.e. lower than 210 K, CrI_3 has a rhombohedral structure (space group $R\bar{3}$), at high temperature (HT), the structure is monoclinic (space group $C2/m$)[6]. The stacking order of these two phases will be discussed in more detail in chapter 4 where we discuss the CrI_3 bilayer.

MOKE measurements performed on bulk CrI_3 show hysteresis in the magnetization, a hallmark for ferromagnetism (see figure 1.3c). The hysteresis loop has a nonzero remnant magnetization in the absence of an externally applied magnetic field which is indicative for ferromagnetic (FM) order[8]. Similar measurements performed on a CrI_3 monolayer show that the hysteresis persists down to the 2D limit[8]. In the 2D case, the hystersis loop has an even bigger coercive field which suggests that the monolayer is a permanent ferromagnet while bulk CrI_3 is a soft ferromagnet[8]. The latter means that the material will become magnetized when an external magnetic field is applied, but doesn't tend to stay magnetized when the magnetic field

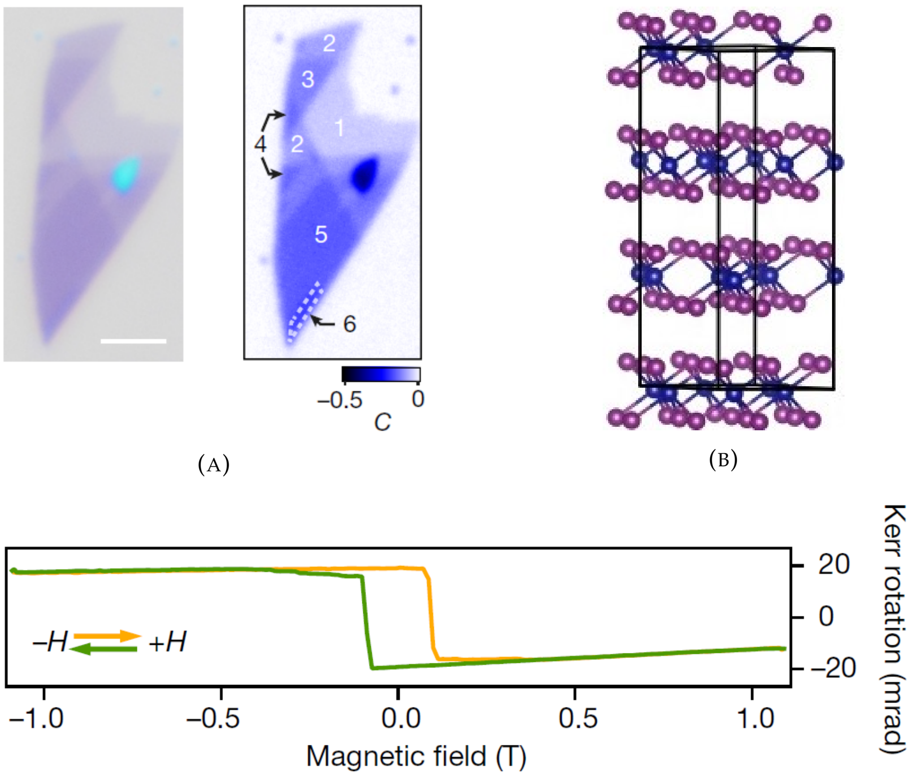

(A)

(B)

(C)

FIGURE 1.3: **Crystal structure and hysteresis of CrI_3.** (A) A CrI_3 flake that has been produced by mechanical exfoliation. The left picture depicts an optical micrograph of the flake. The right picture depicts an optical contrast map with a 631-nm optical filter. The scale bar in the left figure is equal to 3 μm. Figure from reference: [8]. (B) Layered crystal structure of bulk CrI_3. Chromium- and iodine atoms are depicted with blue and purple spheres respectively. The unit cell is marked with black lines. The figure is drawn with the VESTA software. (C) MOKE signal of a thin bulk CrI_3 sample. The hysteresis in the Kerr rotation is clear proof for presence of intrinsic ferromagnetism in CrI_3. Figure from reference: [8].

is switched off. The same paper also claims that bilayer CrI_3 is anti-ferromagnetic (AFM) in its ground-state[8] which is true for some possible stacking orders of the layers but not all of them, more on this matter can be found in chapter 4. Superconducting quantum interference device (SQUID) magnetometery measurements predict a saturation magnetization of 3.0 μ_B/Cr atom[6], here μ_B is the Bohr magneton. This means that the atomic spin is equal to 3/2. Temperature dependence of MOKE signals place the Curie temperature of monolayer CrI_3 at T_c = 45 K[8], which is slightly smaller than the bulk value of T_c = 61 K measured with SQUID magnetometry[6].

Below its Curie temperature, the CrI_3 monolayer displays strongly anisotropic, FM behaviour with an out-of-plane spin polarization[8]. The direction of the spin polarization is explained by the magnetocrystalline anisotropy, which creates an easy axis for the magnetization perpendicular to the atomic plane[7]. As will be discussed in the next two sections, the presence of a strong magnetocrystalline anisotropy is a ’conditio sine qua non’ for the existence of permanent magnetism in monolayers. After all, in the absence of anisotropy, permanent magnetism would be prohibited by the Mermin-Wagner theorem[5].

1.1.3 Origin of 2D Magnetism

We call a material magnetic, when the atomic magnetic moments[*] posses a well determined spatial ordering. If the magnetic moments have a parallel orientation, the material is FM, if the moments are aligned anti-parallel, we call the system AFM. Measurements performed with the MOKE confirm that monolayer CrI_3 displays strongly anisotropic, FM behaviour with an out-of-plane spin polarization[8]. This FM order results from the interplay between several different mechanisms. In this section, we will discuss the most important interactions that contribute to the realization of magnetism in 2D materials, and to CrI_3 in particular.

Exchange Interaction

The dominant interaction in magnetic materials is the *symmetric exchange interaction*. The origin of this interaction can be understood through the Pauli exclusion principle, which states that it's impossible for two fermions, e.g. electrons, to simultaneously occupy the same quantum state[21]. This is due to the fact that the wave function of fermionic systems has to be antisymmetric with respect to the exchange of two electrons[21]. The possible electronic configurations in atoms and solids are, thus, limited to the states that don't violate the Pauli exclusion principle. This effect occurs both intra-atomic, where it determines the atomic spin, and-inter atomic, where it determines the magnetic coupling between different atoms.

Intra-atomic, the exclusion principle causes electrons with parallel spin to occupy different atomic orbitals. By occupying different orbitals, the Coulomb repulsion between the electrons will also be minimized[21]. Therefore, the lowest energy state of an atom will be the state with the maximum number of unpaired valence electrons with parallel spin, this fact is also known as Hund's first rule. The unpaired electrons give rise to a net atomic spin $\mathbf{S}$ through formula $\mathbf{S} = \sum_i \mathbf{s}_i$, with $\mathbf{s}_i$ the electron spin. In summary, the spin of an atom is determined by the spins of its (unpaired) electrons.

In materials, there will also be an exchange interaction between electrons of different atoms. The exchange interaction between neighbouring atoms due to the overlap of atomic orbitals is known as the *direct exchange* interaction[21,22]. The occupation of the respective overlapping orbitals will determine whether the interaction will be FM or AFM[22]. Nearly filled or nearly empty shells will tend to give rise to a FM coupling, half filled shells result in an AFM coupling[22].

If the magnetic atoms aren't neighbours, e.g. the chromium atoms in CrI_3, or when the electrons are strongly localized around an atom, there will only be a very small overlap of the atomic orbitals and, thus, only a minor contribution due to the direct exchange interaction[21]. In such cases, the dominant magnetic interaction is the *indirect exchange interaction*, also called the *superexchange*[21]. This interaction is called 'indirect' because it involves a third non-magnetic atom that is bound to both magnetic atoms[21], e.g. the iodine atom in CrI_3. Orbitals of both magnetic atoms (e.g. Cr) will now overlap with the orbitals of the non-magnetic atom (e.g. I). In contrast, the direct overlap between the orbitals of the magnetic atoms (e.g. Cr) will be negligible small or even non-existent. The superexchange coupling can be both FM or AFM depending on the orbital occupation, the interatomic separation and the bond

---

[*] Throughout this work, we use both the magnetic moment $\mathbf{m}$ and the spin $\mathbf{S}$ interchangeably to talk about magnetic order. Both variables are related through formula $\mathbf{m} = -2\,(\mu_B/\hbar)\,\mathbf{S}$, with μ_B the Bohr magneton and $\hbar$ the reduced Planck constant. Due to the minus sign in this expression, the magnetic moment and the spin have an opposite orientation. It's important to take this into account when contemplating the direction of the magnetization.

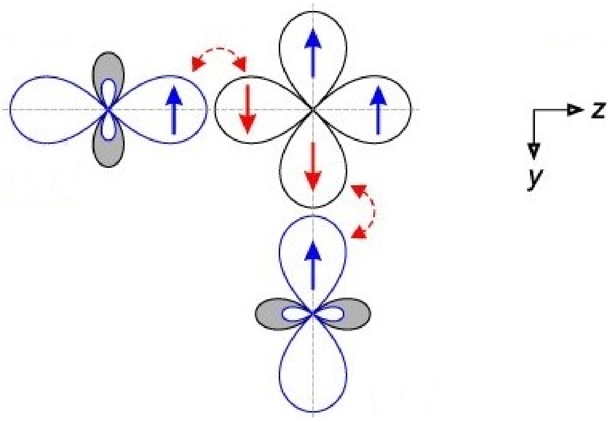

FIGURE 1.4: **Superexchange interaction along a 90° M-X-M bond.** The exchange interaction between partially filled d-orbitals of two magnetic atoms and p-orbitals of a non-magnetic intermediate atom gives rise to an indirect FM coupling between the magnetic atoms. Figure from reference: [23].

angle, the latter determines which atomic orbitals will be overlapping[21,22]. When the bond angle is approximately 90°, like in $\mathrm{CrI_3}$, the overlap of magnetic, partially filled, d-orbitals and non-magnetic p-orbitals will give rise to an overall FM coupling between the magnetic atoms. The latter is illustrated in figure 1.4 for the d-orbitals of two transition metals (M) and the p-orbitals of an intermediate chalcogen atom (X) in a 90° M-X-M bond. The interaction between the magnetic atoms (blue) and the non-magnetic atom (red) will be AFM, the electrons in the overlapping orbitals need to have opposite spin otherwise they would repel each other. As a result, the spins of both magnetic atoms (blue) have the same orientation, i.e. the are coupled FM. In $\mathrm{CrI_3}$, the FM superexchange will be the main source of the exchange interaction which explains why 2D $\mathrm{CrI_3}$ is a permanent ferromagnet[7].

The symmetric exchange interaction between the spins on the $\mathrm{i^{th}}$ and $\mathrm{j^{th}}$ spin sites can be modelled by the fairly simple formula[22]:

$$\begin{aligned}\hat{\mathcal{H}}_{\mathrm{EX}} &= \sum_{i<j} \mathcal{J}_{ij} \hat{\mathbf{S}}_i \cdot \hat{\mathbf{S}}_j \\ &= \sum_{i<j} \left[\mathcal{J}^x_{ij} \hat{S}^x_i \hat{S}^x_j + \mathcal{J}^y_{ij} \hat{S}^x_i \hat{S}^y_j + \mathcal{J}^z_{ij} \hat{S}^x_i \hat{S}^z_j \right], \end{aligned} \tag{1.1}$$

in which the spins are three-dimensional (3D) vectors $\hat{\mathbf{S}}_i = (\hat{S}^x_i, \hat{S}^y_i, \hat{S}^z_i)$ expressed in Cartesian coordinates, and the exchange parameters $\mathcal{J}^\alpha_{ij}$ are constants with $\alpha = x, y, z$. If the exchange constant is $\mathcal{J}^\alpha_{ij} < 0$ the interaction is FM, if its value is $\mathcal{J}^\alpha_{ij} > 0$ the interaction is AFM. In some papers, the exchange interaction is written with an extra minus sign, in this case also the sign of the exchange constant for the FM and AFM cases will be opposite. The exchange parameters have the units of energy. We write $i < j$ in the summation to avoid self-interaction and double counting of spins.

Dzyaloshinskii–Moriya interaction

The *antisymmetric exchange interaction*, more often called the *Dzyaloshinskii–Moriya interaction* (DMI), is a higher-order effect occurring between ions already coupled by superexchange[22]. As such, it's a three-site interaction between two atomic spins, $\mathbf{S}_i$ and $\mathbf{S}_j$, and a neighbouring atom with a large spin-orbit coupling (SOC). The

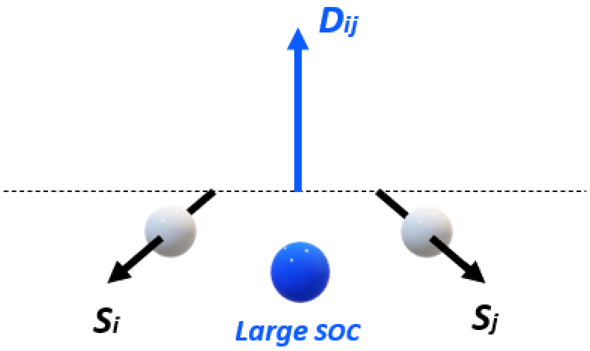

FIGURE 1.5: **Schematic representation of the DMI.** The interaction is generated by an indirect exchange interaction between two atomic spins through a neighbouring atom with a large SOC. Both atomic spins undergo a slight rotation. The DMI-vector is oriented perpendicular to the plane containing the spins.

resulting DMI-vector $\mathbf{D}_{ij}$ is pointed perpendicular to the plane containing the two atomic spins. The symmetric exchange interaction between the spins on the i^{th} and j^{th} spin sites can be modelled by the expression[22]:

$$\hat{\mathcal{H}}_{DMI} = \sum_{i<j} \mathbf{D}_{ij} \cdot (\hat{\mathbf{S}}_i \times \hat{\mathbf{S}}_j). \tag{1.2}$$

Again, we write $i < j$ in the summation to avoid self-interaction and double counting of spins. In a system that lacks inversion symmetry, or where the symmetry is broken, the DMI will try to force $\mathbf{S}_i$ and $\mathbf{S}_j$ to take on an orthogonal orientation with respect to vector $\mathbf{D}_{ij}$ as well as each other[21]. In practice, this results in spin canting, i.e. a slight rotation of the spins around a rotational axis parallel with vector $\mathbf{D}_{ij}$[21]. Usually, the spins will not make the full rotation to an orthogonal configuration due to the competing, and dominant, symmetric exchange interaction that strives for a parallel or anti-parallel orientation. In anti-ferromagnets, spin canting due to the DMI can result in a small FM component perpendicular to the spin axis, this effect is known as weak ferromagnetism[24,25]. The effect of the DMI on two atomic spins is displayed schematically in figure 1.5.

When there is inversion symmetry in the system, there will be no net effect of the DMI and the DMI-vector will vanish[21]. This is the case in $\mathrm{CrI_3}$ layers[7]. Each pair of chromium atoms is connected through two Cr-I-Cr bonds. These two paths each contribute to a DMI-vector with opposite sign resulting in a zero net contribution[7]. It is expected that breaking of the inversion symmetry in $\mathrm{CrI_3}$, e.g. by lattice straining, introduction of defects, stacking of the layers in a multilayer, applying external fields, etc., will result in a non-zero net DMI-vector. The DMI is the main culprit that enables the existence of non-collinear spin configurations like magnetic skyrmions. However, when the DMI is only small and non-uniform, no skyrmions will appear in the lattice and the only effect of the DMI will be spin canting.

It is possible to write the symmetric exchange interaction and the DMI in one term. Let's include both term (1.1) and (1.2) in one expression:

$$\begin{aligned} \hat{\mathcal{H}}_{EX} &= \sum_{i<j} \mathcal{J}_{ij} \hat{\mathbf{S}}_i \cdot \hat{\mathbf{S}}_j + \sum_{i<j} \mathbf{D}_{ij} \cdot (\hat{\mathbf{S}}_i \times \hat{\mathbf{S}}_j) \\ &= \sum_{i<j} J_{ij} \hat{\mathbf{S}}_i \cdot \hat{\mathbf{S}}_j. \end{aligned} \tag{1.3}$$

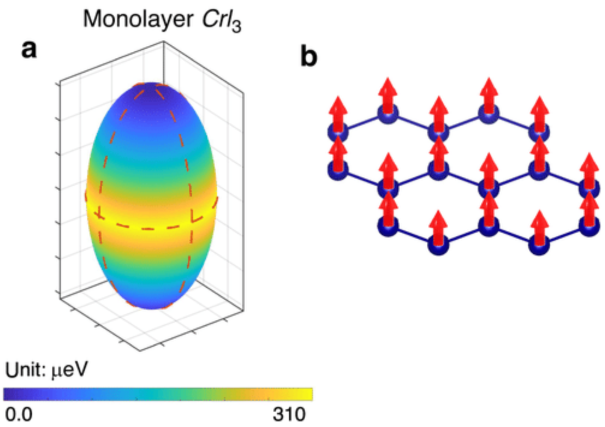

FIGURE 1.6: **Magnetic anisotropy energy of a CrI_3 monolayer.** The anisotropy energy as a function of the spin orientation is shown in (a). The out-of-plane direction is taken as a reference. The energetically most favourable configuration occurs when all the spins are aligned along the out-of-plane easy axis, as shown in (b). Figure from: [26].

Notice that J_{ij} is now a 3×3 matrix. The diagonal elements contain the parameters associated with symmetric exchange, the off-diagonal elements are associated with the DMI. More information on how to calculate the DMI parameters out of the matrix elements of the exchange matrix is given in section 2.1.3.

Magnetic Anisotropy

The symmetric exchange interaction will cause atomic spins to align parallel or antiparallel to the magnetic axis. But what will determine the direction of this magnetic axis? The answer is found in the *magnetic anisotropy* of a material[22]. This anisotropy will create one or more, energetically favourable, easy axes for the magnetization[22]. As an example, we show in figure 1.6 that a CrI_3 monolayer has an out-of-plane magnetic anisotropy, i.e. the magnetic anisotropy energy (MAE) is minimized when the spins point in the out-of-plane direction.

The anisotropy is determined by a few different contributions. On a micro-scale, the anisotropy is influenced by properties like the shape and composition of a sample, and the presence of external forces and stresses on the material[22]. The main contribution, however, results from the crystal structure on the atomic scale and is called the *magnetocrystalline anisotropy*[22]. The latter will be the most important contribution for an atomic scale description of magnetism in materials.

The lowest order contribution to the magnetocrystalline anisotropy is the *single-ion anisotropy* (SIA)[22]. The SIA is caused by the crystal-field and the SOC. The crystal-field, determined by the specific atomic positions in the crystal structure, will tend to stabilize particular atomic orbitals[22]. This field, thus, leads to a preferential direction of the orbital moment **L**. The spin **S** will now also align along a preferential direction, i.e. one of the easy axes, as to minimize the (large) SOC of the material, which is a positive interaction for less than half-filled shells[22]. Since the SOC is proportional to $\propto \lambda \mathbf{L} \cdot \mathbf{S}$ with $\lambda > 0$, the easy axis for the magnetization will lie orthogonal to the orbital stabilized by the crystal-field. The MAE due to the SIA scales as[7]:

$$E_{MAE} \propto \lambda \langle \mathbf{L} \rangle \cdot \langle \mathbf{S} \rangle + \frac{\lambda^2}{\Delta} + \frac{\lambda^4}{\Delta^3}, \tag{1.4}$$

with Δ the energy separation with the crystal-field excited states of the magnetic ion. In CrI_3, the orbital moment is quenched (i.e. $\langle \mathbf{L} \rangle = 0$) which causes the lowest order term of equation (1.4) to vanish[7]. The second term arises from quantum fluctuations of the orbital moment and will also vanish in CrI_3 due to the purely octahedral environment of the chromium atoms[7]. If this symmetry is broken, e.g. by the introduction defects or strain in the lattice, this quadratic term can become non-zero. The remnant term in the MAE now scales as $\frac{\lambda^4}{\Delta^3}$ resulting in an extremely small SIA[7]. The SIA, thus, delivers only a minor contribution to the magnetic anisotropy of CrI_3[7].

Whereas the SIA results from the interaction of a single-ion with the crystal-field, the *two-ion anisotropy* is caused by the interaction of two neighbouring ions with each other. The two-ion anisotropy behaves very similarly to the dipole-dipole interaction, since it favours a head-to-tail spin configuration instead of a broadside one[22]. Each magnetic atom will generate a magnetic field that exerts a force on all other magnetic moments to try to align the moments with the field direction (cfr. demagnetization field)[22]. On an atomic scale, however, this effect is negligibly small. Only on larger, microscopic, scales the combined contribution of many magnetic moments will have an important influence on the magnetization of the material[22]. Through competition with the symmetric exchange interaction, this will for instance result in the formation of magnetic domains[22]. In 2D CrI_3, this magnetic dipolar interaction is not an important contribution since it favors an in-plane anisotropy and CrI_3 clearly possesses an out-of-plane one[7].

Another important contribution originates from anisotropy in the superexchange in the form of two interactions, namely the DMI and the anisotropic symmetric exchange interaction[7]. As discussed earlier, the contribution of the former will vanish in a CrI_3 due to the crystal's inversion symmetry. The latter is a higher-order contribution to the conventional symmetric exchange interaction and is described by formula $\lambda_s S_i^z S_j^z$ with $\lambda_s \neq 0$, otherwise the exchange interaction would be completely isotropic[7]. In CrI_3, this anisotropy in the superexchange is caused by the large SOC of the ligand iodine atoms[7].

In addition to explaining the the direction of the spin polarization, the magnetocrystalline anisotropy also explains why magnetism is possible in CrI_3 in the first place. In the next section, we explain how the presence of anisotropy makes sure the Mermin-Wagner theorem no longer holds. From the above discussion, it becomes clear that, since the SIA is suppressed by the octahedral environment, the anisotropic superexchange due to the (large) SOC of the iodine atoms is the leading mechanism that introduces anisotropy into the CrI_3 structure and, thus, enables the existence of 2D magnetism[7]. Although this anisotropy in the symmetric exchange interaction is the leading mechanism behind the magnetic anisotropy, we still opt to also include the small contribution due to the SIA in our model. The SIA interaction is included for each spin site $\mathbf{S}_i$, and is given by the following expression:

$$\hat{\mathcal{H}}_{SIA} = \sum_i A_{ii} \hat{\mathbf{S}}_i^2, \tag{1.5}$$

in which the SIA-matrix A_{ii} is a 3×3 matrix.

It should be noted that we don't necessarily require exactly the above three terms to accurately describe the magnetic properties of a certain system. Depending on the system, some terms can be omitted or added, e.g. a Zeeman term when an external magnetic field is applied ($\hat{\mathcal{H}}_Z = g\mu_B \sum_i \hat{\mathbf{S}}_i \cdot \mathbf{B}$), or more higher order terms of the exchange interaction. However, for the systems treated in this thesis, it suffices to only include aforementioned three terms in the Hamiltonian.

1.1.4 Mermin-Wagner Theorem

In 1966, Mermin and Wagner published a famous article that excludes the possibility of FM or AFM order in one-dimensional (1D) or 2D systems at finite temperatures[5]. Their theorem states that long-range magnetic order is not possible in 1D and 2D isotropic systems due to temperature induced excitations.

In the groundstate, the magnetization of a permanent magnet is fully saturated. Augmented temperature can diminish the magnetization by inducing excitations into the system[22]. One of the most elementary excitations that result from increased temperature are spin-waves[22]. When a spin gets excited and starts to oscillate (cfr. precession of the spins), the neighbouring spins will feel this oscillation and also start to oscillate. Like this, excitations can propagate through the material as waves in the magnetization, i.e. spin waves. A spin wave is, thus, a collective excitation of a magnetic material. A spin-wave can propagate through the lattice with wavevector $\mathbf{q}$ and energy $\varepsilon_{\mathbf{q}} = \hbar\omega_{\mathbf{q}}$[22]. Here $\hbar$ is the reduced Planck constant and $\omega_{\mathbf{q}}$ is the frequency. The wavevector and the frequency are related via the following expression[22]:

$$\hbar\omega_{\mathbf{q}} = 2\mathcal{J}S\left[Z - \sum_{i}^{Z} \cos \mathbf{q}\cdot\delta_i\right], \tag{1.6}$$

in which the sum runs over the Z vectors δ_i connecting the nearest neighbouring spin sites, factor $\mathcal{J}$ is the exchange constant between these spin sites and models the strength of the symmetric exchange interaction.

Spin-waves are quantized, the quasi particle associated with one quantum of a spin-wave is called a magnon. The total number of magnons excited at a temperature T is given by[22]:

$$\mathrm{n_m} = \int_0^\infty \frac{\mathcal{N}\left(\omega_{\mathbf{q}}\right) \mathrm{d}\omega_{\mathbf{q}}}{\mathrm{e}^{\hbar\omega_{\mathbf{q}}/k_B T} - 1}, \tag{1.7}$$

with k_B the Boltzmann constant and $\mathcal{N}\left(\omega_{\mathbf{q}}\right)$ the magnon density of states (DOS), which scales as $\omega_{\mathbf{q}}^{-1/2}$ in 1D systems, is constant in 2D systems, and varies as $\omega_{\mathbf{q}}^{1/2}$ in 3D systems. For 1D or 2D materials at finite temperatures, this integral will diverge (i.e. $\mathrm{n_m} \to \infty$)[22]. There are, thus, an infinite amount of excitations and as a result no magnetic order. In 3D systems, the integral does not diverge and magnetic order is possible at finite temperatures[22].

At first sight, the divergence of integral (1.7) poses an insurmountable obstacle for physicists eager to study magnetism in 2D. There is, however, a way out of this deadlock. Namely, this divergence only occurs in isotropic systems. When there is anisotropy in the system, there arises a gap in the spin-wave spectrum at $\mathbf{q} = 0$[22]. Due to formula (1.6), this gap also appears in the frequency spectrum. Consequently, the lower limit of the integration in (1.7) will now be greater than zero and therefore the divergence is avoided[22].

In conclusion, if there is anisotropy in the material, 2D magnetic order is still possible. After all, the Mermin-Wagner theorem only holds for isotropic systems. As discussed in the previous section, monolayer $\mathrm{CrI_3}$ has a strong out-of-plane magnetocrystalline anisotropy due to its SOC and, consequently, does show intrinsic magnetic behaviour[7]. This has been confirmed both theoretically[6] and experimentally[8].

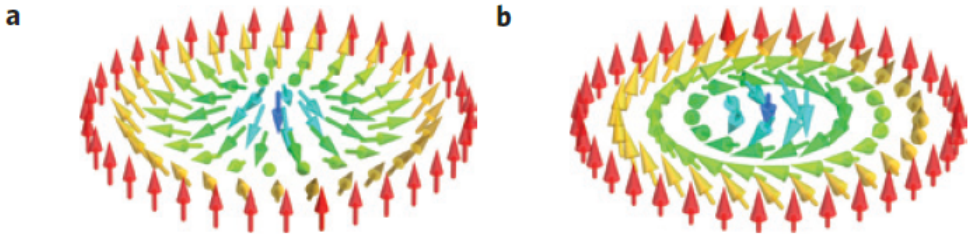

FIGURE 1.7: **Spin configurations in magnetic skyrmions.** Hedgehog skyrmion (a) and spiral skyrmion (b) in a 2D ferromagnet with uniaxial magnetic anisotropy along the vertical axis. Figure from: [29].

1.1.5 Magnetic Skyrmions

Earlier in this text, we briefly mentioned that DMI could potentially give rise to some 'exotic' spin configurations like magnetic skyrmions. Although skyrmions will not appear spontaneously in the systems under scrutiny in this thesis, they have already been observed in monolayer CrI_3 when an additional electric field is applied[27]. In this section, we will briefly summarize the most interesting properties of skyrmions since their presence in monolayer CrI_3 is a big motivator to obtain a better understanding of DMI in CrI_3.

Magnetic skyrmions are nanoscale spin configurations that can be formed in magnetic materials. They were named after Tony Skyrme, a particle physicist who contributed to the quantum field theory of interacting pions[28]. In the aftermath of the publication of his theory, the term 'skyrmion' was coined to describe topologically stable field configurations that appear as particle-like solutions[29]. Nowadays, the term is used to talk about mathematically similar objects in many different contexts, from particle physics to Bose-Einstein condensation to material science[29].

In a magnetic skyrmion, the spins will adopt a whirling configuration. They can be found in both achiral and chiral arrangements. These two forms are respectively called hedgehog skyrmions and spiral skyrmions. Other names used in literature are respectively Néel- and Bloch-type skyrmions, since skyrmions effectively are circular Néel- and Bloch-type domain walls[30]. Examples of both arrangements are depicted in figure 1.7 for the spins in a 2D ferromagnet with uniaxial magnetic anisotropy. We call an object chiral when it is distinguishable from its mirror image. The chirality — the intrinsic handedness — of magnetic skyrmions can be controlled and switched, which creates the potential for the inclusion of skyrmions in applications[31].

Skyrmions are often called topologically protected spin configurations[29]. This means that it's impossible to continuously deform the structure to another magnetic state[29]. In a skyrmion, the spins form a continuous field. If you want to change the magnetization of the material to another — non-skyrmionic — magnetic state, you will need to introduce a discontinuity to the spin field[30] which requires a finite amount of energy. In other words, you will need to overcome an energy barrier to change the magnetic phase of the material. Skyrmions, thus, occur as stable or metastable states of a material. Research shows that the height of this topological energy barrier is proportional to the strength of the symmetric exchange interaction[30].

In the continuum approximation we we can characterize a skyrmion by its topological charge[32]:

$$Q = \frac{1}{4\pi} \int \int \boldsymbol{M} \cdot \left(\partial_x \boldsymbol{M} \times \partial_y \boldsymbol{M} \right) dxdy, \tag{1.8}$$

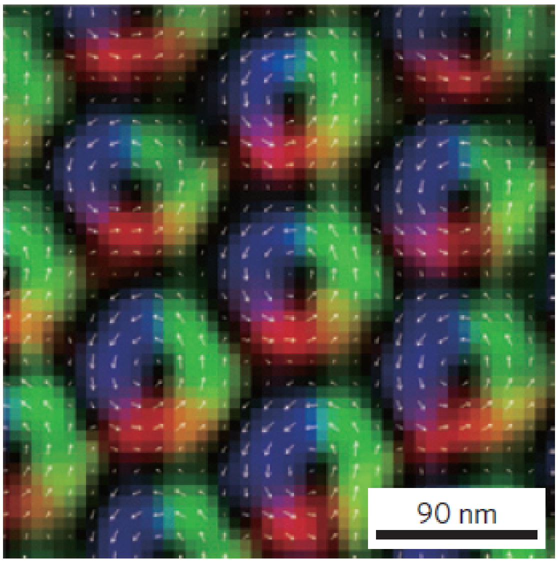

FIGURE 1.8: **Lorentz microscopy image of a skyrmion lattice.** The skyrmions are of the spiral-type and were observed in a 2D ferromagnet with an uniaxial magnetic anisotropy along the vertical axis. Figure from reference: [29].

with $\boldsymbol{M}(x, y)$ the reduced magnetization. The topological charge or skyrmion number is an integer that indicates how many times the spins wind around when projected onto a unit sphere. If $Q \neq 0$ we call the spin configuration topologically non-trivial, i.e. a skyrmion or another topologically protected spin texture is present[33]. On the other hand, when $Q = 0$ the material has a uniform or trivial spin configuration e.g. a FM one[33].

In most cases investigated up until now, magnetic skyrmions originate in crystals where DMI is present[29]. The lack- or breaking of inversion symmetry in layered magnetic materials, i.e. the creation of Moiré patterns, could possibly result in a non-zero DMI[29]. When the DMI is sufficiently large, this could result in the creation of skyrmions in the lattice[29]. However, in a lot of materials skyrmions won't appear spontaneously since they require a uniform DMI in the material and, therefore, we need to apply an extra electric- or magnetic field to introduce them. However, the non-zero DMI could give rise to spin canting or perhaps other spin textures. Due to the crystal periodicity, skyrmions can arise on multiple sites in a material with a certain periodicity, i.e. they can form a skyrmion lattice (see figure 1.8). The DMI is a chiral interaction, the chirality of the DMI will determine the chirality of the skyrmion.

If we want to use skyrmions as information carriers in devices (see section 1.2), we need to be able to move them at low energy costs. Recently, both a current-induced rotation and motion of skyrmion lattices has been observed in experiments[29]. The current densities that are required to move skyrmion lattices are very small, i.e. 10^6 A/m^2, which is a factor 10^5 to 10^6 smaller than the current needed to move magnetic domain walls[29]. According to micromagnetic simulations, the motion of individual skyrmions should also be possible but this has not yet been observed experimentally[29]. Although, a lot of research still has to be done before skyrmions can be integrated in actual applications, the first results definitely look promising.

1.2 Magnetic Monolayers in Action

Due to their interesting properties, magnetic monolayers show great promise for inclusion in applications. In this section, we first discuss how the magnetism in these materials can be controlled and tailored to match specific requirements. Afterwards, we examine some potential applications where we can see 2D magnetism in action.

1.2.1 Tailoring of Magnetic Properties

While designing applications, we sometimes want to enhance or control certain properties or effects in materials. Materials used in devices often require a very specific set of properties to guarantee an optimal performance of the application. To meet demand, scientist came up with several methods to tune the properties of materials. Here, we briefly summarize some of these methods that have been applied to tune the magnetism in CrI_3.

The electronic- and magnetic properties of solids are often heavily depended on the crystal structure. Both the symmetry and composition of a crystal can influence the magnetism of the material. Studies have shown that there is a clear coupling between the crystal structure and magnetism in CrI_3[6]. Also, from our discussion on the origin of 2D magnetism (see section 1.1.3), it becomes clear that all important magnetic interactions — i.e. superexchange, DMI and magnetocrystalline anisotropy — are in one way or another dependent on the crystal structure. In scientific literature on CrI_3, we find several examples were a change in the crystal structure resulted in a change of the magnetic order. For example, applying strain on a CrI_3 monolayer can introduce magnetic phase transitions[34]. The ground state of 2D CrI_3 is FM under compression, but becomes AFM under tension[34]. Studies have also shown that introducing atomic-scale defects in the crystal structure of a CrI_3 monolayer, most notably vacancies, can drive local FM to AFM phase transitions[35]. This is due to the lattice distortions that result from the defects[35]. The magnetism of CrI_3 also depends on the stacking order of the layers. Depending on how the layers are stacked, a CrI_3 bilayer will have either a FM- or an AFM ground-state. We will discuss this in more detail in chapter 4. Also, combining layers of different materials in a heterostrcuture can influence the functionalities of a material, e.g. the magnetic proximity effect or the creation of Moiré patterns due to a lattice mismatch. As mentioned earlier, we can also create Moiré patterns by twisting one or more layers in a structure.

Tailoring of magnetic properties can occur not only by internal changes in the crystal structure but also by applying external forces like electric- and magnetic fields. It is for instance well known that magnetic moments will try to align themselves with magnetic fields as to minimize their energy. In bilayer CrI_3, an external magnetic field can convert an AFM order to a FM one by flipping the spins in one of the layers[8]. To achieve such a magnetic phase transition one needs a very strong magnetic field which is often impractical in applications. Research shows that applying electric fields can lower the magnetic field needed to achieve such phase transitions, and in some cases even make the need for a magnetic field redundant[36,37]. The electric field control of magnetism will prove to be an indispensable concept when trying to understand some of the devices that we discuss further on in this chapter. Hence, let's analyse this effect in a little more detail.

1.2.2 Control of Magnetism by Electric Fields

One of the most effective ways we can tailor the magnetism in materials is by applying an electric field, this is often called gating[36]. The conventional way to achieve gate-controlled magnetism is by depositing a conducting material above and below the magnetic layer to serve as gates[36]. When the two gates have an opposite polarity, they impose an electric field perpendicular to the magnetic layer with a magnitude proportional to the voltage difference. No net charge will accumulate on the magnetic layer. Alternatively, when the gate voltages have the same polarity, the electric field can be made to vanish and charge can accumulate on the layer. Depending on the sign of the voltages these charges will either be electrons or holes. This accumulation of charge carriers is called electrostatic doping of the material. Research shows that electrostatic doping can reduce the magnetic field needed to switch from an AFM to the a FM state in bilayer CrI_3[37]. The same study suggests that for very high doping concentrations this transition can occur even in the absence of an external magnetic field. In monolayer CrI_3, doping significantly modifies the saturation magnetization, coercive force and Curie temperature, showing strengthened/weakened magnetic order with hole/electron doping[37]. Electrostatic doping is a key concept in the context of spin-dependent transistors based on magnetic monolayers.

As mentioned earlier, electric fields are also very important when considering magnetic skyrmions. After all, skyrmions can only appear in materials with a big enough uniform DMI. Electric fields can be used to introduce this uniform DMI in magnetic monolayers.

1.2.3 Spintronics

Spintronics — contraction of ’spin electronics’ — is the field that tries to exploit the spin of electrons, in addition to their charge, for utilization in (nanoscale) electronic devices. In what follows, we shortly review some promising spintronic device concepts based on magnetic monolayers. First, we take a look at a spin-dependent transistor developed recently[12]. This type of device show great promise towards achieving non-volatile data storage and more energy-efficient transistors[12]. Afterwards, we discuss an interesting paper that proposes the use of magnetic skyrmions as information carriers in memory devices.

Transistor Based on a Graphene/CrI_3 Heterostructure

Recent studies report a potentially interesting tunnel field-effect transistor (TFET), based on a graphene/CrI_3/graphene heterostructure[12]. The device features bilayer or four layers of CrI_3 sandwiched between two bilayer graphene samples creating a vertical tunnel junction, as shown in figure 1.9. Above and below the the graphene bilayers we find top and bottom gates made from few-layer graphite electrodes and hBN gate dielectrics. The gate potentials provoke an electric field that can control the current flow. Monolayer hBN serves as a good insulator due to its high bandgap of 6.07 eV[2]. A current flows through the device due to the quantum tunnelling of electrons from the source contact, through the CrI_3 layers, to the drain contact. The choice for bilayer graphene, rather than a monolayer, as the source- and drain contacts, is motivated by its bandgap. The gates can tune the Fermi level of the graphene contacts to modulate the tunnel conductance, the device can be put in the off-state by tuning the Fermi level into the bandgap. When using a gapless monolayer for the contacts, no off-state of the device can be observed. In this setup, the CrI_3 bilayer serves as a spin-filter, which allows us to obtain (highly) spin-polarized tunnelling

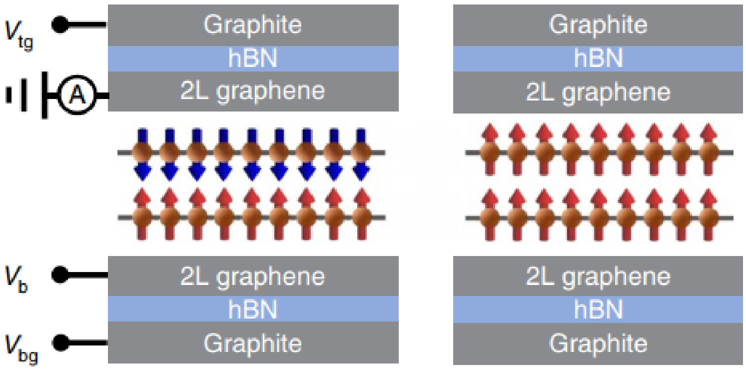

FIGURE 1.9: **TFET based on a graphene/CrI$_3$ heterostructure.** Operational principle of a spin-TFET based on a gate-controlled spin-flip transition in bilayer CrI$_3$ and spin filtering in the tunnel junction. Arrows indicate the spin orientation in the CrI$_3$ layers. The left and right panels correspond to a low and a high tunnel conductance state, respectively[12]. Figure from reference: [12].

currents. The spin-filter effect is based on the fact that there is an exponential dependence of the tunnel current on the tunnel barrier height[38]. Each monolayer of CrI$_3$ can now be thought of as a spin-filter for electrons with different tunnel barrier heights for spin- up and spin-down electrons[12]. When the bilayer is in its AFM ground state (figure 1.9, left), spin-up and spin-down electrons will experience approximately the same tunnel barrier height. Apart from tuning the Fermi level of the contacts, the gates can also induce a spin flip in the CrI$_3$ bilayer, as discussed in section 1.2.2. The electric field causes a huge reduction in the external magnetic field required for the spin-flip. When the bilayer is in the FM phase (figure 1.9, right), the barrier for one flavour of spins is reduced, the barrier for the other layer is increased. Due to the exponential dependence of the tunnelling probability on the barrier height, this will result in a greater overall electron transmission and a polarized spin current.

This device concept shows great promise for the future of TFET devices as it effectively provides us with spin-dependent outputs that are voltage-controllable and reversible[12]. However, in order to function properly, the device requires a non-zero bias magnetic field and low temperatures, the latter due to the Curie temperature of CrI$_3$, which is a serious obstacle for the device to become viable for usage in realistic conditions. The goal in future research will be to overcome these limitations by interchanging CrI$_3$ for other materials with higher critical temperatures and to achieve more efficient gating to eliminate the need for a bias magnetic field.

Skyrmions on the Track

Due to their relatively small size, the possibility to move them with small electric currents and their relative stability, magnetic skyrmions show a lot of promise to function as information carriers in spintronic memory and/or logic devices[29]. In the following, we discuss a memory device similar to domain wall based racetrack memory, but were the information is now encoded in a sequence of skyrmions instead of magnetic domains.

A racetrack memory device (figure 1.10) consists out of nanowires constructed from magnetic material. The nanowire is compartmentalized in many different equally big domains. Bits of information can be stored in the nanowire by assigning

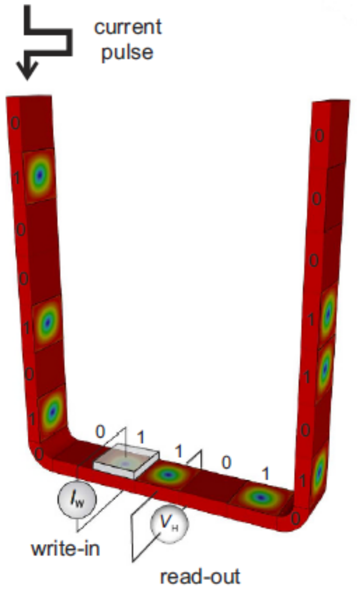

FIGURE 1.10: **Topological racetrack memory based on magnetic skyrmions.** The device consists out of nanowires that are divided in compartments. We assign a '1' or '0' to a compartment depending on the fact it contains a skyrmion or not. Information can be read or stored from/on the wire by a read-out and write-in device respectively. The compartments move through the wire via current pulses. Figure from reference: [33].

a '1' to a domain with a non-zero topological charge ($Q \neq 0$), i.e. a domain that contains a skyrmion, and a '0' to a domain with trivial topology ($Q = 0$)[33]. A sequence of magnetic domains, i.e. a sequence of zero's and one's, gives rise to byte's of information. We can write information in the nanowire by nucleation or destruction of skyrmions by electric fields. The information contained in a wire can be read by measuring the topological Hall effect. By applying current pulses, we can shift the whole magnetic domain pattern to move them over the read and write devices.

The interest in domain wall and skyrmion based racetrack memory devices is motivated by the prospect of achieving non-volatile data storage that could revolutionize the way we store data. IBM fellow Stuart Parking who invented the domain wall racetrack device, describes it as 'a solid state memory with the same low cost of a disk drive but with a performance 10 million times better'[39]. The skyrmion based racetrack takes this idea even further. Skyrmions can be much closer together than domain walls, and consequently there fit more skyrmions on a piece of material than domain walls which results in a bigger information density. Using skyrmions, thus, leads to faster information flows for similar current densities in comparison to domain wall version[29]. The goal of future research is now to improve our knowledge about skyrmion tuning, to achieve a better control of skyrmion motion and nucleation, and to obtain small diameter skyrmions at room-temperatures.

1.2.4 Magnonics

Magnonics is the field that concerns the study of spin waves in magnetic materials, and tries to exploit the properties of spin waves in applications. Possible applications include transmission, storage and processing of information. In this section, we briefly discuss some interesting concepts within the field of magnonics.

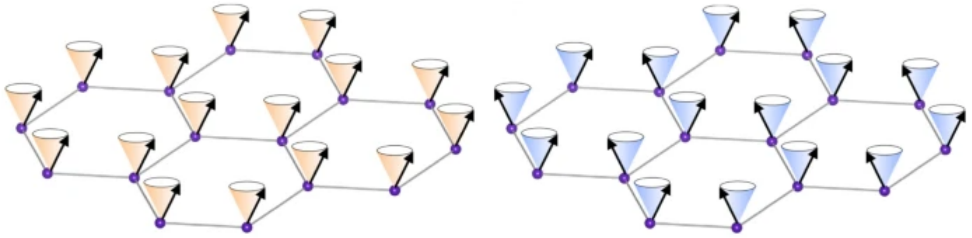

FIGURE 1.11: **Schematic figure of two spin wave modes observed in CrI_3 with Raman spectroscopy.** The cones represent the precession trajectories of the spins (black arrows). The precession of the spins on the two chromium sublattices are out-of-phase (right) and in-phase (left), which corresponds to the high- and low-energy modes respectively. Figure from reference: [40].

In spintronic devices, the frequency of spin waves determines the switching speed of the device. Current state-of-the-art devices based on Heisenberg ferromagnets have switching speeds in the GHz range[40]. Frequencies in the THz regime had not been achieved yet since these materials only have a weak magnetic anisotropy[40]. The discovery of 2D CrI_3 creates new opportunities to achieve high-frequency spin waves due to its interesting properties, namely, its strong magnetic anisotropy in the out-of-plane direction and its large exchange coupling between adjacent chromium atoms[40]. Recently, Raman spectroscopy confirmed the presence of at least two spin wave modes in CrI_3 at respectively 2.28 THz and 3.75 THz[40]. The same experiment also showed that the frequencies of these two spin modes remained constant for structures with a thickness between ten layers and a monolayer. The two spin wave modes correspond to respectively a high energy mode where adjacent spins precess out-of-phase and a low energy mode with an in-phase precession of the spins[40]. Both modes are depicted in figure 1.11. The spin waves in CrI_3 had a lifetime of the order of 10-100 ps[40]. These unique characteristics of spin waves in CrI_3 create opportunities for the development of extremely fast spintronic devices.

Another hot-topic in the field of magnonics are the so-called *magnonic crystals*. Magnonic crystals are artificially created materials with a specific periodic variation that can significantly influence the spectra of spin waves that propagate through it (cfr. how photonic crystals influence photon spectra). In correspondence with Bloch's theorem, such a periodic modulation of the material results in the formation of a spin wave band structure with a possible band gap. On a microscopic scale a magnonic crystal can be created by creating holes and groves in the material. Other ways to create a magnonic crystal include periodic electric gating, strain engineering or by growing the the 2D material on top of a substrate with a specific pattern that matches the requirements[41]. A magnonic crystal for THz frequencies is very hard to create with the aforementioned methods as it requires a modulation period of only a few nanometers[41]. In a recent paper, researchers here at the university of Antwerp showed that it is possible to create such a magnonic crystal by the introduction of Moiré patterns in the structure[41]. By depositing a non-magnetic molybdenum(IV)selenide ($MoSe_2$) layer on top of a magnetic $CrBr_3$ layer they were able to create a Moiré pattern, due to the lattice mismatch of the two materials, that serves as a magnonic crystal[41]. This study shows that it is possible to create magnonic crystals in the THz regime.

Due to their THz magnonic properties and the possibility to use them to create magnonic crystals, chromium trihalids have gained a lot of interest from the research community to study spin waves.

1.3 Outline of the Thesis

Both the discovery of new interesting functionalities and the promise of novel innovative applications motivate the increased interest in 2D magnetic materials. As the size of electronic devices keeps shrinking (cfr. Moore's law), more and more scientists and engineers turn the the field of 2D materials in search for new innovations. In order to be able to construct devices for a wide range of applications, we require many different materials with a wide range of properties. Off-course 2D magnetism can not be absent in the engineering toolbox. As the first ever discovered 2D magnet, CrI_3 has proven to be a unique platform to study the behaviour of magnetism in 2D. Especially the high tunability of the magnetic parameters, e.g. by lattice straining, electric gating, layer stacking or layer twisting among other techniques, is key for the manipulation of magnetic textures, e.g. domain-walls, spin-waves or magnetic skyrmions, which opens up an abundance of new possibilities for device concepts[41]. Also, the possibility to create magnonic applications in the THz regime has generated a lot of interest from the research community for CrI_3.

In this thesis, we focus on monolayer and bilayer CrI_3, and more precisely on the influence of stacking and twisting of the layers on the magnetic properties. First, we calculate several magnetic parameters that model the behaviour of the material, i.e. the symmetric- and anti-symmetric exchange parameters, and the single-ion anisotropy parameters. We will determine these parameters for the monolayer, the bilayer in three different stacking orders and for a twisted bilayer. We'll discuss how this stacking and twisting changes the magnetic parameters. Afterwards, we investigate for each system the dynamics of the magnetic spins which are described by the Landau-Lifshitz-Gilbert (LLG) equation. More precisely, we will take a look at some (meta)stable spin configurations of the systems, calculate the Curie temperature and study the behaviour of spin waves.

In chapter 2, we describe the methodology that was used to perform the calculations. The Heisenberg model is used to describe the interactions between the spins. We calculate the energy of different magnetic configurations of the system using density functional theory (DFT), and map these energies on the corresponding Heisenberg Hamiltonian. This method is called four-state energy mapping (4SM). Chapter 2 discusses both the theoretical background on which 4SM and DFT are based, and how they are implemented in practice. Once we have obtained the magnetic parameters, we can set up a model to investigate the spin dynamics via the LLG equation. In the last section of chapter 2, the theory behind these spin dynamics simulations will be explained.

In chapter 3 and 4, we apply this methodology to respectively the CrI_3 monolayer and bilayer. The crystal structures are optimized, the magnetic exchange parameters are calculated and the spin dynamics are simulated. For the bilayer, we consider three different stacking orders of the layers. Finally, we will also calculate the magnetic parameters for a twisted bilayer, and discuss the influence of the twist.

Finally, in chapter 5, we discuss the significance of the obtained results and give an outlook on further opportunities and challenges in the exciting field of 2D magnetic materials.

Chapter 2

Methodology

In this chapter, we describe a method that can be used to investigate the magnetic properties of materials. Interactions between magnetic moments can be modelled by the Heisenberg spin Hamiltonian. To obtain the magnetic exchange parameters that appear in the Heisenberg model, we use a very effective technique called *four-state energy mapping* (4SM). In the first section of this chapter, we will derive the formula for the magnetic exchange parameters, the DMI parameters, and the SIA parameters. Afterwards, we give an introduction to *density functional theory* (DFT) which is a very powerful computational method to study the electronic structure of materials. In the 4SM method, we will use DFT to calculate the energies of several magnetic configurations of a system, and then map these energies on their corresponding Heisenberg Hamiltonians. This energy mapping produces a system of equations that can be solved algebraically to obtain the magnetic exchange parameters. In the final section of this chapter, we discuss a method that can be used to study the dynamics and relaxation of spins in our material.

2.1 Four-State Energy Mapping

2.1.1 Heisenberg Hamiltonian

Magnetism in materials is caused by the interaction of atomic spins. The three interactions that will be included in our model for this thesis are: the symmetric exchange interaction, the anti-symmetric exchange interaction or DMI, and the SIA. In section 1.1.3 of the previous chapter, we discussed the origin of these interactions, and how they influence the behaviour of the spins in CrI_3. The different contributions are included in our model by adding their corresponding terms (see section 1.1.3) to the Hamiltonian. Now, the resulting interaction between the atomic spins can be described by the following Heisenberg Hamiltonian[42]:

$$\hat{\mathcal{H}} = \sum_{i<j} J_{ij} \hat{\mathbf{S}}_i \cdot \hat{\mathbf{S}}_j + \sum_i A_{ii} \hat{\mathbf{S}}_i^2, \tag{2.1}$$

in which the spins are 3D vectors $\mathbf{S}_i = (S_i^x, S_i^y, S_i^z)$ expressed in Cartesian coordinates. In the remainder of this work, we will drop the operator sign above the spins for the sake of notational simplicity. The strength of these interactions is determined by respectively the exchange matrix J_{ij} and the SIA matrix A_{ii}. To deduce which magnetic configurations will occur in CrI_3, we need to calculate all components of these matrices. In the next three sections, formula for these parameters will be derived. The 4SM procedure provides us with expressions for these parameters that depend solely on the magnitude of the spin S, and the energies of four different magnetic configurations that can be calculated with DFT.

2.1.2 Exchange Parameters

The exchange matrix J_{ij} is a 3×3 matrix and, thus, contains nine parameters. Each parameter characterizes the interaction between a Cartesian component of the i^{th} spin and a component of the j^{th} spin. For instance, the interaction between S_i^y and S_j^z is determined by J_{ij}^{yz}, or equivalently by $J_{ij}^{zy}(\equiv J_{ij}^{yz})$. The matrix elements can be written more generally as $J_{ij}^{\alpha\beta}$ with $\alpha, \beta = x, y, z$. Notice that, in general, $J_{ij}^{\alpha\beta} \neq J_{ij}^{\beta\alpha}$ for $\alpha \neq \beta$, but the symmetry of the crystal might impose this equality on the system[42].

To obtain the exchange parameters, we will, for the most part, follow the derivation as presented by Sabani et al. in reference [42] . We start the derivation by writing out the decomposition of Heisenberg Hamiltonian (2.1) in Cartesian components:

$$\hat{\mathcal{H}} = \sum_{i<j} \sum_{\alpha,\beta} S_i^\alpha \cdot J_{ij}^{\alpha\beta} \cdot S_j^\beta + \sum_i \sum_{\alpha,\beta} S_i^\alpha \cdot A_{ii}^{\alpha\beta} \cdot S_i^\beta. \tag{2.2}$$

Now, we select two arbitrary spin sites $i = 1$ and $j = 2$. Further, we select $\alpha = x$ and $\beta = z$ and will, thus, derive the formula for the exchange parameter J_{12}^{xz}. There is nothing special about the choice for this specific matrix element or these specific spin sites, the derivation of other exchange parameters will be completely analogous. Hence, it suffices to only present one derivation in this work. We continue the derivation by writing all the terms containing the two chosen spin sites separately:

$$\begin{aligned} \hat{\mathcal{H}} = & \sum_{\alpha,\beta} S_1^\alpha \cdot J_{12}^{\alpha\beta} \cdot S_2^\beta + \sum_{j\neq 2} \sum_{\alpha,\beta} S_1^\alpha \cdot J_{1j}^{\alpha\beta} \cdot S_j^\beta + \sum_{i\neq 1} \sum_{\alpha,\beta} S_i^\alpha \cdot J_{i2}^{\alpha\beta} \cdot S_2^\beta + \sum_{i\neq 1, j\neq 2} \sum_{\alpha,\beta} S_i^\alpha \cdot J_{ij}^{\alpha\beta} \cdot S_j^\beta \\ & + \sum_{\alpha,\beta} S_1^\alpha \cdot A_{11}^{\alpha\beta} \cdot S_1^\beta + \sum_{\alpha,\beta} S_2^\alpha \cdot A_{22}^{\alpha\beta} \cdot S_2^\beta + \sum_{i\neq 1,2} \sum_{\alpha,\beta} S_i^\alpha \cdot A_{ii}^{\alpha\beta} \cdot S_i^\beta. \end{aligned} \tag{2.3}$$

Let's introduce four different magnetic states of the system. Afterwards, we fill in these states in equation (2.3) to obtain the energy of each state. Now, it starts to become clear where this method got its name from. The four magnetic states are:

- State 1: $\mathbf{S}_1 = (S, 0, 0)$, $\mathbf{S}_2 = (0, 0, S)$;
- State 2: $\mathbf{S}_1 = (S, 0, 0)$, $\mathbf{S}_2 = (0, 0, -S)$;
- State 3: $\mathbf{S}_1 = (-S, 0, 0)$, $\mathbf{S}_2 = (0, 0, S)$;
- State 4: $\mathbf{S}_1 = (-S, 0, 0)$, $\mathbf{S}_2 = (0, 0, -S)$.

We know that, for CrI_3, the spin has a value of $S = 3/2$ (see section 1.1.2). However, we will not fill in this value yet in order to keep the derivation more general. Since we want to calculate parameter J_{12}^{xz}, spin $\mathbf{S}_1$ is oriented along the x-direction and spin $\mathbf{S}_2$ along the z-direction, both spins are oriented either parallel or anti-parallel to these axes depending on which of the four states we are considering. In all four magnetic states, all other spins are pointed along the y-axis, i.e. $\mathbf{S}_{i\neq 1,2} = (0, S, 0)$ or $(0, -S, 0)$, and are, thus, oriented perpendicular to $\mathbf{S}_1$ and $\mathbf{S}_2$. Notice that in these four states, spins $\mathbf{S}_1$, $\mathbf{S}_2$ and $\mathbf{S}_{i\neq 1,2}$ are all orthogonal with respect to each other. As will become clear in the next section, matrix element J_{12}^{xz}, and all other off-diagonal elements of the exchange matrix, are closely related to the DMI which tries to orient all spins perpendicular to each other. We want to point out that the diagonal elements of the exchange matrix, i.e. J_{12}^{xx}, J_{12}^{yy} or J_{12}^{zz}, are the exchange parameters associated with the symmetric exchange interaction. If we would like to calculate these diagonal elements, we choose both $\mathbf{S}_1$ and $\mathbf{S}_2$ alternately parallel or anti-parallel along respectively the x-, y- and z-direction, and all the other spins perpendicular to them. It are, thus, the diagonal elements that determine whether the spins favour a parallel or an anti-parallel orientation and, consequently, whether the ground state of the material is FM or AFM. In contrast, the off-diagonal elements give us more information about spin canting, but more on that in the next section. Back to the derivation! Remember that the expectation value of the Hamiltonian is equal to the total energy of the system. By filling in the four magnetic states in expression (2.3), we will, thus, obtain the energies of the four states. These energies are:

$$\begin{aligned} E_1 = S \cdot J_{12}^{xz} \cdot S + \sum_{j \neq 2} S_1 \cdot J_{1j}^{xy} \cdot S + \sum_{i \neq 1} S \cdot J_{i2}^{yz} \cdot S + \sum_{i \neq 1, j \neq 2} S \cdot J_{ij}^{yy} \cdot S \\ + S \cdot A_{11}^{xx} \cdot S + S \cdot A_{22}^{zz} \cdot S + \sum_{i \neq 1,2} S \cdot A_{ii}^{yy} \cdot S. \end{aligned} \tag{2.4}$$

$$\begin{aligned} E_2 = -S \cdot J_{12}^{xz} \cdot S + \sum_{j \neq 2} S_1 \cdot J_{1j}^{xy} \cdot S - \sum_{i \neq 1} S \cdot J_{i2}^{yz} \cdot S + \sum_{i \neq 1, j \neq 2} S \cdot J_{ij}^{yy} \cdot S \\ + S \cdot A_{11}^{xx} \cdot S + S \cdot A_{22}^{zz} \cdot S + \sum_{i \neq 1,2} S \cdot A_{ii}^{yy} \cdot S. \end{aligned} \tag{2.5}$$

$$\begin{aligned} E_3 = -S \cdot J_{12}^{xz} \cdot S - \sum_{j \neq 2} S_1 \cdot J_{1j}^{xy} \cdot S + \sum_{i \neq 1} S \cdot J_{i2}^{yz} \cdot S + \sum_{i \neq 1, j \neq 2} S \cdot J_{ij}^{yy} \cdot S \\ + S \cdot A_{11}^{xx} \cdot S + S \cdot A_{22}^{zz} \cdot S + \sum_{i \neq 1,2} S \cdot A_{ii}^{yy} \cdot S. \end{aligned} \tag{2.6}$$

$$\begin{aligned} E_4 = S \cdot J_{12}^{xz} \cdot S - \sum_{j \neq 2} S_1 \cdot J_{1j}^{xy} \cdot S - \sum_{i \neq 1} S \cdot J_{i2}^{yz} \cdot S + \sum_{i \neq 1, j \neq 2} S \cdot J_{ij}^{yy} \cdot S \\ + S \cdot A_{11}^{xx} \cdot S + S \cdot A_{22}^{zz} \cdot S + \sum_{i \neq 1,2} S \cdot A_{ii}^{yy} \cdot S. \end{aligned} \tag{2.7}$$

Apart from some changes in sign of the exchange terms here and there, these expressions are actually quite similar. The SIA terms are identical in all four states. We now got a system of four equations that we will solve for J_{12}^{xz}. By adding E_1 and E_4 and then subtracting E_2 and E_3, a lot of the terms will cancel out. We are left with:

$$E_1 + E_4 - E_2 - E_3 = 4S^2 \cdot J_{12}^{xz}. \tag{2.8}$$

From this, we can quite easily isolate the exchange parameter:

$$J_{12}^{xz} = \frac{E_1 + E_4 - E_2 - E_3}{4S^2}. \tag{2.9}$$

Here, we derived the expression for the case where $i = 1$, $j = 2$, $\alpha = x$ and $\beta = z$. The derivation for other matrix elements will be completely analogous (except for the choice of the four states). We can extend expression (2.9) to the general case that is valid for each element:

$$\boxed{J_{ij}^{\alpha\beta} = \frac{E_1 + E_4 - E_2 - E_3}{4S^2}.} \tag{2.10}$$

Note that this equation is applicable to any magnetic crystal, independent of the crystal symmetry or other structural constraints[42].

2.1.3 Dzyaloshinskii–Moriya Interaction Parameters

In the previous section, we already dropped a hint that the DMI parameters are very closely related to the off-diagonal elements of the exchange matrix. The anti-symmetric exchange interaction, or DMI, is characterized by the DMI vector (see section 1.1.3 for more information). The three components of this vector for the interaction between a spin $\mathbf{S}_i$ and a spin $\mathbf{S}_j$ are calculated as follows[42]:

$$\begin{aligned} D_{ij}^{x} &= \frac{1}{2}(J_{ij}^{yz} - J_{ij}^{zy}), \\ D_{ij}^{y} &= \frac{1}{2}(J_{ij}^{zx} - J_{ij}^{xz}), \\ D_{ij}^{z} &= \frac{1}{2}(J_{ij}^{xy} - J_{ij}^{yx}), \end{aligned} \tag{2.11}$$

in Cartesian coordinates. The exchange parameter J_{12}^{xz} that we calculated in the previous section, is thus, used in the calculation of the y-component of the DMI-vector. Notice that in systems with a symmetric exchange matrix, i.e. $J_{ij}^{\alpha\beta} = J_{ij}^{\beta\alpha}$, the DMI will be zero. In materials where this symmetry is broken, a non-zero DMI vector might appear. In the special case where the matrix is anti-symmetric, i.e. $J_{ij}^{\alpha\beta} = -J_{ij}^{\beta\alpha}$, the DMI-components can be simplified to:

$$\begin{aligned} D_{ij}^{x} &= J_{ij}^{yz} = -J_{ij}^{zy}, \\ D_{ij}^{y} &= J_{ij}^{zx} = -J_{ij}^{xz}, \\ D_{ij}^{z} &= J_{ij}^{xy} = -J_{ij}^{yx}. \end{aligned} \tag{2.12}$$

As explained in section 1.1.3, the DMI will try to force the spins in a orthogonal configuration. In practice, there will be competition between the DMI and the symmetric exchange interaction, which tries to implement a parallel or anti-parallel configuration, and the SIA, which tries to order all the spins along one specific energetically favourable direction. If DMI is present in a system, usually, its only effect will be a slight canting of the spins with respect to the anisotropic axis.

2.1.4 Single-Ion Anisotropy Parameters

Finally, we will also derive a formula for the SIA parameters of a magnetic system. Again, we will follow the derivation as presented by Sabani et al. in reference [42]. Unlike the exchange matrix, the SIA matrix has to be symmetric[42]. This is because the SIA parameters model the interaction between the spin components of one and the same single-ion[42]. Naturally, the interaction between spin components S_i^{α} and S_i^{β} is off course identical to the interaction between spin components S_i^{β} and S_i^{α}, with $\alpha, \beta = x, y, z$. Due to this symmetry, one only needs to calculate six matrix elements to construct the full SIA matrix, namely, the three diagonal elements and the three upper (or lower) off-diagonal elements. As will turn out, we need two different formula to calculate all the matrix elements, one for the diagonal elements, and one for the off-diagonal elements. The derivations themselves are pretty similar to the derivation of the exchange matrix that we presented earlier, a single exception being that we now select only one spin site instead of a spin pair[42].

We will present the derivation for an arbitrary spin site $i = 1$, the final formula can again be extended to the general case pretty easily. Let's start out by writing the decomposition of Heisenberg Hamiltonian (2.1) in Cartesian components, the terms containing components of spin $\mathbf{S}_1$ are written separately:

$$\begin{aligned}\hat{\mathcal{H}} =& \sum_{1<j}\sum_{\alpha,\beta} S_1^\alpha \cdot J_{1j}^{\alpha\beta} \cdot S_j^\beta + \sum_{1<i<j}\sum_{\alpha,\beta} S_i^\alpha \cdot J_{ij}^{\alpha\beta} \cdot S_j^\beta \\ &+ \sum_{\alpha,\beta} S_1^\alpha \cdot A_{11}^{\alpha\beta} \cdot S_1^\beta + \sum_{i\neq 1}\sum_{\alpha,\beta} S_i^\alpha \cdot A_{ii}^{\alpha\beta} \cdot S_i^\beta. \end{aligned} \tag{2.13}$$

The *off-diagonal elements* describe the interaction between different (Cartesian) spin components of the same ion. We need to calculate three off-diagonal elements, namely, $A_{11}^{xy} = A_{11}^{yx}$, $A_{11}^{xz} = A_{11}^{zx}$ and $A_{11}^{yz} = A_{11}^{zy}$. The equalities are off course valid because the SIA matrix is symmetric. Our final formula will be valid for all three elements but, as an example, we perform the derivation for the A_{11}^{xy} parameter. Again, we continue by defining four different magnetic states of our system. In this specific case, we choose our spin $\mathbf{S}_1$ in such a way that it lies along the diagonals of the xy-plane. The spin $\mathbf{S}_1$ will, thus, make a 45° angle with both the x- and y-axis. The four states are:

- State 1: $\mathbf{S}_1 = \left(\frac{\sqrt{2}}{2}S, \frac{\sqrt{2}}{2}S, 0\right)$;
- State 2: $\mathbf{S}_1 = \left(\frac{\sqrt{2}}{2}S, -\frac{\sqrt{2}}{2}S, 0\right)$;
- State 3: $\mathbf{S}_1 = \left(-\frac{\sqrt{2}}{2}S, \frac{\sqrt{2}}{2}S, 0\right)$;
- State 4: $\mathbf{S}_1 = \left(-\frac{\sqrt{2}}{2}S, -\frac{\sqrt{2}}{2}S, 0\right)$.

All other spins in the system will be oriented along the z-axis, i.e. $\mathbf{S}_{i\neq 1}$ = (0,0,S) or (0,0,-S). For the A_{11}^{xz} and A_{11}^{yz} parameters, the choice of the four states is pretty analogous. The spin $\mathbf{S}_1$ is chosen along the xz- or yz-plane respectively and all other spins are pointed along the axis perpendicular to this plane. By filling in these four states in equation (2.13), we can obtain the energies of each of the four states. These energies are:

$$\begin{aligned}E_1 =& \sum_{1<j}\frac{\sqrt{2}}{2}S \cdot J_{1j}^{xz} \cdot S + \sum_{1<j}\frac{\sqrt{2}}{2}S \cdot J_{1j}^{yz} \cdot S + \sum_{1<i<j} S \cdot J_{ij}^{zz} \cdot S \\ &+ \frac{S^2}{2} \cdot A_{11}^{xx} + \frac{S^2}{2} \cdot A_{11}^{xy} + \frac{S^2}{2} \cdot A_{11}^{yx} + \frac{S^2}{2} \cdot A_{11}^{yy} + \sum_{i\neq 1} S \cdot A_{ii}^{zz} \cdot S. \end{aligned} \tag{2.14}$$

$$\begin{aligned}E_2 =& \sum_{1<j}\frac{\sqrt{2}}{2}S \cdot J_{1j}^{xz} \cdot S - \sum_{1<j}\frac{\sqrt{2}}{2}S \cdot J_{1j}^{yz} \cdot S + \sum_{1<i<j} S \cdot J_{ij}^{zz} \cdot S \\ &+ \frac{S^2}{2} \cdot A_{11}^{xx} - \frac{S^2}{2} \cdot A_{11}^{xy} - \frac{S^2}{2} \cdot A_{11}^{yx} + \frac{S^2}{2} \cdot A_{11}^{yy} + \sum_{i\neq 1} S \cdot A_{ii}^{zz} \cdot S. \end{aligned} \tag{2.15}$$

$$\begin{aligned}E_3 =& -\sum_{1<j}\frac{\sqrt{2}}{2}S \cdot J_{1j}^{xz} \cdot S + \sum_{1<j}\frac{\sqrt{2}}{2}S \cdot J_{1j}^{yz} \cdot S + \sum_{1<i<j} S \cdot J_{ij}^{zz} \cdot S \\ &+ \frac{S^2}{2} \cdot A_{11}^{xx} - \frac{S^2}{2} \cdot A_{11}^{xy} - \frac{S^2}{2} \cdot A_{11}^{yx} + \frac{S^2}{2} \cdot A_{11}^{yy} + \sum_{i\neq 1} S \cdot A_{ii}^{zz} \cdot S. \end{aligned} \tag{2.16}$$

$$\begin{aligned}E_4 = &-\sum_{1<j}\frac{\sqrt{2}}{2}S\cdot J^{xz}_{1j}\cdot S-\sum_{1<j}\frac{\sqrt{2}}{2}S\cdot J^{yz}_{1j}\cdot S+\sum_{1<i<j}S\cdot J^{zz}_{ij}\cdot S\\ &+\frac{S^2}{2}\cdot A^{xx}_{11}+\frac{S^2}{2}\cdot A^{xy}_{11}+\frac{S^2}{2}\cdot A^{yx}_{11}+\frac{S^2}{2}\cdot A^{yy}_{11}+\sum_{i\neq 1}S\cdot A^{zz}_{ii}\cdot S.\end{aligned}\tag{2.17}$$

Again, we find pretty similar expressions for the four energies, the only difference are some sign changes. We solve this system of equations by adding E_1 and E_4 and then subtracting E_2 and E_3 from that result, a lot of the terms will cancel out. We end up with:

$$E_1+E_4-E_2-E_3=2S^2\cdot A^{xy}_{11}+2S^2\cdot A^{yx}_{11}=4S^2\cdot A^{xy}_{11},\tag{2.18}$$

where A^{xy}_{11} = A^{yx}_{11} due to the symmetry of the SIA matrix. If we isolate the SIA parameter, we get the final formula:

$$A^{xy}_{11}=\frac{E_1+E_4-E_2-E_3}{4S^2}.\tag{2.19}$$

This expression can be extended to the general formula that is valid for all off-diagonal ($\alpha\neq\beta$) SIA parameters:

$$\boxed{A^{\alpha\beta}_{ii}=\frac{E_1+E_4-E_2-E_3}{4S^2}.}\tag{2.20}$$

Again, note that this equation is applicable to any magnetic crystal, independent of the crystal symmetry or other structural constraints[42]. It's very hard not to see the similarities between both the derivation and the final result of the exchange parameters on one hand and the off-diagonal SIA parameters the other hand. However, for the diagonal elements of the SIA matrix, the final formula will look a little different.

For the *diagonal elements*, it suffices to calculate only two reduced terms instead of calculating all three the diagonal elements. The total spin is related to its components by the relation $S_i^2=(S_i^x)^2+(S_i^y)^2+(S_i^z)^2$. By using this relationship, each spin component can be represented by the total spin (which is known for a given material) and the two other components. Let's illustrate this more concretely. The diagonal part of the SIA Hamiltonian can be written as[42]:

$$\begin{aligned}\hat{\mathcal{H}}^{diag}_{SIA}&=\sum_i\sum_\alpha S_i^\alpha\cdot A^{\alpha\alpha}_{ii}\cdot S_i^\alpha\\ &=\sum_i S_i^x\cdot A^{xx}_{ii}\cdot S_i^x+\sum_i S_i^y\cdot A^{yy}_{ii}\cdot S_i^y+\sum_i S_i^z\cdot A^{zz}_{ii}\cdot S_i^z\\ &=\sum_i A^{xx}_{ii}\cdot S_i^2+\sum_i(A^{yy}_{ii}-A^{xx}_{ii})\cdot(S_i^y)^2+\sum_i(A^{zz}_{ii}-A^{xx}_{ii})\cdot(S_i^z)^2,\end{aligned}\tag{2.21}$$

where we substituted relationship $(S_i^x)^2=S_i^2-(S_i^y)^2-(S_i^z)^2$ in the second step. In this equation, the first term is actually not important, the second and third term already contain all the necessary information about the three diagonal elements[42]. Now, we will derive the formula to calculate these two reduced terms. We will do this for term $A^{yy}_{11}-A^{xx}_{11}$ as an example, off course the general formula we obtain in the end is also valid for the $A^{zz}_{11}-A^{xx}_{11}$ term and for any other reduced term on other spins sites $A^{\alpha'\alpha'}_{ii}-A^{\alpha\alpha}_{ii}$. Without the loss of generality, we choose an arbitrary spin site with spin $\mathbf{S}_1$ for which we will do this derivation[42]. The reduced term $A^{yy}_{11}-A^{xx}_{11}$ contains the SIA parameters for the x- and y-direction. Consequently, we define the following four magnetic states for our derivation:

- State 1: $\mathbf{S}_1 = (0, S, 0)$;
- State 2: $\mathbf{S}_1 = (0, -S, 0)$;
- State 3: $\mathbf{S}_1 = (S, 0, 0)$;
- State 4: $\mathbf{S}_1 = (-S, 0, 0)$.

All other spins in the material will be pointed along the z-direction, i.e. $\mathbf{S}_{i \neq 1}$ = (0,0,S) or (0,0,-S). By filling in these four states in equation (2.13), we can obtain the energies of each of the four states. These energies are:

$$E_1 = \sum_{j>1} S \cdot J_{1j}^{yz} \cdot S + S \cdot A_{11}^{yy} \cdot S + \sum_{i \neq 1} S \cdot A_{ii}^{zz} \cdot S. \tag{2.22}$$

$$E_2 = -\sum_{j>1} S \cdot J_{1j}^{yz} \cdot S + S \cdot A_{11}^{yy} \cdot S + \sum_{i \neq 1} S \cdot A_{ii}^{zz} \cdot S. \tag{2.23}$$

$$E_3 = \sum_{j>1} S \cdot J_{1j}^{xz} \cdot S + S \cdot A_{11}^{xx} \cdot S + \sum_{i \neq 1} S \cdot A_{ii}^{zz} \cdot S. \tag{2.24}$$

$$E_4 = -\sum_{j>1} S \cdot J_{1j}^{xz} \cdot S + S \cdot A_{11}^{xx} \cdot S + \sum_{i \neq 1} S \cdot A_{ii}^{zz} \cdot S. \tag{2.25}$$

When comparing these energies, we see that only in the first and second term of each expression there are some minor sign- and index changes, the third term is completely identical in all four expressions. To solve this system of equations, we add E_1 and E_2 together, and then subtract E_3 and E_4 from that result. We are left with:

$$E_1 + E_2 - E_3 - E_4 = 2S^2 \cdot A_{11}^{yy} - 2S^2 \cdot A_{11}^{xx}, \tag{2.26}$$

which results in the following formula for the reduced term:

$$A_{11}^{yy} - A_{11}^{xx} = \frac{E_1 + E_2 - E_3 - E_4}{2S^2}. \tag{2.27}$$

There are, thus, two small differences between this derivation and the previous two derivations, namely, the choice of the four states and the energies that need to be added and subtracted in the final formula. If we extend the above result to the general formula for the diagonal elements ($\alpha = \beta$) of the SIA parameters, we get:

$$\boxed{A_{ii}^{\alpha\alpha} - A_{ii}^{xx} = \frac{E_1 + E_2 - E_3 - E_4}{2S^2},} \tag{2.28}$$

with $\alpha = y, z$. Again, note that this equation is applicable to any magnetic crystal, independent of the crystal symmetry or other structural constraints[42].

At the start of this section, we claimed that we only needed to calculate six matrix elements to obtain the full SIA matrix. By calculating the reduced terms for the diagonal elements instead of calculating the three diagonal terms separately, the number of required elements reduces further to five. In the following paragraph, we show that, if we take the crystal symmetry into account, we might reduce this even further. Specifically, we will focus on the rotational symmetry in 2D systems or quasi-2D systems. A rotation around the z-axis by an angle θ in the counterclockwise direction can be written as[42]:

$$A_{new} = R_z(\theta) \cdot A_{old} \cdot R_z^T(\theta), \tag{2.29}$$

with A_{new} the SIA matrix in the rotated coordinate system, A_{old} the SIA matrix in the pre-rotation coordinate system and $R_z(\theta)$ the corresponding rotation matrix given by[42]:

$$R_z(\theta) = \begin{bmatrix} \cos\theta & \sin\theta & 0 \\ -\sin\theta & \cos\theta & 0 \\ 0 & 0 & 1 \end{bmatrix}. \tag{2.30}$$

After the execution of this transformation, we get the following two systems of equations[42]:

$$\text{System 1 (S}_1\text{)}: \quad \begin{cases} \left(A_{ii}^{yy} - A_{ii}^{xx}\right) \cdot \sin^2\theta + 2A_{ii}^{xy} \cdot \sin\theta\cos\theta = 0 \\ \left(A_{ii}^{yy} - A_{ii}^{xx}\right) \cdot \sin\theta\cos\theta - 2A_{ii}^{xy} \cdot \sin^2\theta = 0 \end{cases} \tag{2.31}$$

and,

$$\text{System 2 (S}_2\text{)}: \quad \begin{cases} A_{ii}^{xz} \cdot (\cos\theta - 1) + A_{ii}^{yz} \cdot \sin\theta = 0 \\ -A_{ii}^{xz} \cdot \sin\theta - A_{ii}^{yz} \cdot (\cos\theta - 1) = 0 \end{cases} \tag{2.32}$$

Further, we also get the trivial equality $A_{ii}^{zz} = A_{ii}^{zz}$. A system of equations only has a non-trivial solution if the determinant of the system in its matrix representation is equal to zero. The determinants for the two systems of equations are respectively:

$$\begin{aligned} det(\text{S}_1) &= -2\sin^2\theta, \\ det(\text{S}_2) &= 2(1 - \cos\theta). \end{aligned} \tag{2.33}$$

From these expressions, it's clear that for a system with 3-, 4-, or 6-fold rotational symmetry around the out-of-plane axis, i.e. when θ is respectively equal to $2\pi/3$, $\pi/2$ and $\pi/3$, the determinants are different from zero, and consequently, the system only has trivial solutions[42]. The four matrix elements represented by these two systems of equations will, thus, be equal to zero. These four elements are: $A_{ii}^{yy} - A_{ii}^{xx}$, A_{ii}^{xy}, A_{ii}^{xz} and A_{ii}^{yz}. Only the reduced element $A_{ii}^{zz} - A_{ii}^{xx}$ will be non-zero[42]. Of the five matrix elements we needed to calculate the full SIA matrix, only one element remains. This reduction makes the computation of the SIA parameters five times less demanding[42]. Monolayer CrI_3 has a 3-fold rotational symmetry, in the 4SM calculations discussed in this thesis, we only need to calculate the $A_{ii}^{zz} - A_{ii}^{xx}$ term, all the other terms are zero[42].

2.2 Density Functional Theory

The 4SM methodology provides us with a relatively easy strategy to obtain the magnetic parameters of a system. All what's left to do, is to calculate the energies of four magnetic configurations of the system, plug these energies in our formula, and repeat this for all elements in the exchange- and SIA matrices. To obtain these energies, we opt for the use of DFT as it's arguably (one of) the most popular and (one of) the most successful computational method(s) to study the properties of many-body systems. Especially in the fields of solid state physics and material science, DFT is a widely established theory and a plethora of literature is available. In this section, we revise the core principles and themes of DFT and briefly discuss how it's implemented in practice to solve concrete material physics problems.

2.2.1 Many-Body Schrödinger Equation

Consider a magnetic solid like for instance CrI_3. Since magnetism is a purely quantum mechanical effect, we describe this system by the *Schrödinger equation*. The time-independent Schrödinger equation for a crystalline material is given by:

$$\hat{\mathcal{H}}\Psi(\mathbf{R},\mathbf{r}) = E\Psi(\mathbf{R},\mathbf{r}), \tag{2.34}$$

with energy E the eigenvalue of Hamiltonian operator $\hat{\mathcal{H}}$, and $\Psi(\mathbf{R},\mathbf{r})$ the many-body wave function of the system[43]. Let's consider a material that contains M nuclei and N electrons. For notational simplicity we have written

$$(\mathbf{R}_1, \Sigma_1, \mathbf{R}_2, \Sigma_2, \ldots, \mathbf{R}_M, \Sigma_M) \equiv \mathbf{R} \tag{2.35}$$

and

$$(\mathbf{r}_1, \sigma_1, \mathbf{r}_2, \sigma_2, \ldots, \mathbf{r}_N, \sigma_N) \equiv \mathbf{r}, \tag{2.36}$$

where the position- and spin coordinates are respectively given by $\mathbf{R}_i$, Σ_i for nuclei and $\mathbf{r}_j$, σ_j for electrons[43]. The Hamiltonian operator $\hat{\mathcal{H}}$ consists out of five terms: the kinetic energy operators of the nuclei and the electrons, and the potential energy operators for the nucleus-nucleus interactions, the electron-electron interactions and the nucleus-electron interactions[43]. We, thus, write the Hamiltonian operator as[43]:

$$\hat{\mathcal{H}} = \hat{\mathcal{H}}_{kin,n} + \hat{\mathcal{H}}_{kin,e} + \hat{\mathcal{H}}_{pot,n-n} + \hat{\mathcal{H}}_{pot,e-e} + \hat{\mathcal{H}}_{pot,n-e}. \tag{2.37}$$

If we explicitly write out every term in this Hamiltonian, we get the following expression in Gaussian units:

$$\hat{\mathcal{H}} = \sum_{i=1}^{M} \frac{P_i^2}{2M_i^n} + \sum_{j=1}^{N} \frac{p_j^2}{2m_j^e} + \frac{1}{2}\sum_{i\neq i'}^{M} \frac{Z_i Z_{i'} e^2}{|\mathbf{R}_i - \mathbf{R}_{i'}|} + \frac{1}{2}\sum_{j\neq j'}^{N} \frac{e^2}{|\mathbf{r}_j - \mathbf{r}_{j'}|} - \sum_{i=1}^{M}\sum_{j=1}^{N} \frac{Z_i e^2}{|\mathbf{R}_i - \mathbf{r}_j|}. \tag{2.38}$$

In the kinetic energy terms, we define the momentum and the mass respectively as $\mathbf{P}_i$, M_i^n for nuclei and $\mathbf{p}_j$, m_j^e for electrons. In the interaction terms, symbol Z_i stands for the atomic number of the i^{th} nucleus, symbol e represents an elementary charge. In the nucleus-nucleus interaction and the electron-electron interaction, we add a factor 1/2 to avoid double counting of terms, further, we write $i \neq i'$ and $j \neq j'$ in the sums to exclude the self-interaction. In this Hamiltonian, we have two terms that depend solely on the nuclei, two terms that depend solely on the electrons and one term that couples the nuclei and the electrons.

Implicitly, we have made several assumptions when constructing Hamiltonian (2.38) that justify the fact that we included only five terms. First and foremost, notice that we only included the electromagnetic force in our expression, the gravitational force and the strong- and weak nuclear forces are neglected. This can be justified with some simple back-of-the-envelope calculations to estimate the order of magnitude of these forces between particles at realistic distances. The characteristic length scale between the particles in a solid is of the order of 1 Å. Consider a proton and an electron at a distance of 1 Å. The electrostatic force between the particles as calculated by Coulomb's law is approximately equal to $|\mathbf{F}| \approx 2.3 \times 10^{-8}\ N$. In contrast, Newton's law of gravitation for the force between these particles gives a value of $|\mathbf{F}| \approx 1.0 \times 10^{-47}\ N$. Therefore, it is fair to say that the gravitational force will have no significant effect on our simulations. At a distance 1 Å, the strong nuclear force between two protons will be practically equal to zero. The weak nuclear force, which is typically even smaller than the strong nuclear force, can therefore also assumed to be zero[44]. The strong- and weak nuclear forces become significant only on the femtometer scale and smaller[44]. They only have a significant influence on particles within the same nucleus or particles that approach very close to the nucleus[44]. In our calculations, these nuclear forces can safely be neglected as they will not have a significant influence on the magnetic properties of our system. More information on these force estimations can be found in section D of the appendix. Further, we also represented the particles as point charges. In our calculations, this approximation will pose no problems as the typical distances between the particles in our system (≈ 1 Å) are multiple orders of magnitude larger than the typical sizes of the nuclei (≈ 1 fm)[44]. Also, we neglect relativistic corrections for the motion of nuclei and electrons, e.g. the 'zitterbewegung'[45] etc. A relativistic effect that will be taken into account is the SOC, which will later on be added ad hoc to the Hamiltonian. Finally, we also make the trivial assumption that no external fields are present. Even though we have made quite a few assumptions already, Hamiltonian (2.38) still gives a fairly good description of our many-body system. However, more approximations are needed if we want to find a solution to the Schrödinger equation.

For many-body systems, like crystalline solids, it is notoriously difficult to analytically solve the Schrödinger equation. As soon as the system contains more than three particles, it becomes practically impossible to find a solution analytically, and even for one- and two particle systems we can only find analytical solutions in very specific cases, e.g. the particle in a box, the hydrogen atom, etc. If we resort to numerical methods, we can handle some more systems, but we're still far from being able to find a solution for realistic systems. Let's illustrate the complexity of this problem. Consider a sample of material with a number of particles of the order of Avogadro's number, i.e. $N_A = 6.02214076 \times 10^{23}$ particles[46]. Even most state of the art computers don't have enough RAM (random access memory) to store all the positions of these particles, let alone store additional data like velocities, energies and other particle properties that are needed in the calculation[*]. Even if we would be able to store all this data, the calculation would still take a (too) big amount of computational steps. Consider a system with M nuclei and N electrons. Each particle has three spatial coordinates and one spin coordinate, which results

---

[*] Example: The Vaughan cluster of the University of Antwerp has 152 nodes of 256 GB each[47]. To store a number of the 'double' type, we need 64-bits = 8 bytes. A crude estimation tells us that the Vaughan cluster can store a total number of 'doubles' of the order of $\approx 10^{12}$. In other words: not even close.

in a total number of $4M + 4N$ variables for the entire system. Finding a solution to Schrödinger equation (2.34) boils down to finding the eigenvalues and eigenvectors of a $(4M + 4N) \times (4M + 4N)$ Hamiltonian matrix. Typically, the number of required operations to solve this problem increases faster than the number of variables squared, i.e. we need more than $(4M + 4N)^2$ steps to solve this equation[48]. One can see that, for a big amount of particles, the number of required steps increases rapidly. From this paragraph, it becomes clear that we need to introduce some additional approximations in order to reduce the problem to a form which is not only solvable in theory, but also solvable in practice.

We can lower the computational cost by introducing the *Born-Oppenheimer approximation*. The physical idea behind this approximation is that, since their mass is way smaller, the electrons will move much faster than the nuclei[43]. Consequently the electrons will adjust their positions immediately when there is a change in the positions of the nuclei[43]. This is a very powerful assumption because from the perspective of the electrons its as if the nuclei are completely stationary, i.e. the electrons are moving in a field of fixed nuclei[43]. We can implement this approximation by writing the wave function as:

$$\Psi(\mathbf{R}, \mathbf{r}) = \Psi_n(\mathbf{R}) \cdot \Psi_e(\mathbf{R}; \mathbf{r}), \tag{2.39}$$

where the nuclear part of the wave function depends only on the nuclear coordinates and the electronic part of the wave function depends on the electronic coordinates explicitly, and nuclear coordinates parametrically[43]. By inserting equations (2.37) and (2.39) in the Schrödinger equation (2.34), we get[43]:

$$\begin{aligned} E\Psi_n(\mathbf{R})\Psi_e(\mathbf{R}; \mathbf{r}) = \big[& (\hat{\mathcal{H}}_{kin,n} + \hat{\mathcal{H}}_{pot,n-n}) \\ & + (\hat{\mathcal{H}}_{kin,e} + \hat{\mathcal{H}}_{pot,e-e} + \hat{\mathcal{H}}_{pot,n-e}) \big] \Psi_n(\mathbf{R})\Psi_e(\mathbf{R}; \mathbf{r}). \end{aligned} \tag{2.40}$$

If we group all the terms containing the electronic positions together, we find the electronic Schrödinger equation[43]:

$$\begin{aligned} \left(\hat{\mathcal{H}}_{kin,e} + \hat{\mathcal{H}}_{pot,e-e} + \hat{\mathcal{H}}_{pot,n-e}\right) \Psi_e(\mathbf{R}; \mathbf{r}) &= \left[E - \frac{\left(\hat{\mathcal{H}}_{kin,n} + \hat{\mathcal{H}}_{pot,n-n}\right) \Psi_n(\mathbf{R})}{\Psi_n(\mathbf{R})} \right] \Psi_e(\mathbf{R}; \mathbf{r}) \\ &= E_e(\mathbf{R})\Psi_e(\mathbf{R}; \mathbf{r}). \end{aligned} \tag{2.41}$$

After implementation of the Born-Oppenheimer approximation, we thus, get the electronic Schrödinger equation which only depends on the nuclear coordinates parametrically[43]. For a given set of nuclear coordinates, we can now solve this electronic Schrödinger equation for the electronic energy $E_e(\mathbf{R})$ and then use this to calculate the total energy through[43]:

$$E = \frac{\left(\hat{\mathcal{H}}_{kin,n} + \hat{\mathcal{H}}_{pot,n-n}\right) \Psi_n(\mathbf{R})}{\Psi_n(\mathbf{R})} + E_e(\mathbf{R}) = E_{pot,n-n}(\mathbf{R}) + E_e(\mathbf{R}). \tag{2.42}$$

Here, the Hamiltonian operators stand for respectively the kinetic energy of the nuclei and electrostatic interactions between the nuclei. Notice that, in expression (2.42), the kinetic energy of the nuclei can be completely neglected due to the fact that, in the Born-Oppenheimer approximation, we consider the nuclei stationary from the perspective of the electrons[43]. Instead of solving a $4M + 4N$ dimensional eigenvalue problem, we can now choose some set of nuclear coordinates, solve the electronic Schrödinger equation (2.41) for the electronic energies and subsequently calculate the total energy through formula (2.42).

By introducing the Born-Oppenheimer approximation, we have effectively reduced the many-body problem to a $4N$ dimensional eigenvalue problem which we have to solve for certain sets of nuclear coordinates. This is a significant reduction of the computational complexity of the calculation. Now, we can come up with an iterative scheme to solve many-body problems (see figure 2.1). We start off the procedure by choosing some initial nuclear coordinates, this choice can be based on experimental values or earlier theoretical studies. Subsequently, we solve the electronic Schrödinger equation, this will be done with DFT, the next three sections of this chapter will be dedicated to DFT and finding a solution to this equation. Next, we use the electronic energies to calculate the total energy of our system (via formula 2.42), and the forces acting on the nuclei. Based on these forces, the nuclear positions will be updated and the electronic Schrödinger equation will be solved for these updated positions. In section 2.2.5, we go into more detail on how the forces are calculated and how the ionic positions are updated. This whole procedure will be repeated until the energy difference between two iterations or the magnitude of the forces acting on the nuclei are converged below some threshold value. The convergence criteria will be discussed further in section 2.2.4.

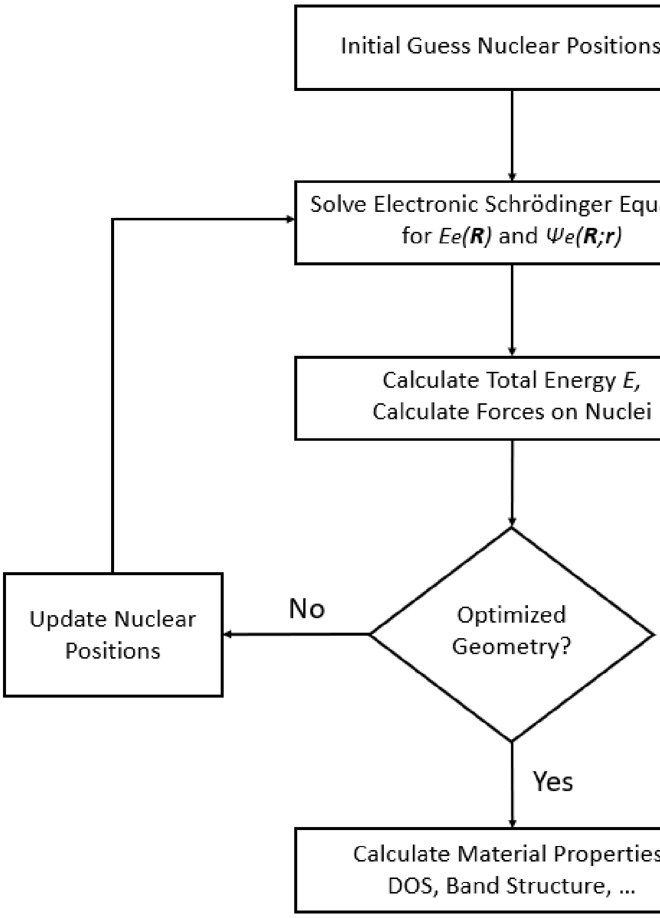

FIGURE 2.1: **Flowchart of an iterative scheme to solve many-body problems.** The procedure starts off with an initial choice of the nuclear positions. In each loop, the electronic Schrödinger equation is solved, the total energy and forces on the nuclei are calculated, and the nuclear positions are updated. The loop is repeated until some convergence criteria are met.

2.2.2 Hohenberg-Kohn Theorems

In the previous section, we showed that we can reduce the computational complexity of a many-body problem by fixing the nuclei. Now, we can solve the electronic Schrödinger equation in the field of these fixed nuclei, use this solution to update the nuclear coordinates, and repeat this loop until certain convergence criteria are met. In every step of this loop, we have to solve an eigenvalue problem with $4N$ variables. Although, this is a significant improvement in comparison with the $4M + 4N$ variables we had earlier, $4N$ variables is still too much to be able to solve the system for a realistic amount of electrons. However, we can reduce this number of variables by reformulating the problem in terms of the electron density instead of considering each individual electron. This is not merely an approximation, Hohenberg and Kohn formulated two theorems that show that it's possible to calculate any ground-state property of a system through knowledge of only the electron density[43].

Since the electronic wave function only depends on the nuclear coordinates parametrically, we can write it as $\Psi_e(\mathbf{R};\mathbf{r}) \equiv \Psi_e(\mathbf{r})$ for the sake of notational simplicity. The electron density is given by[43]:

$$\begin{aligned} \rho(\mathbf{r}) &= \langle \Psi_e(\mathbf{r}) | \hat{\rho}(\mathbf{r}) | \Psi_e(\mathbf{r}) \rangle \\ &= \sum_{i=1}^{N} \int \Psi_e^*(\mathbf{r}) \Psi_e(\mathbf{r}) \delta(\mathbf{r} - \mathbf{r}_i) d\mathbf{r}, \end{aligned} \tag{2.43}$$

with the electron density operator equal to:

$$\hat{\rho}(\mathbf{r}) = \sum_{i=1}^{N} \delta(\mathbf{r} - \mathbf{r}_i). \tag{2.44}$$

Notice, that we have defined $d\mathbf{r} \equiv d\mathbf{r}_1 d\mathbf{r}_2 \cdots d\mathbf{r}_N$, we've temporally omitted the spin polarization but it can also be included in the integration without significant qualitative changes to the results that will be presented in this section. Spatial integration of the electronic density gives the total number of electrons[43]:

$$N = \int \rho(\mathbf{r}) d\mathbf{r}. \tag{2.45}$$

In the many-body Schrödinger equation (2.37), we included a term $\hat{\mathcal{H}}_{pot,n-e}$ due to the interaction between the nuclei and the electrons. Since, from the point of view of the electrons, the nuclei are fixed, this interaction can be viewed as the electrons moving in an external crystal field. In the electronic Schrödinger equation, we write this term more generally as $\sum_i^N V_{\text{ext}}(\mathbf{r}_i)$. In our system, this external potential is indeed the crystal field, but other systems could also be exposed to external potentials with another origin. We choose for the more general notation since the Hohenberg-Kohn theorems are valid for any electronic system in any external potential. In the remainder of this chapter, let's assume this external potential is unknown[43]. Let's also assume that we do know the electron density, for instance, from experimental measurements[43]. The Hamiltonian for the electronic Schrödinger equation (2.39) can be written as:

$$\left(\hat{\mathcal{H}}_{kin,e} + \hat{\mathcal{H}}_{pot,e-e} + \sum_{i}^{N} V_{\text{ext}}(\mathbf{r}_i) \right) \Psi_e(\mathbf{R};\mathbf{r}) = E_e(\mathbf{R}) \Psi_e(\mathbf{R};\mathbf{r}). \tag{2.46}$$

In 1964, Hohenberg and Kohn proved the following two theorems[43]:

> **Theorem 1:** 'For a given ground-state density $\rho(\mathbf{r})$, we cannot have two different external potentials'. Consequently, 'the ground-state energy is a unique functional* of the electron density'.
>
> **Theorem 2:** 'The electron density $\rho(\mathbf{r})$ that minimizes the energy functional $E_e[\rho]$ is the (true) ground-state electron density'.

The first theorem states that the complete Hamiltonian is defined by a given electron density[43]. If we would know the electron density, we could, in principle, determine the full electronic wavefunction and, therefore, calculate any ground-state property of the system[43]. And so, not only the ground-state energy, but every ground-state property is a functional of the electron density[43]. The first theorem clearly is an existence theorem, i.e. it merely tells us that there exists a functional that relates any ground-state property with the electron density[43]. It doesn't tell us how such a functional would look like. Actually, this is a difficult problem to solve and for most properties, an approximation has to be used[43]. What the first theorem also doesn't tell us, is how to determine what the ground-state electron density of the system is. The answer is given by the second theorem, namely, the density that minimizes the total energy functional.

In what follows, we provide proof for these two theorems. Both proofs are based on the work of M. Springborg which can be found in reference [43]. To prove the first theorem, we start from the assumption that we have two different external potentials $V_{\text{ext},1}(\mathbf{r}_i) \neq V_{\text{ext},2}(\mathbf{r}_i)$ for a given density $\rho(\mathbf{r})$, and show that this leads to a contradiction. The two external potentials are assumed to differ more than an additive constant. We have two different Hamiltonian operators:

$$\hat{\mathcal{H}}_1 = \hat{\mathcal{H}}_{kin,e} + \hat{\mathcal{H}}_{pot,e-e} + \sum_i^N V_{\text{ext},1}(\mathbf{r}_i), \tag{2.47}$$

$$\hat{\mathcal{H}}_2 = \hat{\mathcal{H}}_{kin,e} + \hat{\mathcal{H}}_{pot,e-e} + \sum_i^N V_{\text{ext},2}(\mathbf{r}_i). \tag{2.48}$$

For each Hamiltonian we can write down its corresponding electronic Schrödinger equation:

$$\hat{\mathcal{H}}_1 \Psi_{e,1} = E_{e,1} \Psi_{e,1}, \tag{2.49}$$

$$\hat{\mathcal{H}}_2 \Psi_{e,2} = E_{e,2} \Psi_{e,2}. \tag{2.50}$$

Since the external potentials differ, the energies are also different $E_{e,1} \neq E_{e,2}$. Further, notice that we have two different wavefunctions $\Psi_{e,1} \neq \Psi_{e,2}$, but they give rise to the same electronic density $\rho(\mathbf{r})$ through formula (2.43). The variational principle tells us that:

$$E_i = \langle \Psi_i | \hat{\mathcal{H}}_i | \Psi_i \rangle \leq \langle \Psi_{j \neq i} | \hat{\mathcal{H}}_i | \Psi_{j \neq i} \rangle. \tag{2.51}$$

We consider the following two cases:

$$E_{e,1} = \langle \Psi_{e,1} | \hat{\mathcal{H}}_1 | \Psi_{e,1} \rangle < \langle \Psi_{e,2} | \hat{\mathcal{H}}_1 | \Psi_{e,2} \rangle, \tag{2.52}$$

$$E_{e,2} = \langle \Psi_{e,2} | \hat{\mathcal{H}}_2 | \Psi_{e,2} \rangle < \langle \Psi_{e,1} | \hat{\mathcal{H}}_2 | \Psi_{e,1} \rangle. \tag{2.53}$$

---

[*] One can think of a functional as a function that takes another function as its argument. For instance, in this case, the energy is a function of the density which is a function of the spatial coordinates.

The two cases can be worked out further to obtain:

$$\begin{aligned}
E_{e,1} < \langle \Psi_{e,2}|\hat{\mathcal{H}}_1|\Psi_{e,2}\rangle &= \langle \Psi_{e,2}|\hat{\mathcal{H}}_1 + \hat{\mathcal{H}}_2 - \hat{\mathcal{H}}_2|\Psi_{e,2}\rangle \\
&= \langle \Psi_{e,2}|\hat{\mathcal{H}}_1 - \hat{\mathcal{H}}_2|\Psi_{e,2}\rangle + \langle \Psi_{e,2}|\hat{\mathcal{H}}_2|\Psi_{e,2}\rangle \\
&= \langle \Psi_{e,2}|\sum_i^N V_{\text{ext},1}(\mathbf{r}_i) - \sum_i^N V_{\text{ext},2}(\mathbf{r}_i)|\Psi_{e,2}\rangle + E_{e,2} \\
&= \int \rho(\mathbf{r})[V_{\text{ext},1}(\mathbf{r}) - V_{\text{ext},2}(\mathbf{r})]d\mathbf{r} + E_{e,2}, \qquad (2.54) \\
E_{e,2} < \langle \Psi_{e,1}|\hat{\mathcal{H}}_2|\Psi_{e,1}\rangle &= \langle \Psi_{e,1}|\hat{\mathcal{H}}_2 + \hat{\mathcal{H}}_1 - \hat{\mathcal{H}}_1|\Psi_{e,1}\rangle \\
&= \langle \Psi_{e,1}|\hat{\mathcal{H}}_2 - \hat{\mathcal{H}}_1|\Psi_{e,1}\rangle + \langle \Psi_{e,1}|\hat{\mathcal{H}}_1|\Psi_{e,1}\rangle \\
&= \langle \Psi_{e,1}|\sum_i^N V_{\text{ext},2}(\mathbf{r}_i) - \sum_i^N V_{\text{ext},1}(\mathbf{r}_i)|\Psi_{e,1}\rangle + E_{e,1} \\
&= \int \rho(\mathbf{r})[V_{\text{ext},2}(\mathbf{r}) - V_{\text{ext},1}(\mathbf{r})]d\mathbf{r} + E_{e,1}. \qquad (2.55)
\end{aligned}$$

Here, we used the fact that the kinetic energy and the electron-electron interaction are identical in the two Hamiltonians (because for both cases we have the same electron density). Hence, the difference between the two Hamiltonians is equal to the difference between the external potentials. Let's transfer all the energies to the left part of the equations and multiply the first equation with -1. We are left with:

$$E_{e,2} - E_{e,1} > \int \rho(\mathbf{r})[V_{\text{ext},2}(\mathbf{r}) - V_{\text{ext},1}(\mathbf{r})]d\mathbf{r}, \qquad (2.56)$$

$$E_{e,2} - E_{e,1} < \int \rho(\mathbf{r})[V_{\text{ext},2}(\mathbf{r}) - V_{\text{ext},1}(\mathbf{r})]d\mathbf{r}. \qquad (2.57)$$

It's clear that both equations cannot be true at the same time. This contradiction proves that our initial assumption that the two external potentials are different has to be false, which confirms our first theorem. QED ■.

For the proof of the second theorem, we start off from the variational principle:

$$E_0 = \langle \Psi_0|\hat{\mathcal{H}}|\Psi_0\rangle \leq \langle \Psi'|\hat{\mathcal{H}}|\Psi'\rangle, \qquad (2.58)$$

with E_0 the ground-state energy and Ψ_0 the ground-state wavefunction associated with ground state density ρ_0. The variational principle states that the energy of a trial wavefucntion Ψ' is always greater than or equal to the ground-state energy, i.e. the energy is an upper bound for the ground-state energy. If we now take a density $\rho_1 \neq \rho_0$, than we know that the wavefunctions associated with these densities are also not equal $\Psi_1 \neq \Psi_0$. The variational principle then gives us:

$$E_0 = E_e[\rho_0] \leq E_e[\rho_1]. \qquad (2.59)$$

So only the ground-state density ρ_0 minimizes the total energy functional, i.e. gives us the ground-state energy. QED ■.

2.2.3 Kohn-Sham Method

The Hohenberg-Kohn theorems are an important step in the development of our methodology as they prove that using the electron density instead of individual particles is a valid approach. However, they do not provide a practical scheme to solve a many-body problem. In this section, we derive the approach that Kohn and Sham devised in 1965.

The second Hohenberg-Kohn theorem states that the (true) ground-state density minimizes the density[43]:

$$\delta E_e[\rho] = 0. \tag{2.60}$$

We combine this equation together with constraint (2.45) in one expression by using a Lagrange multiplier μ to[43]:

$$\begin{aligned} 0 &= \delta\left\{ E_e[\rho(\mathbf{r})] - \mu\left[\int \rho(\mathbf{r})d\mathbf{r} - N\right]\right\}, \\ &= \frac{\delta}{\delta\rho(\mathbf{r})}\left\{ E_e[\rho(\mathbf{r})] - \mu\left[\int \rho(\mathbf{r})d\mathbf{r} - N\right]\right\}. \end{aligned} \tag{2.61}$$

The electronic energy functional contains four terms[43]:

$$E_e[\rho(\mathbf{r})] = T[\rho(\mathbf{r})] + \int V_{\text{ext}}(\mathbf{r})\rho(\mathbf{r})d\mathbf{r} + \frac{1}{2}\int V_C(\mathbf{r})\rho(\mathbf{r})d\mathbf{r} + E_{xc}[\rho(\mathbf{r})]. \tag{2.62}$$

All four terms are functionals of the electronic density in position space. The first three terms are respectively the kinetic energy, the external potential and the interparticle Coulomb interaction. The fourth term is called the exchange-correlation (XC) term. The exchange interaction repels electrons with the same spin (cfr. exchange hole), the correlation is a measure for how the movement of one electron is influenced by the presence of all other electrons[49]. By filling in the energy functional in expression (2.61) and taking the functional derivative, we obtain[43]:

$$\frac{\delta T}{\delta\rho}(\mathbf{r}) + V_{\text{ext}}(\mathbf{r}) + V_C(\mathbf{r}) + \frac{\delta E_{xc}}{\delta\rho}(\mathbf{r}) = \mu. \tag{2.63}$$

More on the concept of functional derivatives can be found in section E of the appendix. This equation is still not easy to solve, mainly due to the interaction between the electrons. However, Kohn and Sham came up with a neat trick. They considered a fictitious model system of non-interacting particles that has the same density and energy as the real interacting system[43]. To ensure that the systems would have the same electronic density, they assumed that the particles were moving in some effective external potential $V_{\text{eff}}(\mathbf{r})$. For this model system, we thus, have the following energy functional[43]:

$$E_e[\rho(\mathbf{r})] = T'[\rho(\mathbf{r})] + \int V_{\text{eff}}(\mathbf{r})\rho(\mathbf{r})d\mathbf{r}. \tag{2.64}$$

Notice that the kinetic energies of the interacting system and the non-interacting system are not necessarily the same[43]. We have two different systems with different kinetic energies, the systems just happen to have the same density and energy. If we apply the Lagrange multiplier method like for the interacting system, we get[43]:

$$\frac{\delta T'}{\delta\rho}(\mathbf{r}) + V_{\text{eff}}(\mathbf{r}) = \mu. \tag{2.65}$$

By comparison with our earlier result, it becomes clear that the effective external potential is equal to[43]:

$$\begin{aligned} V_{\text{eff}}(\mathbf{r}) &= \frac{\delta T}{\delta \rho}(\mathbf{r}) - \frac{\delta T'}{\delta \rho}(\mathbf{r}) + \frac{\delta E_{xc}}{\delta \rho}(\mathbf{r}) + V_{\text{ext}}(\mathbf{r}) + V_C(\mathbf{r}), \\ &= V_{xc}(\mathbf{r}) + V_{\text{ext}}(\mathbf{r}) + V_C(\mathbf{r}), \end{aligned} \tag{2.66}$$

in which the first term is called the XC potential. The neat thing about this non-interacting model system, is that we can now write the Hamiltonian of electronic Schrödinger equation

$$\hat{\mathcal{H}}\Psi_e = E_e\Psi_e, \tag{2.67}$$

as a sum of effective single particle Hamiltonians[43]:

$$\hat{\mathcal{H}} = \sum_i^N \left[-\frac{1}{2}\nabla_i^2 + V_{\text{eff}}(\mathbf{r}_i) \right] = \sum_i^N \hat{h}_{\text{eff}}(\mathbf{r}_i). \tag{2.68}$$

Therefore, we can write the electronic wave function as a Slater determinant[43]:

$$\Psi_e = |\phi_1, \phi_2, \cdots, \phi_N|, \tag{2.69}$$

in which the single-particle orbitals can be determined from the *Kohn-Sham equations*:

$$\hat{h}_{\text{eff}}\phi_i = \varepsilon_i\phi_i. \tag{2.70}$$

These single-particle orbitals are related to the electronic density through expression:[43]

$$\rho(\mathbf{r}) = \sum_i^N |\phi_i(\mathbf{r})|^2, \tag{2.71}$$

in which the sum runs over the N orbitals with the lowest eigenvalues ε_i. Notice, that the density is determined by the single-particle orbitals that are calculated from the Kohn-Sham equations. However, to solve the Kohn-Sham equations we first need to know the effective potential which is off course dependent on the density. Therefore, we again need to come up with a iterative scheme to find a self-consistent solution. The procedure is shown in figure 2.2. This algorithm is also called a self-consistent field (SCF) calculation. We start off the algorithm with an initial guess for the electronic charge density. This initial density could be based on experimental measurements or densities from earlier theoretical calculations (cfr. DOS and band structure calculations discussed in section A.2 of the appendix). This initial density is used to set up the effective external potential. Afterwards, we have all the necessary information about our Hamiltonian to solve the Kohn-Sham equations (2.70) for eigenvalues ε_i and eigenvectors ϕ_i. Finally, with these single particle orbitals we can calculate the electronic density through formula (2.71). With this density, we can update the effective external potential which brings us back to the beginning of the loop. We repeat this algorithm until a certain convergence criterium is met, usually, until the electronic energy difference between two consecutive steps is converged below some predefined threshold value. Notice, that to solve our overall many-body problem, we perform two self-consistent loops. In the outer loop, we execute an ionic minimization (see figure 2.1). In each step of this ionic loop, we try to self consistently solve the electronic Schrödinger equation (see figure 2.2).

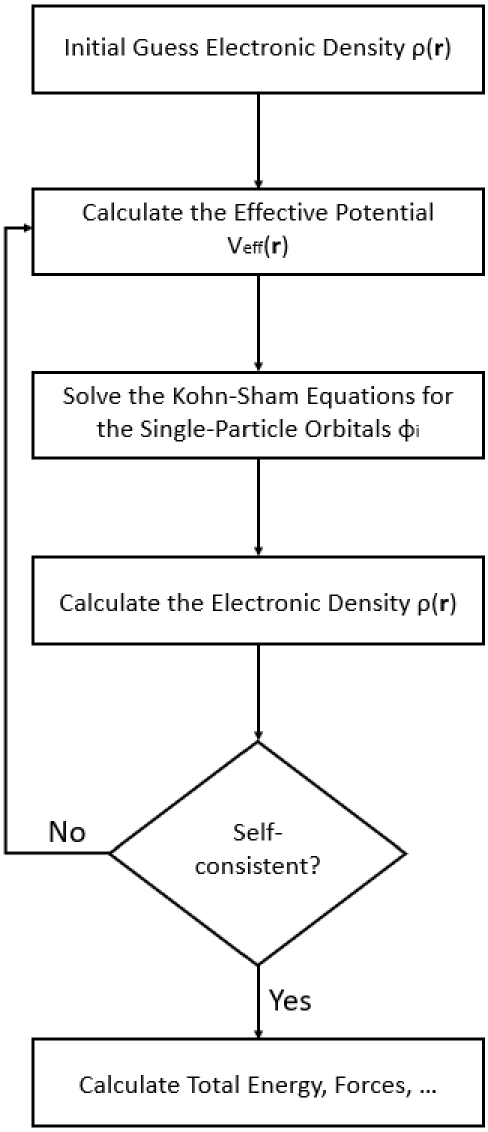

FIGURE 2.2: **Flowchart of an iterative scheme to solve the Electronic Schrödinger equation.** The procedure starts off with an initial choice for the electronic density. In each loop, the Kohn-Sham equations are solved and the density is updated. The loop is repeated until some convergence criteria are met.

We conclude this section, with some remarks about the Kohn-Sham method. First and foremost, for the Kohn-Sham method to be valid, we implicitly assumed that its always possible to construct a model system of non-interacting particles with the same ground-state density as the interacting system[43]. This is not necessarily the case, but since it should be possible in most realistic systems, and also in the materials under scrutiny in this thesis, this represents no problem[43]. Second, notice that the Lagrange multiplier μ that we used in this section, is the chemical potential[43]. The chemical potentials tells us how the energy of the system changes if you change the total number of electrons[43]. Up until now, we didn't consider spin polarisation in our discussion. However, the Hohenberg-Kohn and Kohn-Sham results could relatively easily be extended to include the spin polarisation. If we would do this, the electronic energy, and all other ground-state properties, would not only be a functional of the density $\rho(\mathbf{r})$ but also of the spin-polarisation $m(\mathbf{r})$, i.e. the energy functional is now[43]:

$$E_e = E_e[\rho(\mathbf{r}), m(\mathbf{r})]. \tag{2.72}$$

The Kohn-Sham method provides us with a very good algorithm to start solving electronic systems. However, there are a few problems that arise when implementing this theory in practice. The main problem that remains, is to find a suitable form for the effective potential. In the effective potential, usually, the XC-potential $V_{xc}(\mathbf{r})$ is unknown[43]. As this potential is unknown, we will have to make an approximation and choose one of the many functionals that have been developed over the years. In the next section, we will discuss our choice for the XC-functional. Further, we will also make some remarks considering the choice of basis-set and unit cell.

Notice that, technically speaking, DFT is an exact method. To some readers, this might sound surprising given the fact that we use quite a few approximations in our implementation of DFT. When presenting their theorems, Hohenberg and Kohn formulated DFT as an exact theory to solve many-body systems. If you have the (true) ground-state density, you can exactly determine the ground-state properties of a system. The problem is that, to determine this density, one needs to know the XC-functional, and the functionals that are used are always an approximation of the real functional.

2.2.4 Practical Implementation of DFT

In this section, we make some remarks concerning the implementation of the Kohn-Sham scheme in practice. We start off with a discussion on the XC-functional. Afterwards, we discuss the choice of the unit cell and the boundary conditions. Subsequently, we introduce some concepts related to reciprocal space, the Brillouin zone integration and the choice of a suitable basis-set. Finally, we also discuss the electronic minimization scheme.

Functional

The performance of Kohn-Sham DFT depends for a large part on the used XC-functional. The choice of functional depends on many different factors including the type of system you want to describe, the required accuracy and time limitations.

One of the simplest class of functionals that are commonly used are the so-called *local (spin-)density approximation* (L(S)DA) functionals. In L(S)DA, the XC-functional in each point $\mathbf{r}$ is equal to the potential that a homogeneous electron gas would have, if it had a density (and spin-polarisation) equal to the density (and spin-polarisation) in the point $\mathbf{r}$ of the system[43]. Notice that spatial variations of the density (and spin-polarisation) are completely ignored[43]. Functionals of the L(S)DA type, thus, only depend on local information, hence their name. L(S)DA functionals are used mainly to describe solids[43], since approximating the electrons in a solid by a free electron gas yields relatively good results (cfr. Drude-Sommerfeld model).

By including some non-local information, we could increase the accuracy of a calculation. A class of functionals that does this are the *generalized gradient approximation* (GGA) functionals. GGA functionals don't only include the density, but also the gradient of the density[43]. This slope will be large near nuclei and smaller far away from the nuclei. GGA functionals, thus, include non-local information about the system in the XC-functional.

The accuracy of calculations could be increased even further by including higher order terms that depend for instance on $\nabla^2\rho$, or by using hybrid functionals like the

B3LYP functional[50] which is a hybrid between the XC-functionals used in DFT and the exact exchange from the Hartree-Fock theory. One could also opt for a semi-empirical functional that contains parameters that are fitted to experimental data or earlier ab initio results. Over the years, more and more functionals got developed resulting in an enormous zoo of functionals that are available in literature. It would be rather pointless to give a summary of all the available functionals. Benchmarking for a fitting functional is a whole field on its own and would drive us too far for the purpose of this thesis. However, what is important to take away from this paragraph, is that one can increase the accuracy of a calculation by using a functional that includes more (non-local) information. On the other hand, more accurate (less local) functionals will often be more computationally expensive. The trade-off between accuracy and computational simplicity is the biggest factor that drives the functional picking process.

In our calculations, we opt for a functional of the GGA-type that was developed by Perdew, Burke and Ernzerhof (PBE)[51]. PBE is a widely used functional with lots of available literature, and has proven to give relatively accurate results for a lot of solid state systems without increasing the computational complexity too much.

Unit Cell & Boundary Conditions

All DFT calculations done in this thesis were performed using the Vienna Ab initio Simulation Package (VASP) software[52–54]. One of the properties of VASP is that it automatically implements periodic boundary conditions. Usually, this is pretty useful, especially when studying bulk solid materials since they have a periodic crystal structure. However, when studying materials that lack periodicity in one or more directions, the periodic boundary conditions pose some minor problems. For instance, when studying a 2D material, we only have periodicity in two directions. In the

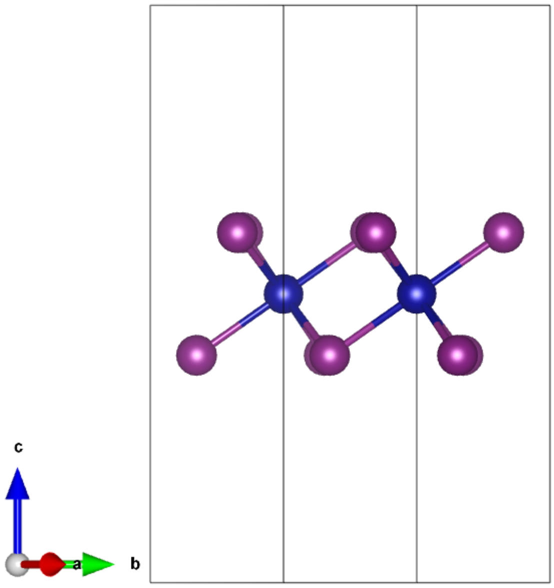

FIGURE 2.3: **Unit cell of a CrI_3 monolayer.** Chromium and iodine atoms are marked with blue- and purple spheres respectively. The unit cell is marked with black lines. A lot of vacuum is included in the out-of-plane direction of the unit cell to prevent interaction of the material with its duplicate(s) that are generated through the periodic boundary conditions.

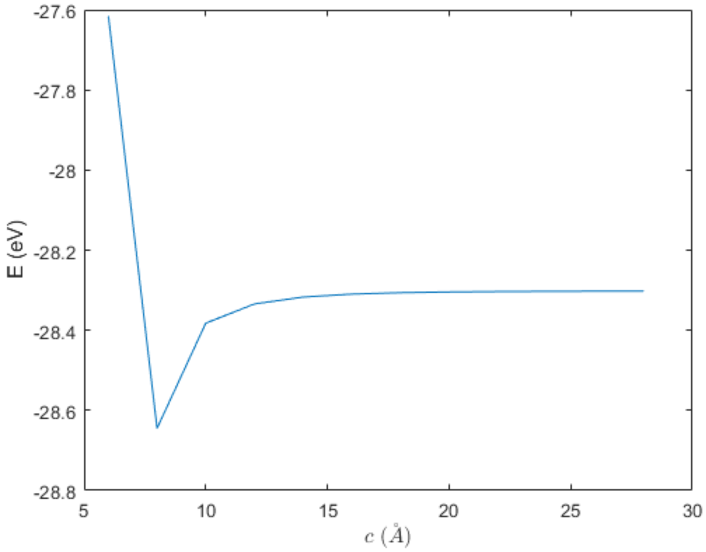

FIGURE 2.4: **Total energy of a CrI_3 monolayer as a function of the unit cell length in the out-of-plane direction.** For each unit cell length, we performed a single-point DFT calculation, i.e. no ionic updates only electronic updates. Thus, the atoms remain on the same position at all times. The simulation was performed on a CrI_3 monolayer with optimized geometry. This figure was plotted within the MATLAB computing environment.

third, out-of-plane, direction there is no periodicity. However, due to the periodic boundary conditions, the 2D layer will be repeated in this out-of-plane direction. This skews the results of the calculation as the 2D material is interacting with its duplicate(s)*. We can solve this problem by including some (big enough) amount of vacuum in our unit cell. This is illustrated in figure 2.3 for a CrI_3 monolayer, one can see that the unit cell (black lines) contains vacuum above and below the layer. For a multilayer structure, we also include vacuum above- and below the upper and lower layers but off-course not between the layers. If there is enough vacuum in the unit cell, there will still be an interaction between the 2D layer and its duplicate(s) but since the distance between them is so big, the influence of this interaction is negligible. On the other hand, one also doesn't want to include to much vacuum since this can result in a bigger computational cost. To determine the ideal amount of vacuum to include in our unit cell, we performed several simulations each one with a different unit cell length in the out-of-plane direction. In figure 2.4, we plotted the energy-distance graph that resulted from these calculations. For a small unit cell size, i.e. a small size between the layer and its duplicate(s), we notice an augmented energy which is due to repulsion between the layers. If we we increase the unit cell length a little further, we arrive in a minimum. The length associated with this minimum is the ideal bond length between layers in a bulk structure. When increasing the unit cell length even more, the energy will increase but there will still be attraction between the layers. For a unit cell length of 15 Å or higher, the energy will be more or less flat. From this point onward, the interaction between the layer and its duplicate(s) will be small enough so that it doesn't have a significant influence any more on the energy. In our calculations, we will always try to implement a vacuum distance of $c = 15$ Å .

---

*The periodic boundary conditions work on all sides of the unit cell, i.e. what leaves at the top comes back up at the bottom. So, in a sense, the material is interacting with itself.

Reciprocal Space & Brillouin Zone Integration

Instead of a real space representation of a crystal, we can also opt for a momentum space or k-space representation. This can be achieved by performing a Fourier transform on the direct lattice in order to obtain the reciprocal lattice. Just like we defined a Bravais lattice in 'real' space, we can define a reciprocal lattice in reciprocal space. The reciprocal lattice vectors can be calculated from the Bravais lattice vectors as follows[55]:

$$\mathbf{b}_1 = 2\pi\frac{\mathbf{a}_2 \times \mathbf{a}_3}{\mathbf{a}_1 \cdot \mathbf{a}_2 \times \mathbf{a}_3}; \quad \mathbf{b}_2 = 2\pi\frac{\mathbf{a}_3 \times \mathbf{a}_1}{\mathbf{a}_1 \cdot \mathbf{a}_2 \times \mathbf{a}_3}; \quad \mathbf{b}_3 = 2\pi\frac{\mathbf{a}_1 \times \mathbf{a}_2}{\mathbf{a}_1 \cdot \mathbf{a}_2 \times \mathbf{a}_3}. \tag{2.73}$$

Just like real space contains position vectors $\mathbf{r}$ that have a dimension of length, reciprocal space contains wavevectors $\mathbf{k}$ with a dimension of inverse length. The wavevector $\mathbf{k}$ is a function of the wavelength $|\mathbf{k}| = k = 2\pi/\lambda$. The Cartesian components of the wavevector, i.e. k_x, k_y and k_z, are often used as quantum numbers to label the states of a system. Just like the Bravais lattice, the reciprocal lattice consists out of a discrete set of points. The reciprocal lattice has an important property, namely, the larger the unit cell of a system in real space, the smaller the unit cell in reciprocal space, and vice versa. For instance, if you increase the real space unit cell by a factor three, the reciprocal unit cell will become three times smaller. If a crystal has no periodicity in a certain direction, one can think of the unit cell as being infinitely long in that direction. Consequently, the reciprocal lattice is infinitely small in that direction. For instance, a monolayer has no periodicity in the out-of-plane direction so the reciprocal lattice will also be 2D. Despite the fact that a bilayer consists of two stacked layers on top of each other, its reciprocal lattice will also be 2D since it is still non-periodic in the out-of-plane direction.

An important concept that needs to be introduced here is the *Brillouin zone*, which is defined as a Wigner-Seitz cell[*] in reciprocal space[55]. Just like a periodic repetition of the unit cell gives us the full lattice, a periodic repetition of the Brillouin zone gives us the whole reciprocal lattice. Notice that there are multiple Brillouin zones, conveniently called the first, second, third, etc. Brillouin zone. The first Brillouin zone is the Wigner-Seitz cell we described earlier. The second Brillouin zone is the region in reciprocal space that can be reached from the first Brillouin zone by crossing only one Bragg plane, i.e. a plane through the bisector of a reciprocal lattice vector[55]. Analogously, you can reach the third Brillouin zone by crossing two Bragg planes etc. Notice that all Brillouin zones have the same volume. In the remainder of this thesis, when we talk about the Brillouin zone, we always mean the first Brillouin zone. Another concept that needs to be introduced here is the *irreducible Brillouin zone*. Due to the symmetries of the point-group of the lattice, we can reduce the first Brillouin zone to a smaller region. The irreducible Brillouin zone is the part of the first Brillouin zone that can't be reduced any further. The entire Brillouin zone can be constructed from the irreducible Brillouin zone by symmetry operations. In the irreducible Brillouin zone there are several high-symmetry points, also called critical points, that get a special name. For a 2D hexagonal lattice, these points are the Γ-point, the K-point and the M-point[56].

In many cases, when doing electronic structure calculations, we need to integrate

---

[*] A Wigner-Seitz cell is a primitive cell that contains exactly one lattice point, and that is defined in such a way so that every point within the cell is closer to the lattice point of that cell than to any other lattice point (cfr. Voronoi construction). A Wigner-Seitz unit cell is the unit cell with the smallest possible volume.

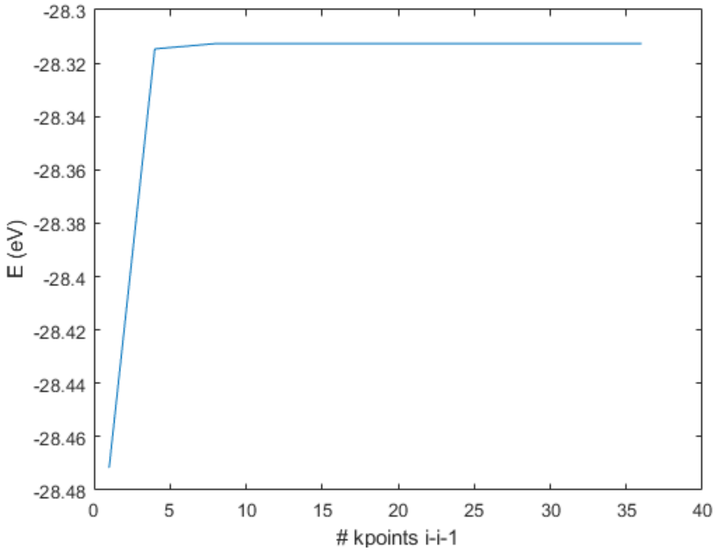

FIGURE 2.5: **Total energy of a CrI_3 monolayer as a function of the number of k-points.** For each number of k-points, we performed a single-point DFT calculation, i.e. no ionic updates only electronic updates. Thus, the atoms remain on the same position at all times. The simulation was performed on a CrI_3 monolayer with optimized geometry. This figure was plotted within the MATLAB computing environment.

over portions of the Brillouin zone or even the entire zone[57]. For instance, when calculating properties like the charge density or the DOS we need to integrate over the Brillouin zone. As an example, we write out the expression for the charge density:

$$\rho(\mathbf{r}) = \frac{1}{V_{\mathrm{BZ}}} \int_{\mathrm{BZ}} d\mathbf{k} \sum_i^N f_i^{(\mathbf{k})} |\phi_i^{(\mathbf{k})}|^2. \tag{2.74}$$

In practical calculations, we replace the integration of the entire Brillouin zone by quadrature over a finite number of points in the Brillouin zone. The integral is replaced by a weighted sum over special k-points:

$$\frac{1}{V_{\mathrm{BZ}}} \int_{\mathrm{BZ}} d\mathbf{k} = \sum_{\mathbf{k}} \omega_{\mathbf{k}_i}. \tag{2.75}$$

One of the most common k-point meshes to sample the Brillouin zone was first described by Monckhorst and Pack[57]. In the case of a $N_1 \times N_2 \times N_3$ Γ-point centred grid, we have:

$$\mathbf{k} = \sum_i^3 \mathbf{b}_i \frac{n_i + 1/2}{N_i}, \tag{2.76}$$

with $n_i = 0, N_i - 1$. In our calculations, we will use such a Γ-centred Monckhorst-Pack grid. However, we still need to determine how many k-points that will be used in our grid. You don't want to use too much k-points, the more k-points in the grid to heavier the calculation. However, you want to use enough k-points to make sure the energy is converged. Since the systems under scrutiny in this thesis don't have periodicity in the z-direction, we always use a 2D square k-point grid, i.e. $N \times N \times 1$ k-points. To determine N, we performed a series of single-point DFT calculations and plotted the energy as a function of the number of k-points. The result is shown in figure 2.5. For a $3 \times 3 \times 1$ k-point grid and bigger grids, the energy is well converged. In this thesis, for the lighter calculations, we usually use a $15 \times 15 \times 1$ grid in order to have the same input values as some papers that were consulted as a reference. For the heavier calculations, among which the 4SM calculations, we use a $3 \times 3 \times 1$ grid to reduce the computational cost as much as possible. For 4SM calcualtions on flakes, we used a $1 \times 1 \times 1$ grid since now there is no periodicity in the structure (see chapter 4). For DOS and band structure calculations, we increase the number of k-points to $24 \times 24 \times 1$ to get higher quality results.

Basis-Set

In Kohn-Sham DFT, we express the density as a function of single particle orbitals, see expression (2.71). A recurring theme in quantum mechanics is that we need to find a suitable basis for the Hilberspace of the wavefunction. In our situation, we need to find a suitable basis for the single-particle orbitals that determine the electronic density. For atoms or molecules, we often use linear combinations of atomic orbitals (LCAO) as the basis functions. Very often, these basis functions will be Gaussian functions. However, for periodic system like solids, we prefer to use plane wave basis sets.

In a solid, the electrons move in a periodic potential due to the nuclei. Bloch's theorem tells us that the eigenfunctions, i.e. the wavefunctions, of the Schrödinger equation in a periodic potential must be of the form[55]:

$$\psi_{\mathbf{k}} = u_{\mathbf{k}}(\mathbf{r}) \exp\{i\mathbf{k} \cdot \mathbf{r}\}. \tag{2.77}$$

In this expression, vector $\mathbf{r}$ is a position vector in real space and vector $\mathbf{k}$ the wavevector in reciprocal space. According to this theorem, a wavefunction can be written as a product of a plane wave $\exp\{i\mathbf{k} \cdot \mathbf{r}\}$ and a Bloch function $u_{\mathbf{k}}(\mathbf{r})$. The latter is a function that reflects the periodicity of the crystal lattice, i.e. that remains unchanged after a translation[55]:

$$u_{\mathbf{k}}(\mathbf{r}) = u_{\mathbf{k}}(\mathbf{r} + \mathbf{T}). \tag{2.78}$$

The translation vector is defined as $\mathbf{T} = n_1\mathbf{a}_1 + n_2\mathbf{a}_2 + n_3\mathbf{a}_3$, with n_1, n_2 and n_3 three arbitrary integers and $\mathbf{a}_1$, $\mathbf{a}_2$ and $\mathbf{a}_3$ the real space lattice vectors. Since there are multiple wavefunctions with the same $\mathbf{k}$, we can write the wavefunction with a band index n as $\psi_{n\mathbf{k}} = u_{n\mathbf{k}}(\mathbf{r}) \exp\{i\mathbf{k} \cdot \mathbf{r}\}$. Analogous to a translation in real space, we can write a translation in reciprocal space as $\mathbf{K} = n_1\mathbf{b}_1 + n_2\mathbf{b}_2 + n_3\mathbf{b}_3$, with n_1, n_2 and n_3 three arbitrary integers and $\mathbf{b}_1$, $\mathbf{b}_2$ and $\mathbf{b}_3$ the reciprocal lattice vectors[55]. As mentioned earlier, we can write arbitrary wavevector as $\mathbf{k}'$ as the sum of a wavevector inside the first Brillouin zone and a reciprocal translation vector, i.e. $\mathbf{k}' = \mathbf{k} + \mathbf{K}$. Without the loss of generality, we can assume that wavevector $\mathbf{k}$ lies in the first Brillouin zone. Now, we can expand (Fourier transform) the Bloch function in a planewave basis set:

$$u_{n\mathbf{k}}(\mathbf{r}) = \sum_{\mathbf{K}} c_{n\mathbf{k}}(\mathbf{K}) \exp\{i\mathbf{K} \cdot \mathbf{r}\}. \tag{2.79}$$

After plugging this expression in Bloch's theorem, we get:

$$\psi_{n\mathbf{k}} = \sum_{\mathbf{K}} c_{n\mathbf{k}}(\mathbf{K}) \exp\{i\mathbf{k} + \mathbf{K} \cdot \mathbf{r}\}. \tag{2.80}$$

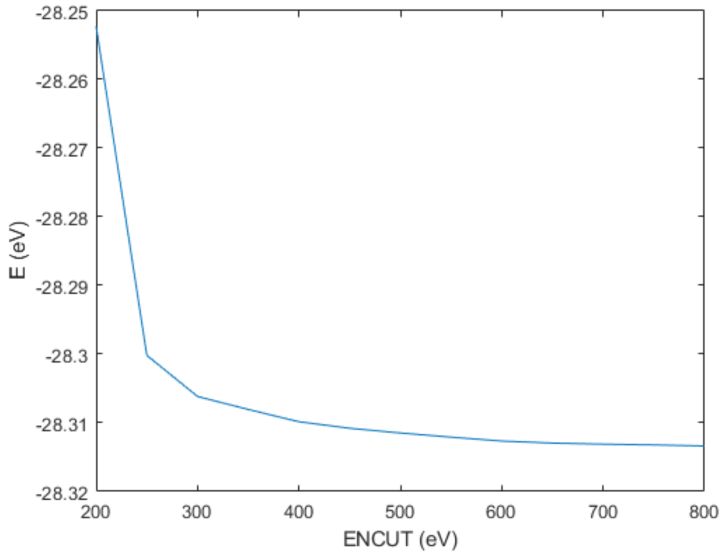

FIGURE 2.6: **Total energy of a CrI_3 monolayer as a function of the energy cut-off.** For each value of the energy cut-off, we performed a single-point DFT calculation, i.e. no ionic updates only electronic updates. Thus, the atoms remain on the same position at all times. The simulation was performed on a CrI_3 monolayer with optimized geometry. This figure was plotted within the MATLAB computing environment.

In principle, the plane wave expansion still contains an infinite number of plane waves. In practical calculations, we have to truncate the expansion in order to get a finite set of plane waves. We do this by defining a cut-off energy. We set an upper bound for the kinetic energy equal to:

$$E_{\text{cut}} > \frac{(\mathbf{k}+\mathbf{K})^2}{2}. \tag{2.81}$$

From this formula, you can determine at which wavevector you need cut-off the expansion. The choice of this energy cut-off value can have a significant influence on the results of a calculation. You need to include enough terms in order to get an accurate and well converged result. However, the more terms you include, the more computationally heavy your calculation will become. In VASP, the energy cut-off is implemented through the 'ENCUT'-tag. In order to determine the ideal value for ENCUT, we performed a series of calculations to investigate how the energy of our system is influenced by this energy cut-off. The result of these calculations is shown in figure 2.6. The energy of the system converges for an increasing energy cut-off. For calculations that aren't that computationally heavy, we often can afford to use a very high cut-off of 700 eV to get really accurate results. However, for most calculations a cut-off of 300 eV already gives pretty reasonable results. Therefore, in the heaviest calculations, i.e. 4SM calculations for the bilayers and the bilayers flakes, we will use an energy cut-off of 300 eV.

In the remainder of this section, we discuss some methods to reduce the number of required basis functions to accurately describe a wavefunction. The main reason why we need such huge basis sets is because the wavefunctions contain many nodes[43]. Even worse, the wavefunction contains the most nodes in the region close to the nucleus[43], and this is the region we're the least interested in. The part of the wavefunction were chemical reactions occur etc. lies outside the region were most nodes occur[43]. Basicly, there are two possible approaches to overcome this problem. In a first approach, we introduce a pseudopotential in order to replace the wavefunction with a smoother one[43]. This new wavefunction would agree with the old one in the chemical bond region, but would be smooth and without nodes close to the core[43]. This method succeeds very well in reducing the number of required basis functions and at the same time gives relatively accurate results.

However, in our calculations, a second approach will be used. This approach is called the *projector augmented wave* (PAW) method[58]. The PAW method uses the opposite strategy in comparison to the pseudopotential method, instead of simplifying the wavefunction, the basis will be adapted to match the potential[43]. In the PAW method, a wavefunction $\psi_{n\mathbf{k}}$ can be derived from the pseudo-wavefunction $\widetilde{\psi}_{n\mathbf{k}}$ through the following transformation[58]:

$$|\psi_{n\mathbf{k}}\rangle = |\widetilde{\psi}_{n\mathbf{k}}\rangle + \sum_i (|\phi_i\rangle - |\widetilde{\phi}_i\rangle)\langle \widetilde{p}_i \mid \widetilde{\psi}_{n\mathbf{k}}\rangle. \tag{2.82}$$

Just like in the pseudopotential method, wavefunction $\widetilde{\psi}_{n\mathbf{k}}$ coincides with the true wavefunction far away from the cores and is smooth close to the cores[58]. To define what is close or far from the nuclei, we can introduce a certain cut-off radius r_c, often this radius is chosen around half the nearest neighbour distance. The sphere defined by r_c is also called the augmentation region[58]. The quantities ϕ_i are partial waves and are solutions of the Kohn-Sham Schrödinger equation[58]. On the other hand, quantities $\widetilde{\phi}_i$ are pseudo partial waves, they are identical to ϕ_i outside r_c and are smooth inside r_c[58]. Inside the augmentation region, the pseudo-wavefunctions can be expanded in pseudo-partial waves $|\widetilde{\Psi}\rangle = \sum_i |\widetilde{\phi}_i\rangle c_i$ [58]. Finally, $\widetilde{p}_i$ is called the projector function and obeys the important relation $\langle \widetilde{p}_i|\widetilde{\phi}_j\rangle = \delta_{ij}$ [58]. Very simply put, formula (2.82) tells us that the true wavefunction is equal to the pseudo-wavefunction (that gives an accurate description outside the augemtation region), plus a the partial wave term (that gives an accurate discription of the wavefunction inside the augmentation region) and minus the pseudo-partial wave term (that describes the pseudo-wavefunction inside the augmentation region).

Electronic Minimization

To conclude the section about the practical implementation of DFT, we very briefly discuss some methods for diagonalization of the Kohn-Sham Hamiltonian. When self-consistently solving the Kohn-Sham equations, we use the blocked Davidson algorithm in the first iteration of the loop and afterwards switch to the residual minimization method by direct inversion of the iterative subspace (RMM-DIIS)[59][*]. The blocked Davidson iteration scheme is used only in the first step since it is a factor 1.5-2 slower than the RMM-DIIS algorithm. The main idea behind these iterative matrix diagonalization techniques, is that we don't need all the eigenvectors of the Hamiltonian but only the N_b lowest eigenstates (with N_b of the order of electrons per unit cell). The techniques are based on the Rayleigh-Ritz method to approximate the eigenvalues of a $N_b \times N_b$ subspace. The interested reader can find more information on these electronic minimization methods on the VASP website were multiple lectures are available[**].

---

[*] In VASP, set ALGO = Fast in the INCAR file.

[**] https://www.vasp.at/wiki/index.php/The_VASP_Manual

2.2.5 Ionic Relaxation

In this section, we will fill in the last remaining gaps of the flowchart presented in figure 2.1. We will discuss how the forces on the nuclei are calculated and how the nuclear positions are updated in order to obtain an optimized geometry.

To determine whether a certain set of nuclear coordinates is close to the optimized structure, we will calculate the forces acting on the nuclei. These calculations can be done via the *Hellmann-Feynman theorem*. The forces equal the negative of the gradient of the energy:

$$F_i = -\frac{\partial E}{\partial \mathbf{R}_i}, \tag{2.83}$$

with $i \in 1, \cdots, M$, i.e. the system contains M nuclei. When the energy is minimal, the forces acting on the nuclei will be zero. By using the expressions for the electronic Schrödinger equation (2.41) and the total energy (2.42), we can derive a formula for the forces on the nuclei:

$$\begin{aligned}
F_i &= -\frac{\partial}{\partial \mathbf{R}_i}\left[E_{pot,n-n}(\mathbf{R}) + E_e(\mathbf{R})\right] \\
&= -\frac{\partial}{\partial \mathbf{R}_i}\left[E_{pot,n-n}(\mathbf{R}) + \langle \Psi_e(\mathbf{R};\mathbf{r})|\hat{\mathcal{H}}_{kin,e} + \hat{\mathcal{H}}_{pot,e-e} + \hat{\mathcal{H}}_{pot,n-e}|\Psi_e(\mathbf{R};\mathbf{r})\rangle\right] \\
&= -\frac{\partial E_{pot,n-n}(\mathbf{R})}{\partial \mathbf{R}_i} - \frac{\partial}{\partial \mathbf{R}_i}\langle \Psi_e(\mathbf{R};\mathbf{r})|\hat{\mathcal{H}}_{pot,n-e}|\Psi_e(\mathbf{R};\mathbf{r})\rangle \\
&= -\frac{\partial E_{pot,n-n}}{\partial \mathbf{R}_i} - \langle \frac{\partial \Psi_e}{\partial \mathbf{R}_i}|\hat{\mathcal{H}}_{pot,n-e}|\Psi_e\rangle - \langle \Psi_e|\frac{\partial \hat{\mathcal{H}}_{pot,n-e}}{\partial \mathbf{R}_i}|\Psi_e\rangle - \langle \Psi_e|\hat{\mathcal{H}}_{pot,n-e}|\frac{\partial \Psi_e}{\partial \mathbf{R}_i}\rangle \\
&= -\frac{\partial E_{pot,n-n}}{\partial \mathbf{R}_i} - \langle \Psi_e|\frac{\partial \hat{\mathcal{H}}_{pot,n-e}}{\partial \mathbf{R}_i}|\Psi_e\rangle \\
&= -\frac{\partial E_{pot,n-n}(\mathbf{R})}{\partial \mathbf{R}_i} - \int d\mathbf{r}\, |\Psi_e|^2 \frac{\partial E_{pot,n-e}(\mathbf{R},\mathbf{r})}{\partial \mathbf{R}_i}.
\end{aligned} \tag{2.84}$$

In this derivation, all the derivatives of terms that don't explicitly depend on the nuclear coordinates are zero. The only terms that stay present are the forces due to the nuclei-nuclei interactions, and the forces due to the nuclei-electron interactions. The electronic wave function $\Psi_e(\mathbf{R};\mathbf{r})$ is found by solving the electronic Schrödinger equation.

For the ionic relaxation, we use the conjugate gradient algorithm[60]. This is a predictor-corrector step algorithm. In a first step (predictor step), the ionic positions are moved in the direction of the resulting forces acting on them. If the corresponding settings are enabled, the shape and volume of the unit cell will also be changed based on the stress in the cell (usually we will keep the cell shape and volume fixed). Afterwards, through an interpolation that takes into account the change in energy and forces after the trial step, the approximate minimum is calculated and a corrector step towards the approximate minimum is performed. If the convergence criteria for the forces of the total energy aren't reached yet, new predictor and corrector steps are made until the geometry of the system is sufficiently converged.

2.3 Spin Dynamics

In this section, we will describe how we can study the dynamics of the magnetic spins, i.e. how the spin configuration of our material changes over time. Up until now, we have always fixed the spins in a certain direction, and then calculated the energy of the system while the spins were fixed in order to determine the magnetic parameters that model the interaction strength between the spins. Now, we take the magnetic parameters as an input and simulate how the spins want to order themselves to minimize the energy of the system.

The dynamics of magnetic spins can be explored by the *Landau-Lifshitz-Gilbert* (LLG) equation[41]:

$$\frac{\partial \hat{\mathbf{S}}_i}{\partial t} = -\frac{\gamma}{(1+\alpha^2)\,\mu}\left[\hat{\mathbf{S}}_i \times \mathbf{B}_i^{\text{eff}} + \alpha\hat{\mathbf{S}}_i \times \left(\hat{\mathbf{S}}_i \times \mathbf{B}_i^{\text{eff}}\right)\right], \tag{2.85}$$

in which γ is gyromagnetic ratio and α the damping parameter. The effective field is found by taking the derivative of the Hamiltonian $\mathbf{B}_i^{\text{eff}} = -\partial\hat{\mathcal{H}}/\partial\hat{\mathbf{S}}_i$, thus, the field can be thought of as a gradient in the energy[61]. The magnetic parameters enter the LLG equation through Hamiltonian (2.1) which is used to determine the effective field. The effective field is, thus, the field that results due to all the different magnetic interactions that are included in the Heisenberg model. If we also want to investigate the thermal dependencies of the magnetization, the effective field will will also contain a stochastic thermal field (i.e. $\boldsymbol{B}_i \to \boldsymbol{B}_i + \boldsymbol{B}_i^{\text{th}}$) given by[61]:

$$\mathbf{B}_i^{\text{th}}(t) = \sqrt{2D_i}\boldsymbol{\eta}_i(t) = \sqrt{2\alpha k_{\text{B}} T\frac{\mu_i}{\gamma}}\boldsymbol{\eta}_i(t), \tag{2.86}$$

i.e. the fluctuation-dissipation theorem with $\boldsymbol{\eta}_i(t)$ white noise such that the ensemble average and variance of the thermal field fulfil $\langle \boldsymbol{B}_{i\alpha}^{\text{th}}(t)\rangle = 0$ and $\langle \boldsymbol{B}_{i\alpha}^{\text{th}}(t)\boldsymbol{B}_{j\beta}^{\text{th}}(0)\rangle = 2D_i\delta_{ij}\delta_{\alpha\beta}\delta(t)$ respectively. Further, we have D_i the diffusion constant, k_{B} the Boltzmann constant and T the temperature[61]. The first term in the LLG equation (2.85) represents the precession of the spins, the second term is a damping term[61]. The movement of the spins can be interpreted as follows: the spins will try to precess around the axis of the effective field due to the first term, meanwhile the damping term tries to relax the spins in the direction of the effective field. In some cases, more terms can be included in the LLG equation, e.g. a term that represents the spin-transfer torque, but this is not necessary in our calculations.

Off-course, when the direction of one spins changes, this has an influence on their neighbouring spins. We will, thus, have to perform the simulations over a big enough amount of time steps in order to obtain an equilibrium spin configuration. In a temperature dependent simulation, we start off from an elevated temperature and gradually decrease the temperature in a certain amount of steps. In each step, we solve the LLG equation to determine the spin configuration and calculate the magnetization. From the magnetization-temperature curve, we will be able to determine the Curie temperature. The spin configuration after the final step will be a (meta)stable spin configuration of the system. We can also use this framework to study spin-waves by introducing a local sinusoidal magnetic field that let's certain spins oscillate, and afterwards track how these oscillations propagate through the material over time. All simulations were performed with the *Spirit* simulation package[61], which is a C++ based framework to study spin dynamics. Computational details about the simulations can be found in section B of the appendix.

Chapter 3

Monolayer

3.1 Crystal Structure

A CrI_3 monolayer is a polyhedral-thick slab in which one layer of chromium atoms is sandwiched between two layers of iodine atoms. The chromium atoms form a hexagonal- or honeycomb lattice in which each chromium atom is octahedrally coordinated with six iodine atoms. Each iodine atom is bound to two chromium atoms. The Cr-I-Cr bonds have a bonding angle of $\approx 90°$. The typical crystal structure of a CrI_3 monolayer is shown in figure 3.1.

Since crystals have a periodic structure, we can describe them using periodic boundary conditions. The unit cell, i.e. the smallest part of the crystal that contains the full lattice symmetry, incorporates two chromium- and six iodine atoms and is marked with black lines on figure 3.1. The entire crystal structure can be obtained by a repetitive translation of the unit cell along the crystal axes. The lattice vectors along these axes are given by:

$$\mathbf{a} = \left(\frac{\sqrt{3}}{2}, -\frac{1}{2}, 0\right) a, \quad \mathbf{b} = \left(\frac{\sqrt{3}}{2}, \frac{1}{2}, 0\right) a, \quad \mathbf{c} = \left(0, 0, 1\right) c, \tag{3.1}$$

with a and c the lattice constants. When we relax the structure using ab initio calculations based on DFT, we find a lattice constant of a = 6.919 Å, a Cr-I bond length equal to 2.77 Å and a Cr-I-Cr bond angle of 92.46°. For computational details and implementation in VASP, we refer to section A.1 of the appendix. To determine the other lattice constant (c), it's important to realize that monolayers don't have periodicity in the out-of-plane direction. However, since we use periodic boundary

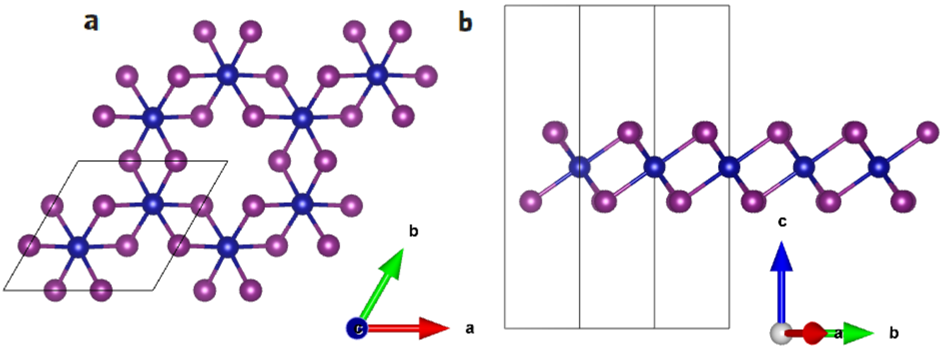

FIGURE 3.1: **Crystal structure of a CrI_3 monolayer.** Top view (a) and sideways view (b) of a CrI_3 monolayer's crystal structure. Chromium and iodine atoms are represented by blue and purple spheres respectively. The unit cell is marked with black lines.

conditions, the unit cell will replicate itself along all three crystal axes and, thus, also in this out-of-plane direction. This problem can be solved by choosing $c \geq 15$ Å in order to include a good amount of vacuum in the unit cell. Due to this vacuum, the (short-range) vdW interaction between adjacent layers will be negligibly small. We refer to the earlier section on the practical implementation of DFT calculations (section 2.2.4) for more details on the unit cell vacuum. The atomic positions within the unit cell can be written as a function of the lattice vectors, i.e. in direct coordinates:

$$\mathbf{R}_i = x_i\mathbf{a} + y_i\mathbf{b} + z_i\mathbf{c}. \tag{3.2}$$

The position of an arbitrary atom in the material $\mathbf{R}_i'$ can be written as the position of the corresponding atom within the unit cell and an additional translation:

$$\begin{aligned} \mathbf{R}_i' &= \mathbf{R}_i + \mathbf{T} \\ &= \mathbf{R}_i + n_1\mathbf{a} + n_2\mathbf{b} + n_3\mathbf{c}, \end{aligned} \tag{3.3}$$

with n_1, n_2 and n_3 three specific integers.

3.2 Electronic Properties

To get an idea of the typical electronic behaviour of CrI_3, we perform DFT calculations in order to obtain the density of states (DOS) and the electronic band structure.

The DOS describes how many different states are occupied at each energy level. In figure 3.2, we depict the DOS of monolayer CrI_3 in proximity of the Fermi level. The Fermi level itself is set to zero to serve as a reference. After all, energy has no absolute zero, only differences in energy are physically meaningful. Notice that we switched on the SOC, the electrons now have a preferential spin orientation, and only states with this spin orientation will be occupied. In the same figure, we also plotted the DOS for the most important atomic orbitals which are the d-orbitals

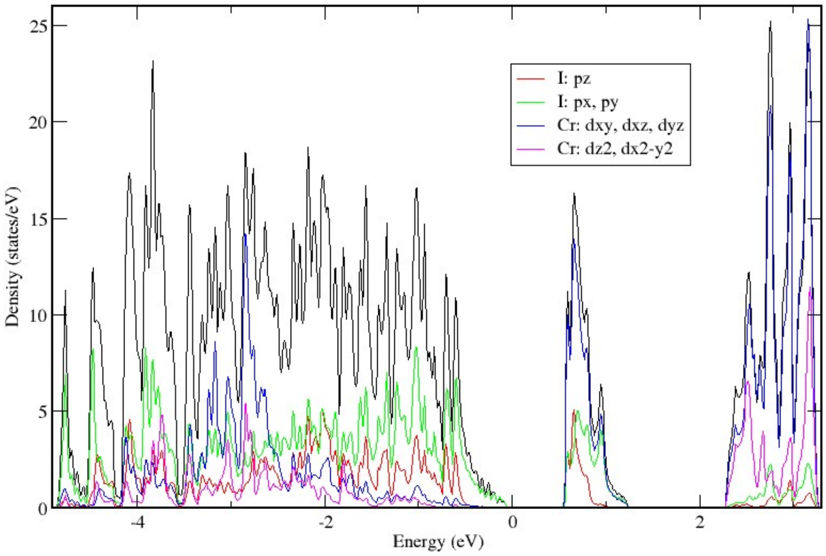

FIGURE 3.2: **Density of States of a CrI_3 monolayer.** The graph contains the DOS of the energy levels close to the Fermi level. The graph contains both the total DOS (black) as the DOS for several orbitals (in colour). The energy of the Fermi level is set as zero as a reference. Figure is plotted with P4VASP and XmGrace.

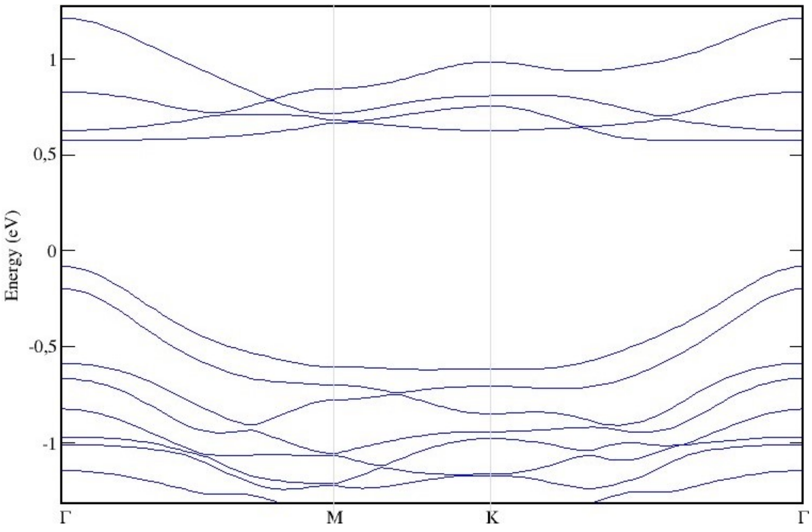

FIGURE 3.3: **Band structure of a CrI$_3$ monolayer.** The graph contains the band structure of monolayer CrI$_3$ close to the Fermi level. The energy of the Fermi level is set as zero as a reference. Figure is plotted with P4VASP and XmGrace.

of the chromium atoms and the p-orbitals of the iodine atoms. Orbitals that are degenerate are plotted together[62]. We clearly see that the p$_x$ and p$_y$ orbitals of the iodine atoms (green plot) dominate the valence band maximum. The p$_z$ orbital of the iodine atom (red plot) and the d-orbitals of the chromium atoms (blue- and magenta plots) reside mostly in the middle of the valence band. In the conduction band, the d$_{xy}$, d$_{xz}$ and d$_{yz}$ orbitals (blue plot) are the most important orbitals. Qualitatively, these results are in relatively good agreement with earlier published articles[62].

In figure 3.3, we depict the band structure of a CrI$_3$ monolayer near the Fermi level. Again, we set the Fermi level to zero as a reference. Our calculations suggest that monolayer CrI$_3$ has a direct bandgap at the gamma point of 0.657 eV. This is in relatively good agreement with some values in literature, e.g. Webster et al. report a direct bandgap at the gamma point of 0.890 eV for a FM monolayer with SOC[63]. This small bandgap suggests that a FM CrI$_3$ monolayer possesses semiconducting properties.

3.3 Magnetic Properties

In chapter 1, we already briefly discussed some experimental findings regarding the magnetic properties of CrI$_3$. Experimental data suggests that monolayer CrI$_3$ displays a strongly anisotropic FM behaviour with an out-of-plane spin polarization, and a Curie temperature of T_c = 45 K. The magnetic moments on the chromium atoms have a magnitude of 3 μ_B, while the iodine atoms are non-magnetic. In this section, we try to confirm the experimentally observed behaviour by performing some theoretical calculations. First, we apply the 4SM methodology to the CrI$_3$ monolayer to obtain the magnetic exchange parameters. These parameters model the interaction between the spins in our material. Afterwards, we perform a temperature dependent simulation of the spin dynamics to determine the magnetic groundstate of the system and the Curie temperature. Finally, we also briefly discuss the behaviour of spin waves in monolayer CrI$_3$.

3.3.1 Magnetic Parameters

For the 4SM calculations, we enlarge the unit cell to a 2 × 2 × 1 supercell as is depicted in figure 3.4. All the chromium atoms are labelled to differentiate between different spin sites. We will calculate all possible exchange parameters between different nearest neighbouring spin site pairs. Notice that, due to the symmetry of the crystal, many of these pairs are identical. For instance, the 1-2 pair and the 7-8 pair are identical. All other equalities between pairs are mentioned on the right of figure 3.4. There are three different exchange matrices left to calculate. Namely, the parameters between the 1-2 pair, the 2-3 pair and the 2-5 pair. The bonds between these three pairs, and all bonds identical to them, are coloured in green, blue and red respectively on figure 3.4. Due to the 3-fold symmetry in the crystal, it suffices to calculate only one exchange matrix. For instance, it suffices to calculate the matrix associated with the interaction between the 1-2 pair, and then perform rotations over 120 degrees and 240 degrees to obtain the other two exchange matrices.

To obtain the exchange parameters, we follow the procedure derived in section 2.1.2. The energies of four different spin configurations of the system are calculated and mapped on the corresponding Heisenberg Hamiltonian. From the resulting system of equations, we can derive one exchange matrix element. If we repeat this procedure for all nine matrix elements, we obtain the following exchange matrix:

$$J_{12} = \begin{bmatrix} -4.34 & 0.00 & 0.00 \\ 0.00 & -3.24 & -0.65 \\ 0.00 & -0.65 & -3.96 \end{bmatrix}, \tag{3.4}$$

in which every value is expressed in meV. Notice that the exchange parameters are either zero or negative. In principle, we can calculate the 2-3 and 2-5 pairs from the 1-2 pair by performing rotations. However, we calculated the 2-3 pair to check the

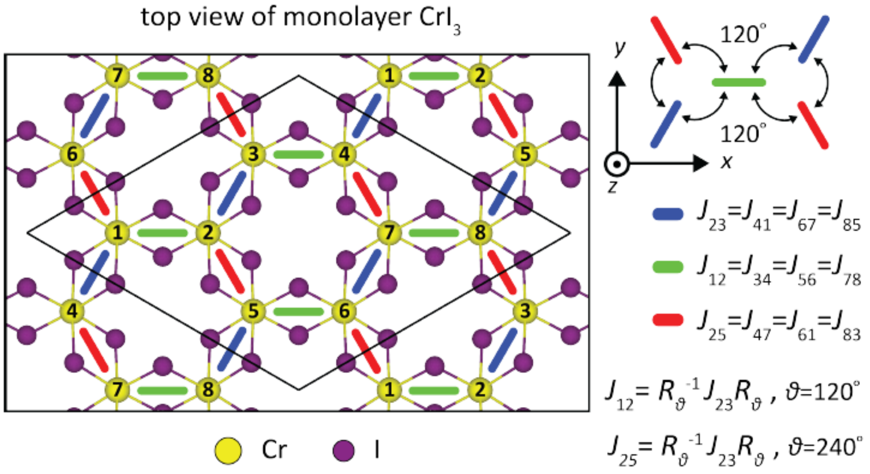

FIGURE 3.4: **Labelled spin sites in a CrI$_3$ monolayer.** Top view of a CrI$_3$ monolayer's crystal structure. Chromium and iodine atoms are represented by yellow and purple spheres respectively. The chromium atoms are labelled to differentiate between different spin sites. The 2 × 2 × 1 supercell is marked with black lines. On the right, three Cr-Cr bonds connected with 3-fold in-plane symmetry are shown as blue, green, and red bars with their respective magnetic exchange matrices. Figure from reference: [42].

validity of this rotation. The exchange matrix for the 2-3 pair is given by:

$$J_{23} = \begin{bmatrix} -3.53 & -0.50 & -0.57 \\ -0.50 & -4.07 & 0.33 \\ -0.57 & 0.33 & -3.97 \end{bmatrix}, \tag{3.5}$$

again with all the values expressed in meV. These values are in relatively good agreement with the matrices calculated from the 1-2 pair by rotation:

$$J_{23} = \begin{bmatrix} -3.52 & -0.48 & -0.56 \\ -0.48 & -4.07 & 0.33 \\ -0.56 & 0.33 & -3.96 \end{bmatrix} ; \quad J_{25} = \begin{bmatrix} -3.52 & 0.48 & 0.56 \\ 0.48 & -4.07 & 0.33 \\ 0.56 & 0.33 & -3.96 \end{bmatrix} . \tag{3.6}$$

The mean of the J_{12}, J_{23} and J_{25} matrices can give us effective exchange parameters that are identical for each spin site[62]. This effective exchange matrix, expressed in meV, is equal to:

$$\langle J \rangle = \begin{bmatrix} -3.79 & 0.00 & 0.00 \\ 0.00 & -3.79 & 0.00 \\ 0.00 & 0.00 & -3.96 \end{bmatrix} . \tag{3.7}$$

In all exchange matrices, we observe negative values for the diagonal elements, which suggest a FM interaction between the atoms, i.e. the atomic spins prefer a parallel orientation.

Notice that all three the exchange matrices are symmetric. As a consequence, all DMI parameters (i.e. the anti-symmetric exchange parameters) will be equal to zero as can be seen from the formula presented in section 2.1.3. This is due to the inversion symmetry of the crystal. As long as there are no external forces that break the inversion symmetry, the CrI_3 monolayer will have a DMI equal to zero.

As discussed in section 2.1.4, the crystal symmetry assures that we only need to calculate one SIA parameter instead of the full 3 × 3 SIA matrix. This parameter is equal to $A_{ii}^{zz} = -0.08$ meV. A negative SIA parameter indicates that the out-of-plane direction is the preferential orientation for the spins.

In section 1.1.3, we argued that the anisotropy in the exchange has a more important contribution to the magnetic anisotropy of the crystal than the SIA. The anisotopic exchange is indeed equal to $\Delta = \langle J \rangle^{zz} - \langle J \rangle^{xx} = \langle J \rangle^{zz} - \langle J \rangle^{yy} = -0.17$ meV, which is significantly bigger than the SIA. This value is also negative which again confirms the fact that the spins prefer to orient themselves along the z-direction.

3.3.2 Equilibrium Magnetization

To obtain the ground-state spin configuration and the Curie temperature of the system, we perform simulations using the Spirit software. In CrI_3, the chromium atoms are magnetic while the iodine atoms are non-magnetic. Therefore, we only need to include the chromium atoms in the Spirit calculations. These chromium atoms form a hexagonal 2D spin lattice. Each unit cell contains two chromium atoms, i.e. two spin sites. The simulations are performed on a 24 × 24 × 1 supercell to include enough atoms in the lattice. In figure 3.5, we plot the ground-state spin configuration of the lattice. The spins are represented with coloured arrows. The direction of the arrows mark the directions of the spins and the colour of the arrows represents the inclination of the spins with respect to the 2D plane. The colours of the spins follow the order of the colours on a rainbow (red, orange, yellow, green, blue, indigo

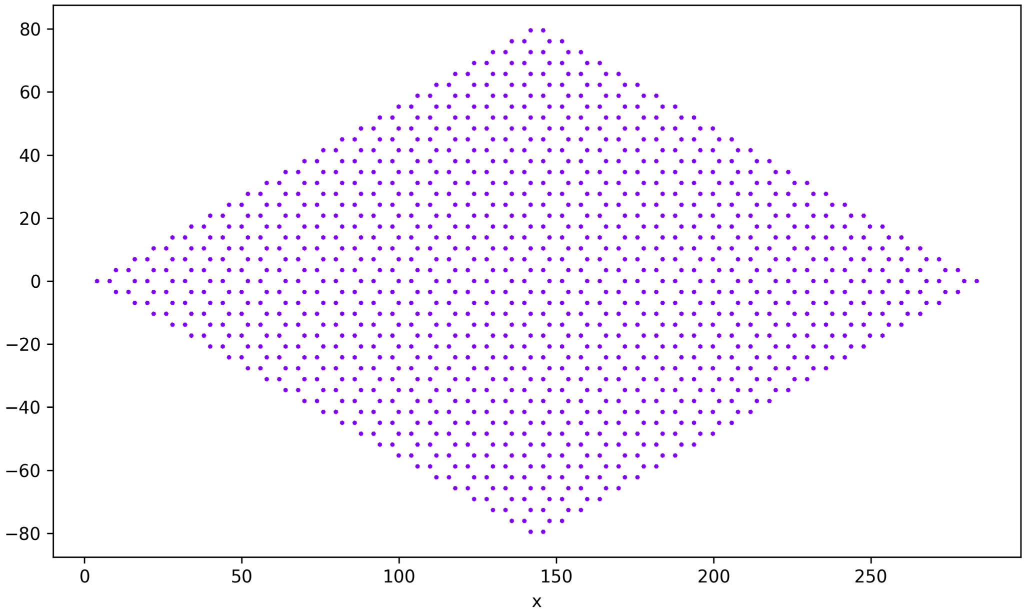

FIGURE 3.5: **Ground-state spin configuration of a CrI_3 monolayer.** The figure contains the spin-lattice for a CrI_3 monolayer. Only the magnetic atoms, i.e. the chromium atoms, are represented in the picture. The figure represents a 24 × 24 × 1 supercell, each unit cell contains two chromium atoms. All spins have a violet colour, this means that all the spins have a downwards out-of-plane orientation.

and violet). If the spins are oriented entirely upwards, they are coloured red, if they are pointed entirely downwards, they are coloured violet. Spins with an in-between orientation possess intermediate colours depending on their respective orientation, e.g. orange arrows have a more upwards inclination while blue arrows have a more downward inclination. Since the spins are represented as violet dots, we know they are pointed downwards in the out-of-plane direction, which is in agreement with our expectations based on the material's magnetic parameters (see previous section) and experimental observations[8]. Let's conclude this section by noting that the upwards- and downwards out-of-plane directions are energetically degenerate in a CrI_3 monolayer. After a simulation, the system will end up in one or the other depending on the random initial positions. Since there is no DMI in CrI_3 monolayers, and since our spin configuration matches experimental observations, we can be pretty sure of the fact that the spin configuration found in our simulation is indeed the ground-state of the material and not a metastable state.

3.3.3 Curie Temperature

To obtain the Curie temperature, we need to perform a temperature dependent simulation. The simulation starts off with a random spin configuration at a temperature of $T = 60$ K. In steps of 0.25 K, the temperature decreases to absolute zero. In each temperature step, we solve the LLG equation to obtain the spin configuration and magnetization of the system. The simulation is again performed with the Spirit software on a 24 × 24 × 1 supercell. More computational details can be found in section B of the appendix. In figure 3.6, the magnetization of the system is plotted as a function of the temperature. On the left panel of the figure, we see that the Cartesian components of the magnetization are plotted as a function of the temperature. The calculation starts off at a temperature of $T = 60$ K with all the spins oriented in a

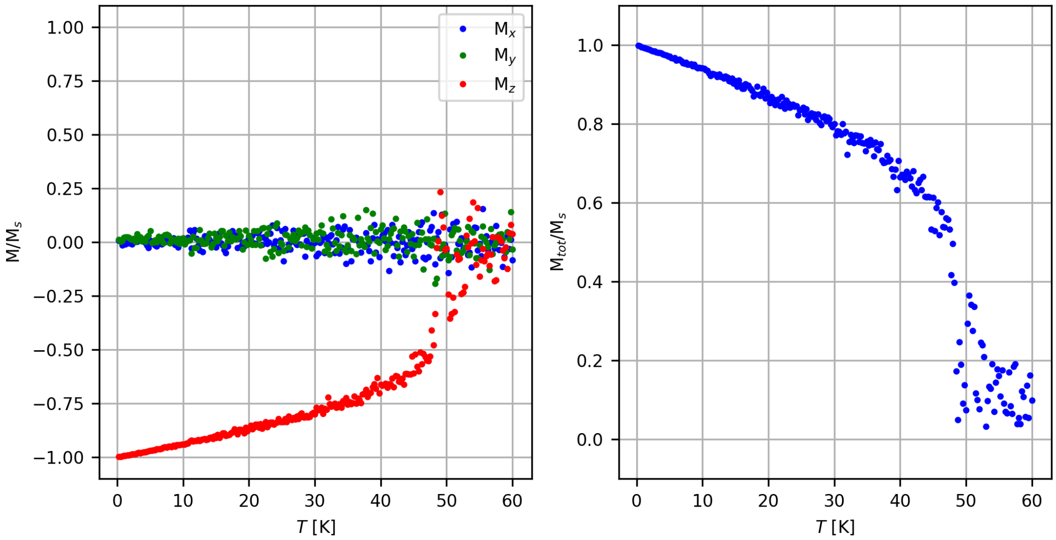

FIGURE 3.6: **Magnetization of a CrI$_3$ monolayer as a function of the temperature.** On the left panel of the figure, the three Cartesian components of the magnetization are depicted as a function of the temperature. The sign of the magnetization denotes the direction of the magnetization relative to the Cartesian axes. On the right panel of the figure, the total magnetization of the system is depicted as a function of the temperature. In both panels, the magnetization is portrayed relative to the saturation magnetization.

random direction. If there are enough spins in the system, the magnetization along each Cartesian axis will average out close to zero. Consequently, the total magnetization of the system, displayed on the right panel of figure 3.6, will also be close to zero. If the temperature decreases, we see that the magnetization in the x- and y-directions approach closer and closer to zero, meanwhile more and more spins orient themselves along the z-axis which results in an increase in magnetization in this direction. Consequently, also the total magnetization of the system will increase with decreasing temperature. The temperature where the magnetization will start to increase rapidly is called the Curie temperature. Below this temperature, the material is magnetic, above this temperature, the material is non-magnetic. Our simulation places the Curie temperature at 48 K which is in relatively good agreement with the Curie temperature of 45 K observed in experiments[8]. Below the Curie temperature the magnetization keeps increasing. At absolute zero, the total magnetization is equal to one, i.e. the magnetization is fully saturated. At this point, the magnetization in the x- and y-directions are equal to zero while the magnetization in the z-direction is equal to minus one. All the spins will now be oriented downwards in the out-of-plane direction, i.e. the state depicted in figure 3.5. Since there is no DMI in CrI$_3$ monolayers, there will be no in-plane components (x- and y-components) of the magnetization.

3.3.4 Spin Waves

To study the spin waves in monolayer CrI$_3$, we artificially create a sinusoidal in-plane oscillating field applied in a narrow rectangular region of the material and then check how the waves propagate through the material[41] (for more computational details see section B of the appendix). In figure 3.7, we show the propagation of a spin wave generated by an oscillating magnetic field with a frequency of 0.6 THz

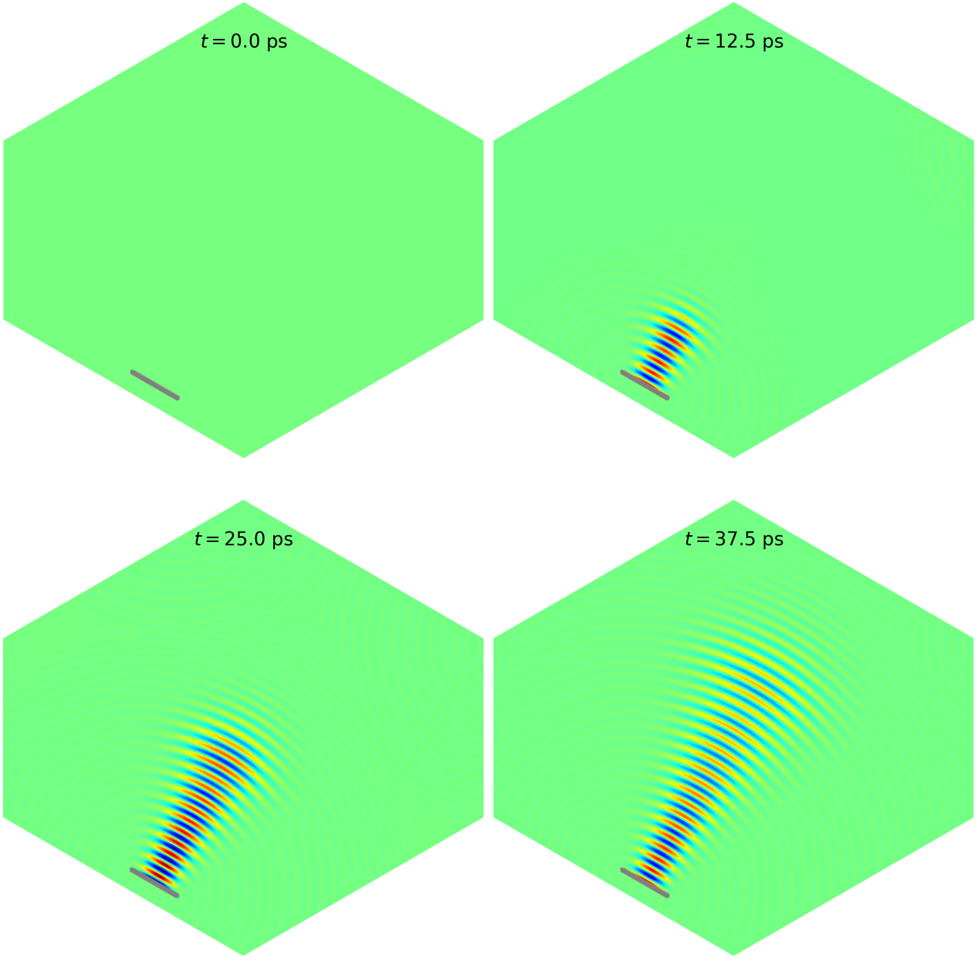

FIGURE 3.7: **Propagation of spin waves in monolayer CrI$_3$.** Four figures showing the propagation of a spin wave through the crystal at four different times (between 0.0 ps and 37.5 ps at intervals of 12.5 ps). The material is depicted in green, the spin wave is depicted alternatingly in blue and red representing the oscillations of the spins. The spin wave is created in the grey rectangular region marked on the figure by an oscillating magnetic field with a frequency of 0.6 THz.

at four different times in the simulation, i.e. between 0.0 ps and 37.5 ps in intervals of 12.5 ps. The spin wave is represented alternatingly in blue and red representing the oscillations of the spins.

The frequency f and and wavelength λ of the spin wave can be calculated by plotting the magnetization as function of respectively time and space and subsequently fitting a sine function to that data[41]. As an example we show how this is done for a spin wave with a frequency of 0.6 THz in figure 3.8. From the wavelength λ we can calculate the wavector k through $k = 2\pi/\lambda$. In a similar fashion, we can determine the frequency and wavevectors for spin waves with various initial frequencies. Plotting the frequency as a function of these wavevectors gives us the dispersion relation for spin waves in monolayer CrI$_3$ which is depicted in figure 3.9. The solid line in this figure represents a quadratic fit to the data according to the expression $f(k) = Ak^2 + f_0$, in which A and f_0 are two fitted parameters with f_0 representing the zero-momentum spin wave mode[41]. The quadratic dispersion is in agreement with the spin wave modes that have been observed experimentally with Raman spectroscopy[40]. The dispersion depicted in figure 3.9 corresponds to the lower energy magnon mode with spins that oscillate in-phase (see also section 1.2.4). Simulations show that the spin wave dispersion relation in CrI_3 can be tuned through a large range of frequencies by applying strain on the structure which creates opportunities for possible magnonic applications[41].

The results presented in this section are a reproduction of original calculations done by Rai Menezes and published in reference [41].

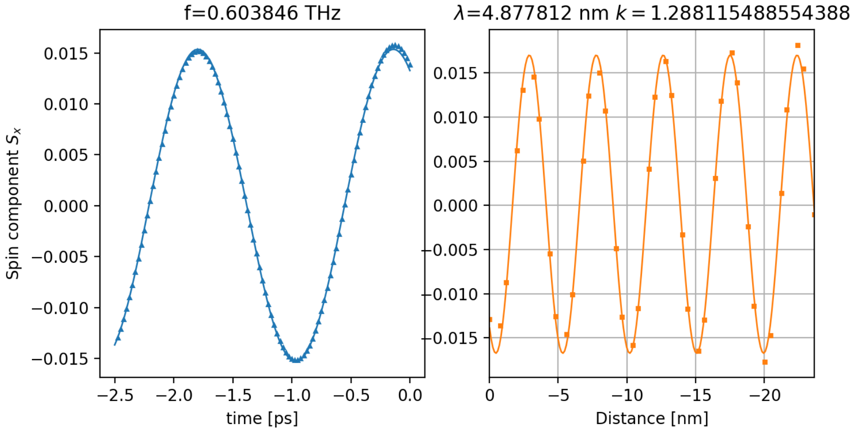

FIGURE 3.8: **Spin component S_x as a function of time and space for a spin wave with a frequency of 0.6 THz.** The left figure depicts the S_x component of the spin as a function of time at different time steps during the simulation (blue dots). Similarly, the right figure contains data points for the S_x component of the spin as a function of the distance travelled by the spin wave. In both figures, a sine wave was plotted to the data to calculate the frequency f, wavelength λ and corresponding wavevector k of the spin wave.

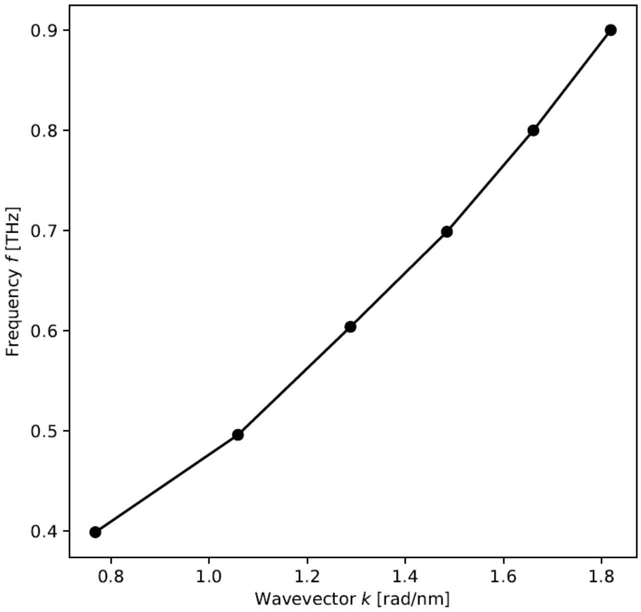

FIGURE 3.9: **Spin wave dispersion relation for monolayer CrI_3.** The figure depicts the frequency f of a spin wave as a function of the wavevector k for six different frequencies (black dots). The black solid line represents a numerical quadratic fit to the data.

Chapter 4

Bilayer

4.1 Stacking

Multilayer CrI_3 can be constructed by stacking multiple monolayers on top of each other. For a CrI_3 bilayer, there are at least two different stable structural phases of the material that have been observed experimentally, the LT phase and the HT phase, each one with another stacking order of the layers. In the LT rhombohedral phase, the layers are stacked in a way that place the chromium atoms in one layer above a hole in the chromium honeycomb of the adjacent layers[6]. One can transform the LT rhombohedral phase to the HT monoclinic phase by sliding one of the layers by a distance of $a/3$ along the in-plane lattice vectors[64], with a the lattice constant of the material. The crystal structures of the LT- and HT phases are depicted in figure 4.1.

From the previous chapter, it became clear that a CrI_3 monolayer has a FM ground-state with an out-of-plane spin polarisation. If we stack two monolayers on top of each other, we can stack them either with their spins pointed in the same direction,

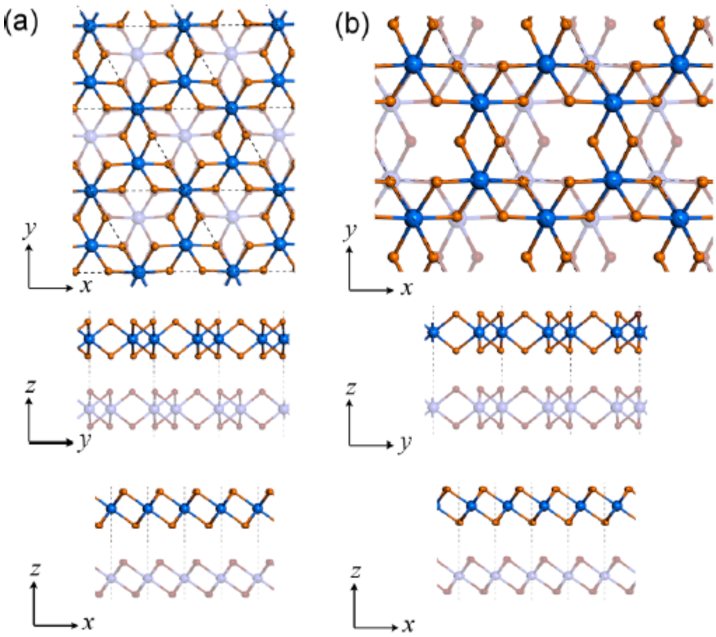

FIGURE 4.1: **Crystal structure of the LT- and HT phases of a CrI_3 bilayer.** Top and sideways views of a CrI_3 bilayer in the LT phase (a) and the HT phase (b). Chromium and iodine atoms are depicted with blue and purple spheres respectively. The atoms in the bottom layer have been faded out to create some contrast with the atoms in the upper layer. Figure from reference: [64].

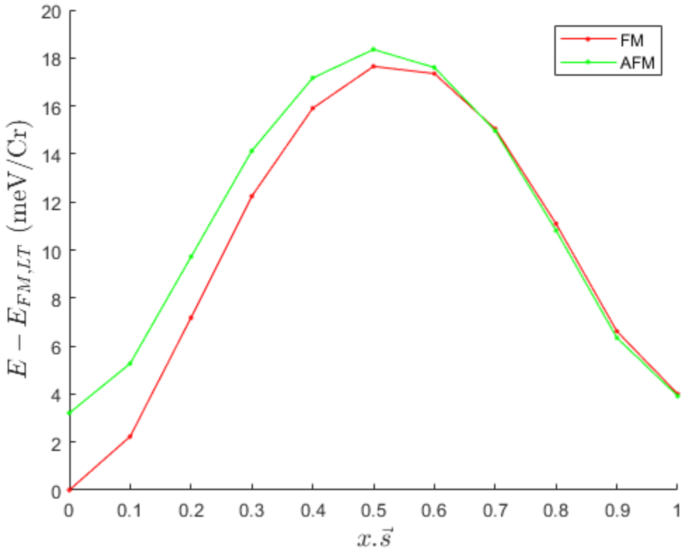

FIGURE 4.2: **Transition pathway between the LT- and HT phase of a FM- and an AFM CrI_3 bilayer.** The energy per chromium atom is plotted as a function of the transition pathway, the energy of the FM configuration in the LT phase is chosen as a reference. The LT phase is located at $x \cdot \mathbf{s} = 0$, the HT phase at $x \cdot \mathbf{s} = 1$.

giving rise to a FM bilayer, or with their spins pointed in opposite directions, giving rise to an AFM bilayer with zero net magnetization. So, in a CrI_3 bilayer each individual layer possesses FM order with its spins oriented perpendicular to the atomic planes, however, the overall phase of the bilayer could be either FM or AFM. The latter will be determined by the phase of the material. As illustrated in figure 4.2, the LT phase favours a FM interlayer coupling, meanwhile the HT phase prefers an AFM configuration. The figure can be interpreted as follows. We start off from a bilayer in the LT phase and transform it to the HT phase by sliding the upper layer along the **b** lattice vector with a vector **s** of length $a/3$. The transition occurs in ten steps, in each step we calculate the energy of the system. We performed this transformation both for a FM and an AFM bilayer. The transition pathway for the FM and the AFM bilayers are plotted in red and green respectively. We set the energy of the FM bilayer in the LT phase to zero as a reference. The graph confirms that both the LT and the HT phases are stable configurations of the crystal, both configurations occur at minima in the energy and are separated by an energy barrier. This figure also predicts that the LT phase is more stable than the metastable HT phase, which is in agreement with experimental results[6]. For the LT phase, the FM bilayer is 3.21 meV/Cr atom more stable than the AFM bilayer, the LT phase clearly favours a FM spin configuration. In the HT phase, the difference is way smaller, here the AFM phase is 0.084 meV/Cr atom more stable than the FM phase. MOKE measurements on HT bilayer CrI_3 indeed confirm this AFM phase[8]. The most important result to take away from this graph is that the magnetic ground-state of a CrI_3 bilayer can, indeed, be tuned by the stacking order of the layers. Qualitatively, our results are in good agreement with earlier publications also based on ab initio calculations[64].

Next to the LT- and the HT phases, we will also consider an AA-stacking of the layers. In an AA-stacked bilayer, every atom in the upper layer is stacked directly above an identical atom in the bottom layer. Ab initio calculations show that an AA-stacked bilayer prefers a FM spin configuration which is 0.199 meV/Cr atom more

TABLE 4.1: **Structural parameters of bilayer CrI_3 in its different stacking orders.** For both the FM as the AFM phases of the three stacking orders, the table contains values for the lattice constant, the Cr-I distance, the Cr-I-Cr bonding angle, and the interlayer distance.

		a (Å)	$d_{\mathrm{Cr-I}}$ (Å)	θ (°)	d_{layer} (Å)
LT	FM	6.915	2.77	92.43	0.90
	AFM	6.914	2.76	92.43	0.91
HT	FM	6.913	2.76	92.42	0.92
	AFM	6.914	2.76	92.45	0.92
AA	FM	6.908	2.76	92.31	0.97
	AFM	6.907	2.76	92.29	0.97

stable than AFM phase.

Table 4.1 contains some structural parameters for the optimized geometries of the LT, HT and AA bilayers in both the FM and AFM phases. The structures were optimized with DFT calculations. The parameters for the LT and HT phase are quite similar, meanwhile the parameters for the AA bilayer are slightly different. Since the atoms in the AA-stacked bilayer are directly on top of each other, the interlayer distance d_{layer} is a little bigger to keep enough distance between the atoms. The AA bilayer also has a smaller lattice constant a, and consequently, the Cr-I-Cr angle θ is smaller. The bond length between the chromium and iodine atoms $d_{\mathrm{Cr-I}}$ was almost identical in all structures.

4.2 Magnetic Properties

4.2.1 Magnetic Parameters

The magnetic parameters for the CrI_3 bilayers are calculated with the 4SM method. The calculations are performed for the LT-phase and the HT-phase in both the FM and AFM configurations, and for the AA-phase in the FM configuration. Due to the crystal symmetry in the monolayer case, we could limit ourselves to calculating only one exchange matrix and the other matrices could be derived by performing rotations. In the bilayer case, this rotational symmetry is absent which leads to a bigger number of parameters that needs to be calculated.

LT-bilayer

In the 4SM calculations, we enlarge the unit cell to a 2 × 2 × 1 supercell as depicted in figure 4.3. The figure contains a top view and sideways view of the LT-phase bilayer. Since only the chromium atoms are magnetic, we left the iodine atoms and the atomic bonds out of the picture for the sake of simplicity. The supercell contains 16 chromium atoms in total. To make a clear distinction between the chromium atoms in the top- and bottom layers, they are coloured in green (atoms 1-8) and yellow (atoms 9-16) respectively. Every spin site in the supercell is assigned a label. In the LT-bilayer case, we need to calculate seven exchange matrices, six matrices that model the intra-layer exchange (three in the top layer and three in the bottom layer) and one matrix that models the inter-layer interaction. In the top layer, we calculate the exchange matrices for the 2-1, 2-3 and 2-5 pairs, in the bottom layer, the 10-9, 10-11 and 10-13 pairs, and for the inter-layer interaction, the 2-9 pair. Notice that only the interactions between intra-layer nearest neighbours and inter-layer

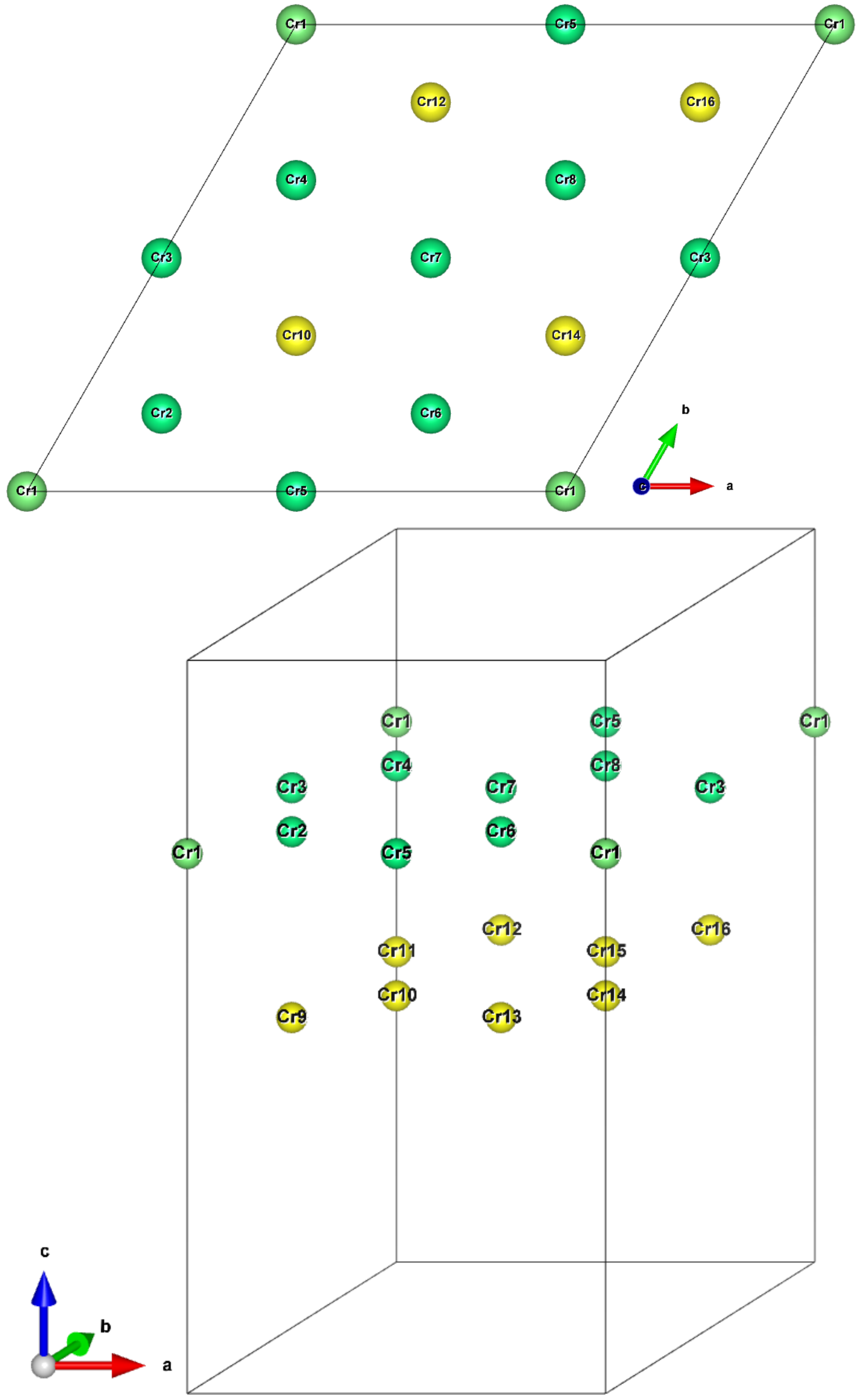

FIGURE 4.3: **Labelled spin sites in a CrI_3 bilayer in the LT-phase.** Top view and sideways view of a CrI_3 bilayer in the LT-phase. The iodine atoms and the bonds are left out of the figure for simplicity. Chromium atoms from the upper layer are coloured in green, atoms from the bottom layer are coloured in yellow.

TABLE 4.2: **Magnetic parameters of a CrI$_3$ bilayer in the LT-FM phase.** The table contains the exchange matrices, the DMI vectors and a SIA parameter for seven distinct spin pairs. The 1-2, 2-3 and 2-5 pairs model the intra-layer interaction in the top layer. The 9-10, 10-11 and 10-13 pairs model the intra-layer interaction in the bottom layer. The 2-9 pair model the inter-layer interaction.

	J_{i-j} (meV)				$\mathbf{D}_{i-j}$ (meV)	A_{ii}^{zz} (meV)
J_{1-2}	-4.63	-0.04	-0.13	$\mathbf{D}_{1-2}$	0.00	-0.07
	0.03	-3.56	-0.64		0.12	
	0.11	-0.64	-4.25		-0.03	
J_{2-3}	-3.43	-0.47	-0.54	$\mathbf{D}_{2-3}$	-0.04	-0.07
	-0.43	-3.93	0.26		0.02	
	-0.50	0.34	-3.86		-0.02	
J_{2-5}	-3.84	0.49	0.50	$\mathbf{D}_{2-5}$	0.10	-0.07
	0.53	-4.34	0.42		0.05	
	0.61	0.22	-4.25		-0.02	
J_{2-9}	-0.26	0.06	0.01	$\mathbf{D}_{2-9}$	0.00	-0.07
	0.06	-0.27	0.01		0.00	
	0.02	0.01	-0.30		0.00	
J_{9-10}	-4.61	0.00	0.12	$\mathbf{D}_{9-10}$	0.00	-0.07
	0.05	-3.53	-0.64		-0.12	
	-0.12	-0.64	-4.23		-0.02	
J_{10-11}	-3.42	-0.43	-0.50	$\mathbf{D}_{10-11}$	0.04	-0.07
	-0.49	-3.92	0.34		-0.03	
	-0.56	0.26	-3.86		0.03	
J_{10-13}	-3.84	0.53	0.61	$\mathbf{D}_{10-13}$	-0.10	-0.07
	0.47	-4.34	0.22		-0.05	
	0.50	0.43	-4.25		0.03	

nearest neighbours are taken into account. The results for the exchange matrices are depicted in tables 4.2 and 4.3 for respectively the FM and the AFM cases.

In all exchange matrices, all the diagonal elements are negative. This means that that the interaction between the spins will be FM, i.e. the spins prefer to align parallel to each other. As expected, the inter-layer interaction (the 2-9 pair) is significantly smaller than the intra-layer interactions.

In the monolayer case, all exchange matrices were symmetric resulting in a zero net DMI. For the LT bilayer, there will be a non zero DMI due to some asymmetry in the exchange matrices. However, the resulting DMI is rather small and, therefore, the effect on the magnetization will also be very small. The non-zero DMI results from the breaking of inversion symmetry in CrI$_3$ bilayers.

Further, notice that the SIA parameter will has similar values for both the bilayer and the monolayer cases. The negative values again indicate that the out-of-plane direction is the preferential orientation of the spins.

Finally, notice that we found very similar values for both the FM- and AFM cases. Especially the parameters for the intra-layer exchange interaction, the DMI and the SIA are almost exactly the same in both cases. Only for the J_{2-9}^{zz} parameter, i.e. the interlayer interaction, the difference between the values was bigger. In the FM case we found a value of -0.30 meV, in the AFM case the parameter was equal to -0.17 meV. This difference might explain why the LT bilayer prefers a FM spin configuration.

TABLE 4.3: **Magnetic parameters of a CrI$_3$ bilayer in the LT-AFM phase.** The table contains the exchange matrices, the DMI vectors and a SIA parameter for seven distinct spin pairs. The 1-2, 2-3 and 2-5 pairs model the intra-layer interaction in the top layer. The 9-10, 10-11 and 10-13 pairs model the intra-layer interaction in the bottom layer. The 2-9 pair model the inter-layer interaction.

J_{i-j} (meV)				$\mathbf{D}_{i-j}$ (meV)		A_{ii}^{zz} (meV)
J_{1-2}	-4.61	-0.04	-0.13	$\mathbf{D}_{1-2}$	0.00	-0.06
	0.03	-3.53	-0.63		0.12	
	0.12	-0.63	-4.23		-0.04	
J_{2-3}	-3.82	-0.44	-0.60	$\mathbf{D}_{2-3}$	-0.10	-0.08
	-0.52	-4.36	0.22		0.06	
	-0.48	0.43	-4.24		0.04	
J_{2-5}	-3.83	0.52	0.49	$\mathbf{D}_{2-5}$	0.11	-0.08
	0.45	-4.35	0.42		0.06	
	0.61	0.21	-4.24		0.04	
J_{2-9}	-0.25	0.00	0.00	$\mathbf{D}_{2-9}$	0.00	-0.08
	0.00	-0.25	0.00		0.00	
	0.00	0.00	-0.17		0.00	
J_{9-10}	-4.61	0.03	0.13	$\mathbf{D}_{9-10}$	0.00	-0.07
	-0.04	-3.54	-0.63		-0.13	
	-0.13	-0.64	-4.23		0.03	
J_{10-11}	-3.82	0.51	-0.48	$\mathbf{D}_{10-11}$	0.10	-0.06
	-0.44	-4.36	0.42		-0.06	
	-0.60	0.22	-4.24		-0.04	
J_{10-13}	-3.83	0.45	0.61	$\mathbf{D}_{10-13}$	-0.10	-0.06
	0.52	-4.34	0.21		-0.06	
	0.49	0.42	-4.24		-0.04	

HT-bilayer

For the HT bilayer case, we again perform our calculations in a 2 × 2 × 1 supercell as depicted in figure 4.4. The figure contains top- and sideways views of a CrI$_3$ bilayer in the HT-phase. Again, we leave the iodine atoms and the bonds out of the picture to simplify the figure. This is justified by the fact that only the chromium atoms are magnetic. The supercell contains 16 chromium atoms in total. To make a clear distinction between the chromium atoms in the top- and bottom layers, the top-layer atoms are coloured in green (atoms 1-8) while the bottom-layer atoms are coloured in yellow (atoms 9-16). Every spin site in the supercell is assigned a label. In the monolayer case, we only had to calculate one exchange matrix due to the crystal symmetry. In the LT bilayer this number grew to seven exchange matrices to account for all the interactions. In the HT bilayer, this extends even further to ten pairs. This is due to the fact that for the interlayer interaction, we only include the interactions between the nearest neighbouring spins, and in the HT-phase there are multiple atoms in the top- and bottom layer at the same distance. Therefore, we now have to calculate four inter-layer exchange matrices, i.e. for the 1-9, 2-9, 2-10 and 5-10 pairs. Like earlier, we have six matrices that model the intra-layer exchange interaction, three in the top layer (the matrices associated with the 1-2, 2-3 and 2-5 pairs) and three in the bottom layer (the matrices associated with the 9-10, 10-11 and 10-13 pairs). Both for the intra-layer interaction as the inter-layer interaction,

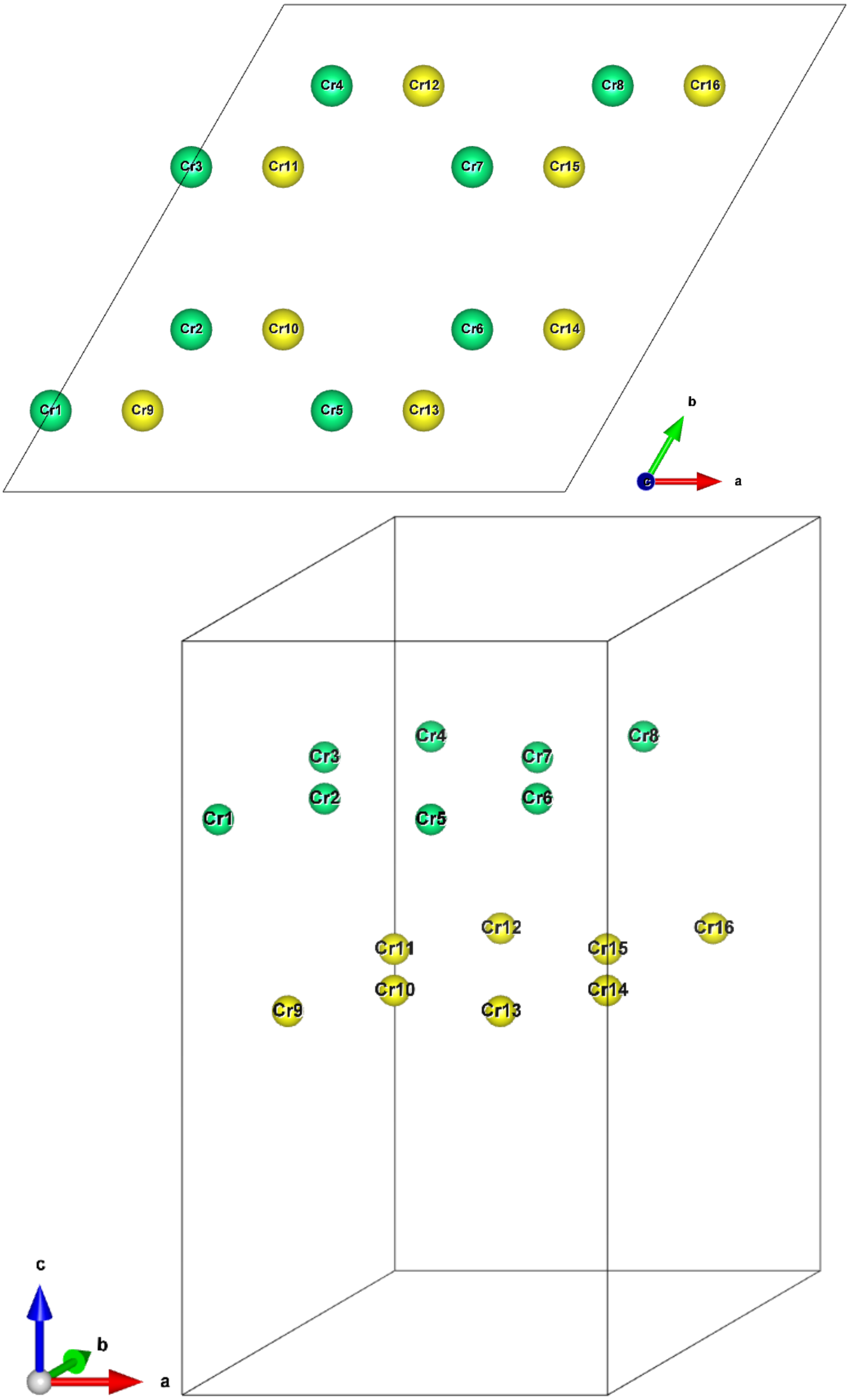

FIGURE 4.4: **Labelled spin sites in a CrI$_3$ bilayer in the HT-phase.** Top view and sideways view of a CrI$_3$ bilayer in the HT-phase. The iodine atoms and the bonds are left out of the figure for simplicity. Chromium atoms from the upper layer are coloured in green, atoms from the bottom layer are coloured in yellow.

TABLE 4.4: **Magnetic parameters of a CrI_3 bilayer in the HT-FM phase.** The table contains the exchange matrices, the DMI vectors and a SIA parameter for ten distinct spin pairs. The 1-2, 2-3 and 2-5 pairs model the intra-layer interaction in the top layer. The 9-10, 10-11 and 10-13 pairs model the intra-layer interaction in the bottom layer. The 1-9, 2-9, 2-10 and 5-10 pairs model the inter-layer interaction.

	J_{i-j} (meV)				$\mathbf{D}_{i-j}$ (meV)	A_{ii}^{zz} (meV)
J_{1-2}	-4.62	0.04	-0.12	$\mathbf{D}_{1-2}$	-0.01	-0.07
	-0.01	-3.53	-0.65		0.12	
	0.12	-0.64	-4.24		0.03	
J_{1-9}	-0.26	-0.03	-0.05	$\mathbf{D}_{1-9}$	-0.04	-0.07
	-0.06	-0.31	-0.02		0.03	
	0.00	0.06	-0.29		0.01	
J_{2-3}	-3.42	-0.48	-0.54	$\mathbf{D}_{2-3}$	-0.04	-0.07
	-0.44	-3.92	0.27		0.02	
	-0.50	0.34	-3.86		-0.02	
J_{2-5}	-3.83	0.48	0.51	$\mathbf{D}_{2-5}$	0.10	-0.07
	0.53	-4.34	0.42		0.05	
	0.61	0.22	-4.25		-0.02	
J_{2-9}	-0.25	0.04	0.02	$\mathbf{D}_{2-9}$	0.00	-0.07
	0.06	-0.26	0.02		0.00	
	0.02	0.01	-0.29		-0.01	
J_{2-10}	-0.26	-0.05	0.01	$\mathbf{D}_{2-10}$	0.04	-0.07
	-0.04	-0.29	0.06		-0.03	
	-0.05	-0.03	-0.29		-0.01	
J_{5-10}	-0.30	0.03	-0.01	$\mathbf{D}_{5-10}$	0.00	-0.07
	0.03	-0.20	-0.02		0.00	
	0.00	-0.02	-0.30		0.00	
J_{9-10}	-4.61	0.00	0.12	$\mathbf{D}_{9-10}$	0.01	-0.07
	0.05	-3.53	-0.64		-0.12	
	-0.12	-0.65	-4.23		-0.03	
J_{10-11}	-3.43	-0.42	-0.49	$\mathbf{D}_{10-11}$	0.04	-0.07
	-0.49	-3.92	0.35		-0.02	
	-0.54	0.27	-3.86		0.04	
J_{10-13}	-3.83	0.53	0.61	$\mathbf{D}_{10-13}$	-0.10	-0.07
	0.49	-4.33	0.22		-0.05	
	0.51	0.42	-4.24		0.02	

we included only the interactions between nearest neighbours. The results for the exchange matrices can be found in tables 4.4 and 4.3 for respectively the HT-FM and HT-AFM cases.

In both the FM and AFM case, all the diagonal elements in every exchange matrix are negative. This means that the spins in a HT bilayer prefer to orient themselves parallel to each other resulting in a FM spin configuration. This is a surprising result since our DFT calculations portrayed in figure 4.2 suggest that an AFM spin configuration has lower energy than a FM one, more so, an AFM spin configuration has already been observed in the HT bilayer in experiments[8].

As expected the parameters that model the inter-layer interactions are significantly smaller than the parameters that model the intra-layer interactions which was also the case for the LT-bilayer.

TABLE 4.5: **Magnetic parameters of a CrI_3 bilayer in the HT-AFM phase.** The table contains the exchange matrices, the DMI vectors and a SIA parameter for ten distinct spin pairs. The 1-2, 2-3 and 2-5 pairs model the intra-layer interaction in the top layer. The 9-10, 10-11 and 10-13 pairs model the intra-layer interaction in the bottom layer. The 1-9, 2-9, 2-10 and 5-10 pairs model the inter-layer interaction.

	J_{i-j} (meV)				$\mathbf{D}_{i-j}$ (meV)	A_{ii}^{zz} (meV)
J_{1-2}	-4.63	0.06	-0.12	$\mathbf{D}_{1-2}$	-0.01	-0.07
	-0.01	-3.54	-0.66		0.12	
	0.12	-0.64	-4.25		0.03	
J_{1-9}	-0.26	-0.04	-0.05	$\mathbf{D}_{1-9}$	-0.04	-0.07
	-0.05	-0.31	-0.02		0.02	
	0.00	0.06	-0.29		0.00	
J_{2-3}	-3.43	-0.48	-0.54	$\mathbf{D}_{2-3}$	-0.04	-0.07
	-0.44	-3.93	0.26		0.02	
	-0.50	0.34	-3.86		-0.02	
J_{2-5}	-3.85	0.47	0.51	$\mathbf{D}_{2-5}$	0.11	-0.07
	0.54	-4.34	0.43		0.05	
	0.61	0.22	-4.26		-0.03	
J_{2-9}	-0.26	0.05	0.02	$\mathbf{D}_{2-9}$	0.00	-0.07
	0.05	-0.27	0.02		0.00	
	0.02	0.02	-0.28		0.00	
J_{2-10}	-0.26	-0.05	0.00	$\mathbf{D}_{2-10}$	0.04	-0.07
	-0.04	-0.31	0.05		-0.02	
	-0.05	-0.02	-0.29		0.00	
J_{5-10}	-0.31	0.02	-0.01	$\mathbf{D}_{5-10}$	0.00	-0.07
	0.02	-0.22	-0.03		0.00	
	-0.01	-0.02	-0.30		0.00	
J_{9-10}	-4.62	-0.01	0.12	$\mathbf{D}_{9-10}$	0.01	-0.07
	0.05	-3.53	-0.64		-0.12	
	-0.12	-0.66	-4.24		-0.03	
J_{10-11}	-3.43	-0.44	-0.50	$\mathbf{D}_{10-11}$	0.04	-0.07
	-0.48	-3.93	0.34		-0.02	
	-0.54	0.27	-3.86		0.02	
J_{10-13}	-3.84	0.54	0.61	$\mathbf{D}_{10-13}$	-0.10	-0.07
	0.47	-4.34	0.22		-0.05	
	0.51	0.43	-4.25		0.03	

Further, note that both the FM bilayer as well as the AFM bilayer have a non-zero DMI. However, the magnitude of the DMI vector will be rather small and will, therefore, also have a small effect on the magnetization. The DMI in the HT-bilayer is of the same order of magnitude as the DMI in the LT-bilayer. The non-zero DMI results from the breaking of inversion symmetry in CrI_3 bilayers.

The SIA parameter for the HT-bilayer has very similar values as the LT-bilayer and the monolayer. The negative values again indicate that the out-of-plane direction is the preferential orientation of the spins.

Overall, we found very similar values for the FM- and AFM cases. For all interactions, the intra- and inter-layer exchange, the DMI, and the SIA we found very similar results. The fact that these values are very close together seems to confirm our DFT results from earlier, where there is only a very small energy difference between the FM and the AFM case. However, the DFT results suggested that the HT-bilayer would have a AFM interlayer coupling which was not the case in our 4SM analysis. In DFT calculations, the results of a calculation can often be significantly different if the parameters of the calculation are poorly chosen. Since the the FM- and AFM state are so close together in energy it could be the case that small changes in the parameters could (wrongly) favour the FM configuration over the AFM one. A recent paper investigated the influence of several parameters on the final state of the system and, although, they found an AFM groundstate in most cases, there were some instances were the HT-bilayer had an FM ground-state[64]. Additionally, in future research, other methods to calculate the exchange parameters should be solicited to exclude the possibility that the 4SM method is not valid for this system.

AA-bilayer

For the LT- and HT-phases, we calculated the magnetic parameters in both the FM and AFM phases. When comparing these results, it becomes clear the the parameters of the FM- and AFM phases don't differ very much from each other. As such, it suffices to only calculate the parameters for the energetically most favourable of the two. For the AA-stacked bilayer, this is the FM one. In figure 4.5, we depict a top and sideways view of the $2 \times 2 \times 1$ supercell used in our calculations for the AA-bilayer. Like earlier, we left the iodine atoms and the bonds out of the picture for the sake of simplicity. Only the magnetic atoms, i.e. the chromium atoms, are depicted in the figure. The supercell contains 16 chromium atoms in total, the atoms in the top layer are coloured in green (atoms 1-8) while the atoms in the bottom layer are coloured in yellow (9-16). Every spin site is assigned a label. Since we have an AA-stacking, only the atoms in the upper layer are visible from the top view. In contrast with the LT- and HT-bilayers, we now have to calculate eight distinct exchange matrices to fully characterize the magnetic interactions in the lattice. Only interactions between nearest neighbours are considered. Similarly to the two earlier structures, there are six matrices that model the intra-layer interactions, three in the top layer (the matrices associated with the 1-2, 2-3 and 2-5 pairs), and three in the bottom layer (the matrices associated with the 9-10, 10-11 and 10-13 pairs). For the inter-layer interactions we have to calculate two sets of parameters which are associated with the 1-9 and 2-10 pairs. The results from the calculations can be found in table 4.6.

In all exchange matrices (both the intra- as inter-layer), all diagonal elements are negative. This means that the spins in the AA-bilayer prefer a FM spin configuration with parallel oriented spins. This is in agreement with our DFT calculations that suggested that the AA-FM bilayer had lower energy than the AA-AFM one.

As expected, the inter-layer exchange parameters are significantly smaller than the inter-layer ones. However, when we comparing the AA-stacking with the LT- and HT-stacked layers, we see that the inter-layer parameters of the AA-stacking are even smaller than the parameter of the other two phases. This small inter-layer exchange parameter suggests a very weak magnetic coupling between the layers. The weak magnetic interaction might be explained by the bigger inter-layer distance in the AA-stacked bilayer (see table 4.1). A bigger distance between the magnetic atoms means a smaller overlap between the orbitals of these atoms which might explain the weaker magnetic interaction.

The AA-bilayer has a non-zero DMI of the same order of magnitude as the DMI in the LT- and HT-phases. Since this DMI is only small, it will also have a small effect

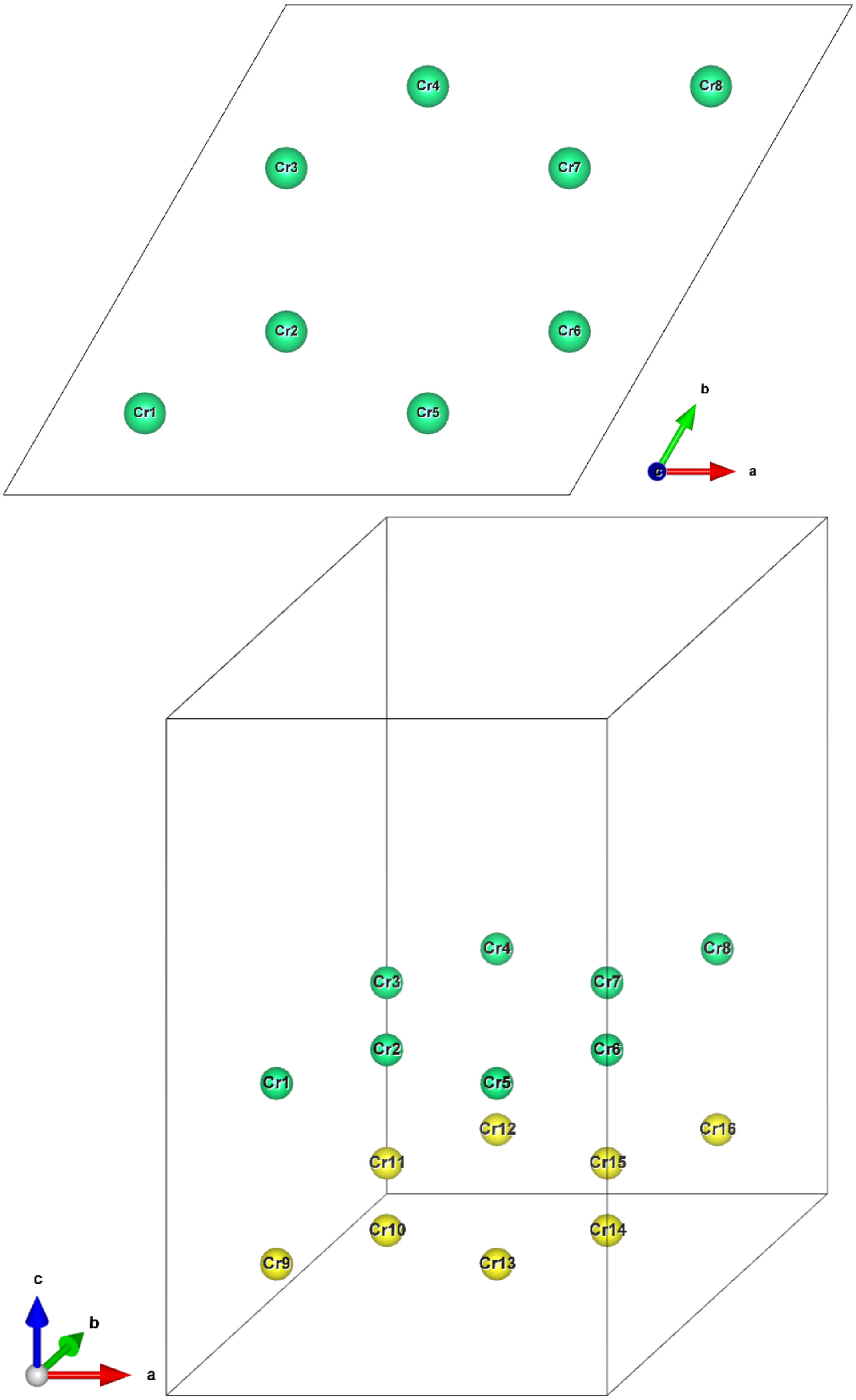

FIGURE 4.5: **Labelled spin sites in a CrI$_3$ bilayer in the AA-phase.** Top view and sideways view of a CrI$_3$ bilayer in the AA-phase. The iodine atoms and the bonds are left out of the figure for simplicity. Chromium atoms from the upper layer are coloured in green, atoms from the bottom layer are coloured in yellow.

TABLE 4.6: **Magnetic parameters of a CrI_3 bilayer in the AA-FM phase.** The table contains the exchange matrices, the DMI vectors and a SIA parameter for eight distinct spin pairs. The 1-2, 2-3 and 2-5 pairs model the intra-layer interaction in the top layer. The 9-10, 10-11 and 10-13 pairs model the intra-layer interaction in the bottom layer. The 1-9 and 2-10 pairs model the inter-layer interaction.

J_{i-j} (meV)				$\mathbf{D}_{i-j}$ (meV)		A^{zz}_{ii} (meV)
J_{1-2}	-4.40	0.04	0.11	$\mathbf{D}_{1-2}$	0.00	-0.08
	-0.04	-3.34	-0.63		-0.11	
	-0.11	-0.63	-4.05		0.04	
J_{2-3}	-3.62	-0.52	-0.49	$\mathbf{D}_{2-3}$	0.10	-0.08
	-0.44	-4.15	0.41		-0.06	
	-0.60	0.22	-4.06		-0.04	
J_{2-5}	-3.62	0.44	0.60	$\mathbf{D}_{2-5}$	-0.10	-0.08
	0.52	-4.15	0.22		-0.05	
	0.49	0.41	-4.06		-0.04	
J_{1-9}	-0.12	-0.06	0.00	$\mathbf{D}_{1-9}$	0.00	-0.08
	0.06	-0.12	0.00		0.00	
	0.00	0.00	-0.04		-0.06	
J_{2-10}	-0.12	0.06	0.00	$\mathbf{D}_{2-10}$	0.00	-0.08
	-0.06	-0.12	0.00		0.00	
	0.00	0.00	-0.04		0.06	
J_{9-10}	-4.41	-0.04	-0.11	$\mathbf{D}_{9-10}$	0.00	-0.08
	0.04	-3.34	-0.62		0.11	
	0.11	-0.62	-4.05		-0.04	
J_{10-11}	-3.62	-0.44	-0.60	$\mathbf{D}_{10-11}$	-0.09	-0.08
	-0.52	-4.15	0.22		0.05	
	-0.49	0.41	-4.06		0.04	
J_{10-13}	-3.62	0.52	0.49	$\mathbf{D}_{10-13}$	0.10	-0.08
	0.44	-4.15	0.41		0.05	
	0.59	0.22	-4.06		0.04	

on the magnetization. The non-zero DMI results from the breaking of inversion symmetry in CrI_3 bilayers.

Also, the SIA is of the same order of magnitude as in all earlier structures. The negative values again indicate that the out-of-plane direction is the preferential orientation of the spins.

4.2.2 Equilibrium Magnetization

To obtain an equilibrium spin configuration of our bilayers, we perform simulations using the Spirit software to solve the LLG equation at absolute zero. Since we're only interested in the behaviour of the magnetic atoms of our material, it suffices to construct a lattice that only contains the chromium atoms, the non-magnetic iodine atoms are neglected. In each layer, the chromium atoms form a 2D hexagonal spin lattice. The simulations are executed on a $24 \times 24 \times 1$ supercell, each of these unit cells contains four chromium atoms, two in each layer. More computational details can be found in section B of the appendix.

At the top of figure 4.6, we depict an equilibrium spin configuration of a bilayer in the HT-phase. All the spins are coloured in violet. Remember from previous

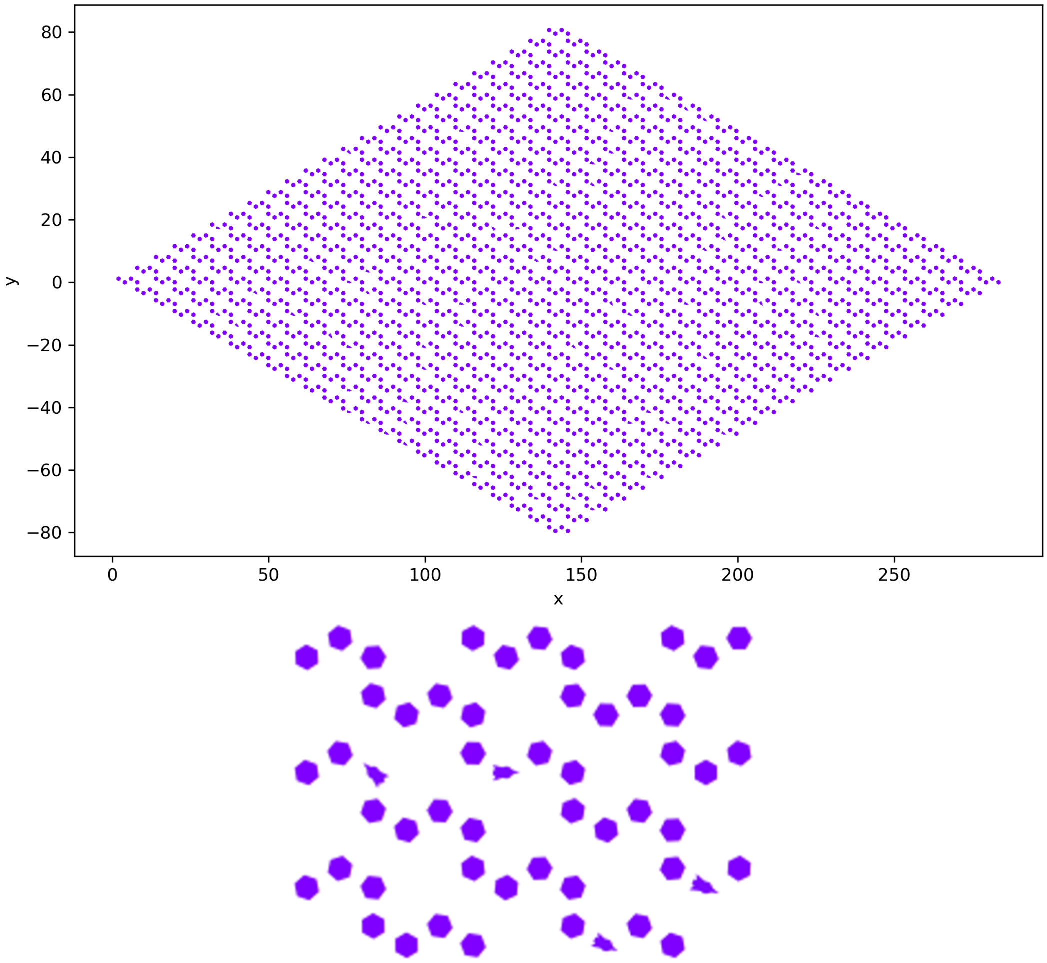

FIGURE 4.6: **Equilibrium spin configuration of a CrI_3 bilayer in the HT-phase.** The top figure contains the spin-lattice for a CrI_3 bilayer in the HT phase. Only the magnetic atoms, i.e. the chromium atoms, are represented in the picture. The figure represents a 24 × 24 × 1 supercell, each unit cell contains four chromium atoms, two in each layer. All spins have a violet colour, this means that all the spins have a downwards out-of-plane orientation. In the bottom figure, we zoomed in on one part of the lattice. Here we see four spins that are canted with respect to the z-direction.

discussions that this means that all the spins have an out-of-plane spin orientation in the downwards direction. This is the case for all the spins in both the upper and bottom layer. This simulation suggests that the HT-bilayer has a FM inter-layer coupling. Remember from the previous chapter that, in the monolayer case, all the atoms were also oriented along the z-axis resulting in a value of zero for the x- and y-components of the magnetization (see section 3.3.2). In contrast, in the HT-bilayer, the magnetization does have a very small but non-zero component in the x- and y-directions. Some spins will be slightly canted with respect to the z-axis resulting in a small in-plane component of the magnetization. This spin canting is due to the non-zero DMI that is present in bilayers which is absent in monolayers due to the symmetry of the exchange matrix. Since the DMI is only small, the resulting in-plane magnetization will also be very small. At the bottom of figure 4.6, we zoomed in on the spin lattice so that the canting of the spins becomes visible. Which spins will be canted and which won't is subject to changes from simulation to simulation.

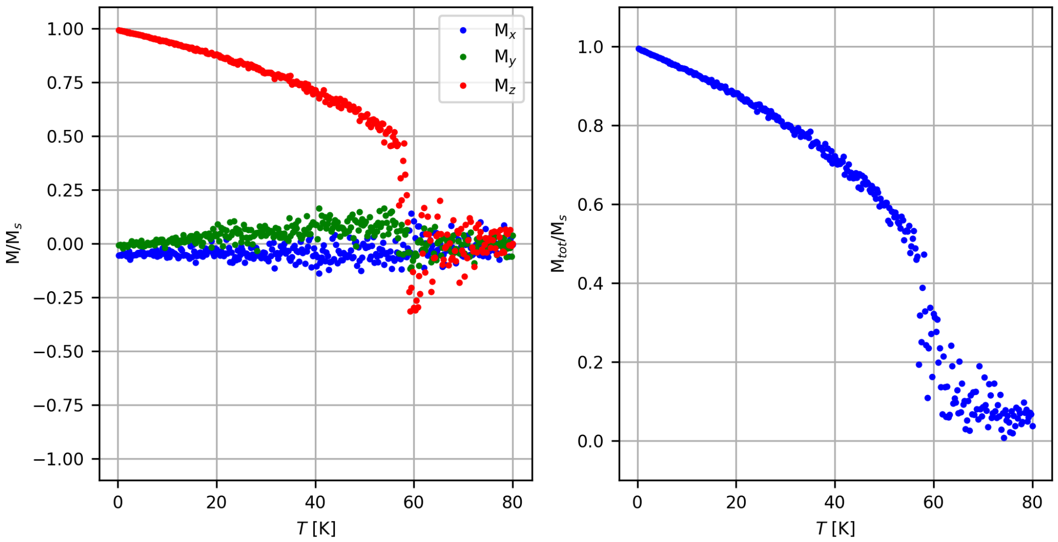

FIGURE 4.7: **Magnetization of a CrI_3 bilayer in the LT-phase, as a function of the temperature.** On the left panel of the figure, the three Cartesian components of the magnetization are depicted as a function of the temperature. The sign of the magnetization denotes the direction of the magnetization relative to the Cartesian axes. On the right panel of the figure, the total magnetization of the system is depicted as a function of the temperature. In both panels, the magnetization is portrayed relative to the saturation magnetization.

The direction in which the spins are canted depends for a large part on the direction of the DMI vector at that specific spin site. Notice that state depicted here is one of many (meta)stable magnetic states of the system. In order to determine the ground-state and other possible (meta)stable states of the system one can resort to other techniques, e.g. molecular dynamics, metropolis algorithm, etc., to probe to entire phase space of the system. Most metastable states will be pretty similar to the one depicted here with pretty uniform magnetization with the exception of a few canted spins. But, since there is some non-zero DMI in the material, there is a slight possibility to find (meta)stable states with a non-trivial spin configuration.

For the LT- and AA-stacked bilayers, we find pretty similar results as for the HT-phase. In both cases, we also found a FM equilibrium state with all the spins pointed in the out-of-plane direction[*]. In the LT-phase, there also is a small in-plane magnetic component caused by spin canting due to the DMI. However, in the AA-layer, this in-plane components of the magnetization is absent. This is due to the crystal symmetry of the AA-bilayer which more closely resembles the symmetry of a monolayer. Due to the weak inter-layer coupling between the layers in an AA-stacked bilayer, the behaviour of each individual layer will resemble that of monolayer.

4.2.3 Curie Temperature

In figures 4.7, 4.8 and 4.9, we depict the magnetization of respectively the LT, HT and AA-bilayer as a function of temperature. On the left panel of each figure, we depict the three Cartesian components of the magnetization as a function of temperature, in

---

[*] In the LT-phase and AA-phases, the spins were pointed in the upwards out-of-plane direction. However, this doesn't really matter since both directions are degenerate. The direction in which the system will end up at is, for the most part, depended on the random initial orientations of the spins at the start of the simulation.

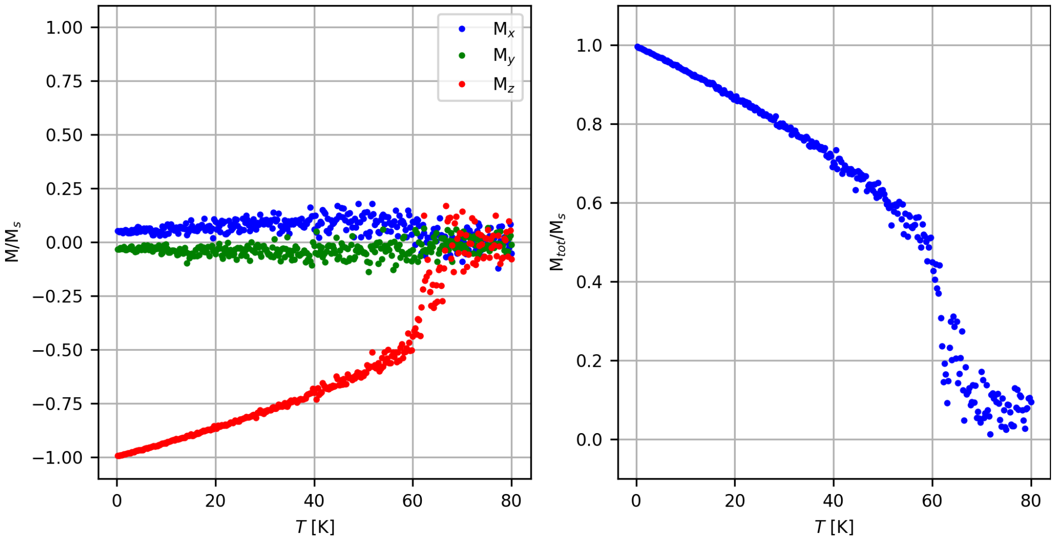

FIGURE 4.8: **Magnetization of a CrI$_3$ bilayer in the HT-phase, as a function of the temperature.** On the left panel of the figure, the three Cartesian components of the magnetization are depicted as a function of the temperature. The sign of the magnetization denotes the direction of the magnetization relative to the Cartesian axes. On the right panel of the figure, the total magnetization of the system is depicted as a function of the temperature. In both panels, the magnetization is portrayed relative to the saturation magnetization.

the right panel, the temperature dependence of the total magnetization is portrayed. All graphs have similar shapes as the magnetization curves of the monolayer. As soon as the temperature decreases below the Curie temperature, the total magnetization and z-component of the magnetization start to increase rapidly. The magnetization keeps increasing with decreasing temperature and finally approaches the saturation magnetization at absolute zero. In the case for the HT-bilayer, the equilibrium spin configuration at $T = 0$ K is shown in figure 4.6 of the previous section. As mentioned earlier, the LT- and AA-bilayers had an opposite magnetization which can be seen from the z-component of the magnetization in figures 4.7 and 4.9 (which is irrelevant since both directions are degenerate). In the monolayer, the x- and y-components of the magnetization converged to zero with decreasing temperature which results in the absence of spin canting. As discussed earlier, there will also be no spin canting in the AA-bilayer since its behaviour resembles that of a monolayer due to the weak inter-layer interaction. In the LT- and HT-phases there clearly are non-zero components to the magnetization in the x- and y-direction caused by spin canting due to the DMI. Further, notice that the Curie temperature of the Lt- and HT-bilayers lies closer to the Curie temperature of bulk CrI$_3$ which is equal to $T_c = 61$ K than to the Curie temperature of the monolayer which our simulations placed at $T_c = 48$ K. The Curie temperatures for the LT, HT and AA-bilayers are respectively 58 K, 61 K and 50 K. The higher Curie temperature of bilayers can be explained by the magnetic exchange interaction which is stronger for bilayers in comparison to monolayers. This stronger interaction is both due to the intra-layer exchange parameters which are bigger in bilayers and because bilayers also have an additional inter-layer interaction. As such, more energy, i.e. a higher temperature, is required to thermally excite the spins. However, the Curie temperature of the AA-bilayer is significantly lower than the temperatures of the other two structures. This is caused by the weaker inter-layer coupling in the AA-bilayer. Due to this weak coupling, the

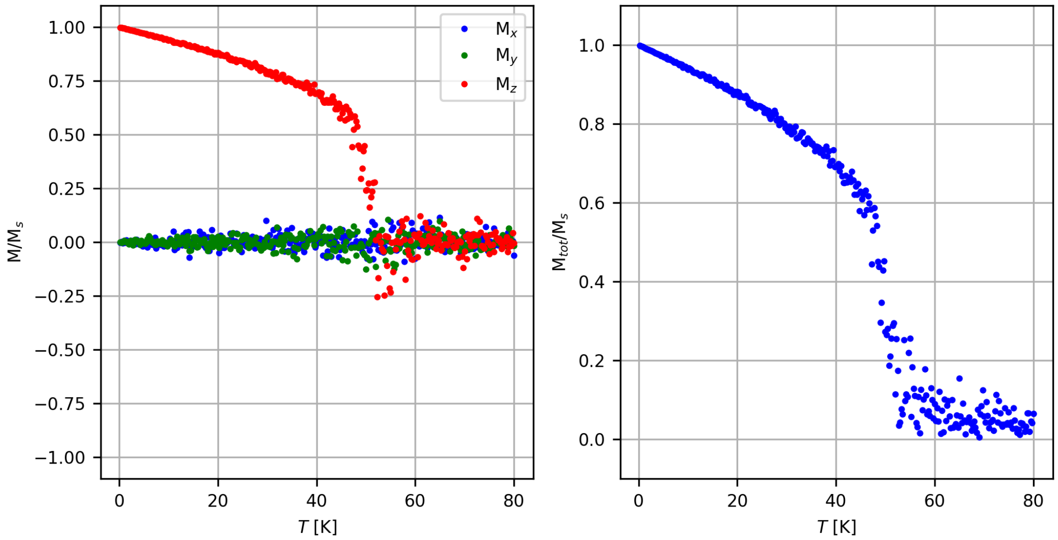

FIGURE 4.9: **Magnetization of a CrI_3 bilayer in the AA-phase, as a function of the temperature.** On the left panel of the figure, the three Cartesian components of the magnetization are depicted as a function of the temperature. The sign of the magnetization denotes the direction of the magnetization relative to the Cartesian axes. On the right panel of the figure, the total magnetization of the system is depicted as a function of the temperature. In both panels, the magnetization is portrayed relative to the saturation magnetization.

behaviour of each individual layer resembles that of a monolayer with only a small additional effect of the inter-layer interaction. The result is that the Curie temperature of the AA-bilayer $T_c = 50$ K is only a little higher than the Curie temperature of the monolayer $T_c = 48$ K.

4.3 Twisted Bilayer

4.3.1 From Layers to Flakes

In this chapter, we will study the influence of the twisting of one of the layers in a CrI_3 bilayer on its magnetic parameters. However, performing 4SM calculations for twisted bilayers is not so straightforward as it may seem. Due to the twisting of the layers, Moiré patterns appear in the structure. There is now additional periodicity in the lattice over a distance of multiple unit cells. To be able to do DFT calculations on a twisted bilayer, we would require a very large supercell which would result in an extremely computationally heavy calculation. Such calculations would have a supercell that contains hundreds of atoms. Given the fact that a 4SM calculation for a regular bilayer already requires several days of calculation time on the best computational infrastructure available at the University of Antwerp (see section A.4 of the appendix for more information), it becomes clear that doing DFT calculations for a twisted bilayer in this way is practically impossible within a reasonable time frame.

However, we can solve this issue by switching our structure from an infinite layer to finite flake. As an example, we show a monolayer flake in figure 4.10. In contrast to the infinite sheet of atoms that is a monolayer, a flake contains a finite number of atoms. We can construct a flake by including vacuum in the unit cell in all directions. By stacking two monolayer flakes on top of each other, we can construct a bilayer flake, and finally, by twisting one of the flakes we obtain the desired structure. In figure 4.11, we show a twisted bilayer flake in the LT-phase with a twisting angle of 3°. Since the twisted bilayer flake contains fewer atoms than the supercell of a regular twisted bilayer, we save a lot of computational resources and can still study the effect of the twist on the magnetism in the material. To validate this approach, we will first do the 4SM calculations for a monolayer flake and a bilayer flake and compare the results with the magnetic parameters from their regular counterparts. The results from this benchmark study can be found in section C of the appendix. Since the method yields relatively accurate results for the regular monolayer and bilayer, we will now apply it to a twisted bilayer.

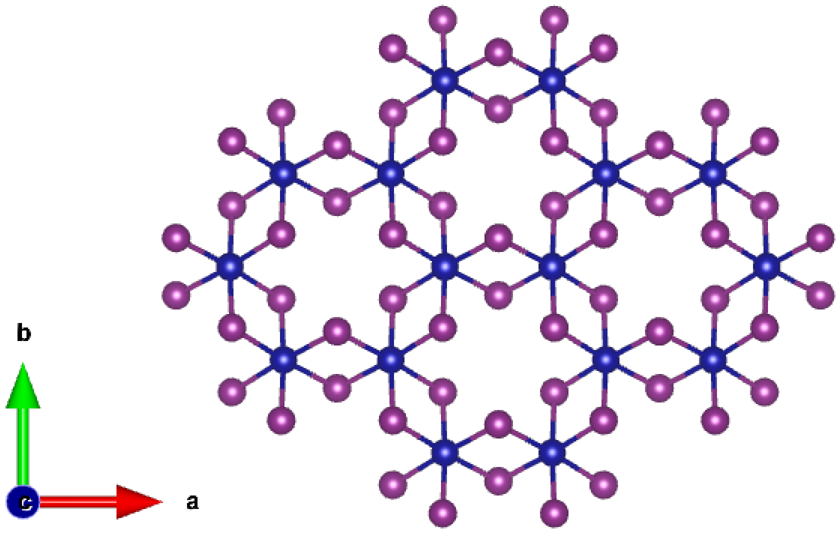

FIGURE 4.10: **Crystal structure of a CrI_3 monolayer flake.** Top view of a flake constructed from a CrI_3 monolayer. Chromium and iodine atoms are represented by blue and purple spheres respectively.

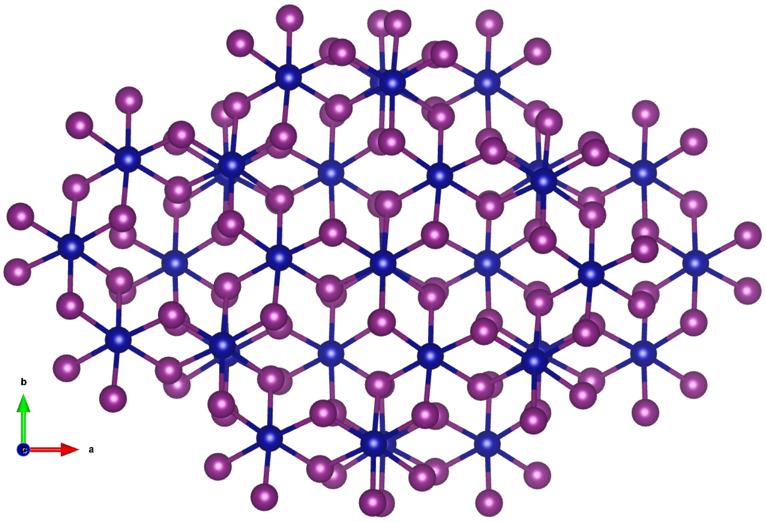

FIGURE 4.11: **Crystal structure of a twisted CrI_3 bilayer flake in the LT-phase.** Top view of a twisted bilayer flake in the LT-phase. The top layer is twisted over 3° in the clockwise direction. Chromium and iodine atoms are represented by blue and purple spheres respectively.

4.3.2 Magnetic Parameters

To study the influence of twisting on the magnetism of CrI_3, we take a bilayer flake in the LT-phase and calculate the exchange parameters for this structure at different twisting angles. We repeat the calculation for both an intra-layer and an inter-layer exchange matrix. The results from these calculations are shown in figure 4.7. The twisting angles gradually increase from 0° to 15° in intervals of 3°. In figure 4.11, we show a twisted bilayer flake in the LT-phase with a twisting angle of 3°.

For a more clear representation of the data, the results from table 4.7 are also plotted in figure 4.12. In the intra-layer case, the diagonal elements of the exchange matrix become more negative with an increasing twisting angle. This means that the

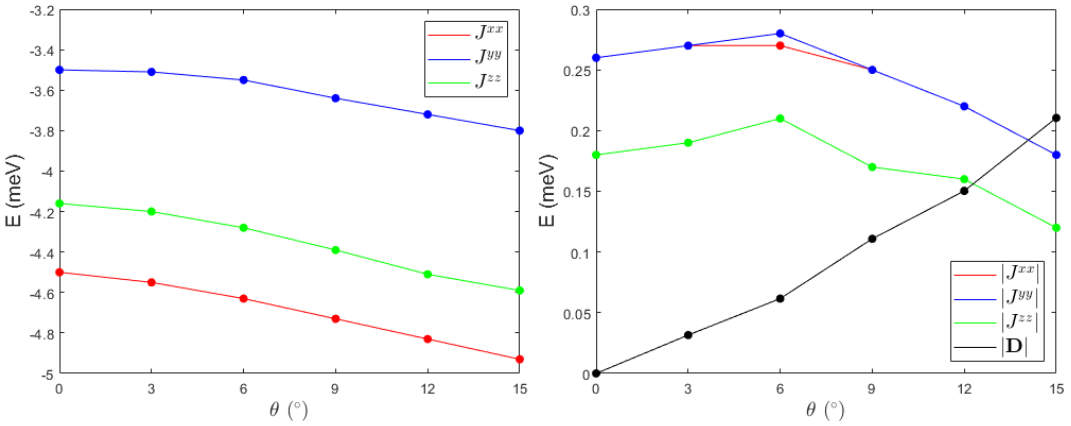

FIGURE 4.12: **Magnetic exchange parameters of a twisted bilayer as a function of the twisting angle.** On the left figure, the diagonal elements of an intra-layer exchange matrix of a twisted LT-bilayer are depicted as a function of the twisting angle. On the right figure, the absolute value of the diagonal elements of an inter-layer exchange matrix and the size of the DMI for this interaction of a twisted LT-bilayer, are depicted as a function of the twisting angle.

TABLE 4.7: **Magnetic exchange parameters of a twisted CrI_3 bilayer in the LT-FM phase.** The table contains the exchange matrices for one intra-layer spin pair and one inter-layer spin pair at different twisting angles.

θ	J_{intra} (meV)			J_{inter} (meV)		
0°	-4.50	-0.02	0.09	-0.26	0.00	0.00
	0.00	-3.50	-0.61	0.00	-0.26	0.00
	-0.13	-0.59	-4.16	0.00	0.00	-0.18
3°	-4.55	-0.03	0.11	-0.27	0.03	0.00
	-0.02	-3.51	-0.63	-0.03	-0.27	-0.01
	-0.13	-0.58	-4.20	0.00	0.02	-0.19
6°	-4.63	-0.03	0.11	-0.27	0.07	0.00
	0.02	-3.55	-0.66	-0.06	-0.28	0.00
	-0.11	-0.59	-4.28	0.01	0.01	-0.21
9°	-4.73	-0.03	0.11	-0.25	0.11	0.01
	-0.01	-3.64	-0.68	-0.10	-0.25	0.00
	-0.07	-0.59	-4.39	0.02	0.02	-0.17
12°	-4.83	-0.03	0.15	-0.22	0.16	0.01
	-0.01	-3.72	-0.68	-0.14	-0.22	0.00
	-0.12	-0.60	-4.51	0.01	-0.02	-0.16
15°	-4.93	-0.05	0.13	-0.18	0.21	0.01
	0.00	-3.80	-0.69	-0.20	-0.18	0.01
	-0.13	-0.59	-4.59	0.03	-0.02	-0.12

intra-layer exchange interaction becomes stronger in a twisted bilayer. We observe a 10%, 8% and 9% increase in interaction strength for respectively the J^{xx}, J^{yy} and J^{zz} parameters. The off-diagonal elements of the remain relatively unchanged after applying the twists. This means that there will not be significant changes in the intra-layer DMI throughout the twisting process.

In the inter-layer case, we see a significant increase in the DMI with each twist of the layer (black line on the right panel of figure 4.12). On the other hand, the diagonal elements of the inter-layer exchange matrix slightly decrease with increasing angle. After an angle of 15°, the DMI even overtakes the exchange interaction as the most dominant interaction between the layers. This can have a significant effect on the spin configuration of the material since, in principle, the inter-layer interaction now favours an orthogonal orientation over a parallel one. Off-course, there is competition between the DMI and both the (also increased) intra-layer exchange and inter-layer exchange which both still try to align the spin parallel. More research is need to be able to draw a definitive conclusion as to which spin textures might appear as (meta)stable states of the system. However, our calculations are able to show that it is possible to tune the DMI in a material by twisting of the layers.

Chapter 5

Conclusion

In this chapter, we will conclude the thesis by summarizing the most important results that were achieved throughout this work and give an outlook on further challenges and opportunities within the field.

Magnetic Parameters

In this thesis, we used the 4SM method in combination with DFT to calculate some magnetic parameters that model the magnetic interactions in CrI_3. Based on these parameters, we can predict the behaviour of the spins in our material. The 4SM analysis of a CrI_3 *monolayer* confirmed some experimental observations of the material's magnetic behaviour. Monolayer CrI_3 is a permanent ferromagnet with strong out-of-plane magnetic anisotropy. This anisotropy is caused by the anisotropy of the exchange matrix in combination with a smaller contribution due to the SIA. The exchange matrix is completely symmetric resulting in zero net DMI which prevents spin canting.

The 4SM method was also applied to CrI_3 *bilayers* in three different stacking orders, namely an AA-stacked bilayer, a bilayer in the LT-phase and a bilayer in the HT-phase. In CrI_3 bilayers, the 4SM calculations showed a FM intra-layer exchange interaction. The exchange parameters for the LT-phase and the HT-phase are bigger than for the monolayer which suggest that the intra-layer exchange interaction is even stronger in these structures. In the AA-bilayer, the difference with the monolayer was smaller. All three bilayers also showed a FM inter-layer coupling. The inter-layer exchange parameters for the LT-bilayer and the HT-bilayer had more or less the same value, the inter-layer parameters for the AA-layer were smaller. The latter is possibly due to the bigger inter-layer distance in the AA-bilayer which results in a smaller overlap of the atomic orbitals and consequently a weaker interaction. In all three the layers, the inter-layer exchange interaction was significantly smaller than the intra-layer exchange interaction. The fact that this interaction is small means that it should be relatively easy to manipulate the inter-layer coupling, e.g. by applying electric and/or magnetic fields, which creates opportunities for applications. The magnetic anisotropy is still caused by the anisotropy of the exchange matrix with an additional smaller contribution due to the SIA. The latter showed similar values in all the bilayers and in the monolayer. In the bilayers, there was a non-zero contribution due to the DMI which allows for canting of the spins. This could possibly lead to some interesting non-trivial (meta)stable states of the system. Future research should investigate this claim by probing the entire phase space of the system. Overall, the results for the bilayers were in relatively good agreement with our expectations and experimental results. A sole exception is the inter-layer coupling of the HT-bilayer which was observed to be AFM in experiments. To address this, other methods to calculate the exchange parameters should be consulted to confirm the validity of the 4SM method to calculate these parameters. Further more, the influence of several DFT parameters on the magnetic parameters should be more thoroughly investigated to pinpoint possible discrepancies. Another possibility is that the Heisenberg model used in this thesis is incomplete, in future calculations, the inclusion of other terms in the Heisenberg Hamiltonian, e.g. the biquadratic exchange or magnetic dipole interaction, or the inclusion of the current interactions for the next nearest neighbours, should be considered.

In this thesis, we showed that it is possible to tune the magnetic parameters in a CrI_3 bilayer by twisting one of the layers. We proved this for a LT-bilayer. The intra-layer exchange got stronger with increasing twisting angle. On the other hand, the inter-layer exchange got weaker while the inter-layer DMI got stronger with increasing twisting angle. At an angle of 15° the DMI even overtook the exchange as the dominant inter-layer interaction. This effect creates the possibility for interesting spin configurations in the material. However, further research is required to confirm and quantify this effect.

Tunability of magnetic properties is currently a hot topic within the field. Earlier tuning methods that have been investigated include: introduction of lattice defects, applying strain and applying electric and/or magnetic fields, among others. In this thesis, we demonstrated that stacking and twisting of the layers are also valid ways to engineer the properties of a material. The exploration of how these tuning methods influence the material properties could lead to interesting new physics. Especially the tuning of DMI could lead to new interesting spin textures. With respect to devices, one challenge that is still unsolved is to develop techniques that can switch the inter-layer coupling at zero applied magnetic field. Further, we should develop a very good understanding of how we can store information in magnets by manipulation of their magnetic states.

Curie Temperature

Another property that we determined in this work is the Curie temperature of our materials. These temperatures can be consulted in table 5.1. For the monolayer, we found a Curie temperature of 48 K which is in pretty good agreement with the experimentally observed Curie temperature of 45 K. For the LT- and HT- bilayer we found Curie temperatures of respectively 58 K and 61 K. These lie both pretty close to the Curie temperature of bulk CrI_3 which is also experimentally observed to be 61 K. The Curie temperature for the AA-stacked bilayer is equal to 50 K which lies closer to the value for the monolayer than to the values for the other bilayers. This is due the weak inter-layer coupling in this structure. The two layers will more or less behave themselves as individual monolayers with an additional small contribution

TABLE 5.1: **Curie temperatures of the different structures that were investigated in this thesis.** The Curie temperatures were calculated for a CrI_3 monolayer, an AA-stacked bilayer, a LT-phase bilayer and a HT-phase bilayer.

Structure	T (K)
Monolayer	48
AA-Bilayer	50
LT-Bilayer	58
HT-Bilayer	61

due to the inter-layer coupling. For the same reason there was also no spin canting observed in the AA-bilayer. The presence of an inter-layer exchange interaction, thus, has a significant influence on the Curie temperature of the systems.

Although CrI_3 definitely has interesting properties, its relatively low Curie temperature can be a problem for the inclusion in realistic applications. A current challenge in the field of 2D magnetism is to identify other materials to have similar interesting properties but a higher Curie temperature. Possible candidates could be $MnSe_2$ or VSe_2, two materials that show intrinsic 2D magnetism at room-temperature.

Spin Waves

Finally, 2D magnetic materials have drawn a lot of attention for how spin waves behave themselves in these materials. CrI_3 shows spin wave modes in the THz regime, a part of the spectrum that had not been utilized yet. In future research, the goal will be to develop a very thorough understanding of how we can manipulate spin waves in these materials. In this regard, magnonic crystals are an interesting topic as they can create a bandgap in the spin wave spectrum. Further, we should try to extend the study of spin waves from magnetic monolayers to multilayers. A next challenge could be to try to determine the dispersion relation in a CrI_3 bilayer. Also, the interaction between spin waves and materials with a non-zero DMI is something that requires more research. The propagation of spin waves in a material can be influenced by the presence of DMI in the material.

Appendix A

Computational Details (DFT)

The ab initio calculations done in this thesis were performed entirely within the DFT formalism using the VASP software[52–54]. We thoroughly discuss DFT in section 2.2. In this part of the appendix, we summarize some important settings and parameters used in our calculations, and give a short overview of the available computational resources.

A.1 Structural Calculations

As discussed in section 2.2.5, we use the conjugate gradient algorithm[60] to relax the ions in our system. The unit cell shape and volume are kept constant during the optimizations, only the atomic positions are allowed to change.

All structural relaxations are executed using a GGA functional and the PAW method[58]. We opt for the PBE exchange-correlation functional[51], with the D2 method of Grimme to account for the vdW correction term[65]. A term due to the SOC is added ad hoc. Since the system contains localized (strongly correlated) d-electrons, we implement the GGA+U method in the form proposed by Dudarev et al.[66]. We add an on-site Coulomb interaction of U = 3.9 eV and J = 1.1 eV to the d-orbitals of the chromium atoms. The energy convergence criterion between two successive electronic iterations is set at 10^{-7} eV. Consequently, the convergence criterion between two successive ionic steps is 10^{-6} eV. For the electronic minimisation, we set ALGO = Fast in the INCAR file. This setting uses the Davidson iteration scheme for the first step in the minimization loop, and afterwards switches to the RMM-DIIS algorithm[59]. Due to the fact that our material is magnetic, we perform spin polarised calculations (collinear). Since we're also interested in magnetic anisotropies, we recommend setting the GGA_COMPAT tag to False in the INCAR file, this will prevent the automatic restoration of the full lattice symmetry that might be broken by the magnetic anisotropy. The plane-wave cut-off is set at 700 eV.

For the regular CrI_3 monolayer and bilayer, the Brillouin zone integration is done over a 15 × 15 × 1 uniform Gamma-centred Monkhorst-Pack grid[57], with a Gaussian smearing of 0.01 eV. To construct a 2D crystal structure, we implement a unit cell height of 15 Å in the out-of-plane direction for the monolayer, and 26 Å for the bilayer, to make sure we got enough vacuum in the unit cell.

For all flake relaxations, we use a 1 × 1 × 1 grid for our k-point sampling since flakes don't have periodicity in either direction. We use a Gaussian smearing of 0.01 eV. Naturally, the lack of periodicity obliges us to include vacuum in all directions of the unit cell. In all flakes, we use the length of the flake plus an additional 10 Å of vacuum as the unit cell sizes in both the x- and y-direction. In the z-direction, we again use a unit cell height of 15 Å for monolayer flakes, and 26 Å for bilayer flakes.

A.2 Electronic Property Calculations

Before we can study the electronic properties of a system (DOS and band structure), we first need to relax the system's crystal structure and use the optimized geometry as an input in the subsequent calculations. Further, we perform a single point calculation on the optimized geometry to generate the charge density (written to the CHGCAR file) that is also used as an input in the subsequent calculations.

In the DOS and band structure calculations, we use a GGA functional and the PAW method[58]. We opt for the PBE exchange-correlation functional[51], with the D2 method of Grimme to account for the vdW correction term[65]. A term due to the SOC is added ad hoc. Since the system contains localized (strongly correlated) d-electrons, we implement the GGA+U method in the form proposed by Dudarev et al.[66]. We add an on-site Coulomb interaction of U = 3.9 eV and J = 1.1 eV to the d-orbitals of the chromium atoms. The energy convergence criterion between two successive electronic iterations is set at 10^{-7} eV. For the electronic minimisation, we set ALGO = Fast in the INCAR file. This setting uses the Davidson iteration scheme for the first step in the minimization loop, and afterwards switches to the RMM-DIIS algorithm[59]. Due to the fact that our material is magnetic, we perform spin polarised calculations (collinear). Since we're also interested in magnetic anisotropies, we recommend setting the GGA_COMPAT tag to False in the INCAR file, this will prevent the automatic restoration of the full lattice symmetry that might be broken by the magnetic anisotropy. The plane-wave cutoff is set at 700 eV.

For the DOS calculation, we choose a $24 \times 24 \times 1$ grid for our k-point sampling. We use a Gaussian smearing of 0.01 eV. The DOS is evaluated on 2000 gridpoints.

We perform the band structure calculations along the Γ-M-K-Γ high-symmetry directions of the first Brillouin zone. We use a Gaussian smearing of 0.02 eV.

A.3 Four-State Mapping Calculations

In 4SM calculations, we want to start from a system with optimized geometry. For regular monolayers and bilayers, we just use the relaxed structure like usual. For flake systems, we manually construct the flakes from the corresponding relaxed monolayer and bilayer structures.

In 4SM calculations, all magnetic moments are aligned along a specific axis as explained in section 2.1. In most calculations (e.g. monolayers, monolayer flakes and bilayers), we use the constrained local moment approach. This means that we add a so called penalty contribution that constrains the magnetic moments in a specified direction. The weight of this penalty term in the total Hamiltonian is set as LAMBDA = 10. For bilayer flakes, we use a slightly different approach. The calculation is performed in two steps. In a first step, we constrain not only the direction, but also the size of the spins and perform a calculation to generate a WAVECAR file. In a second step, we start from this WAVECAR file and perform a calculation like for the regular bilayer where only the direction of the spins is constrained.

In 4SM calculations, we use a GGA functional and the PAW method[58]. We opt for the PBE exchange-correlation functional[51], with the D2 method of Grimme to account for the vdW correction term[65]. A term due to the SOC is added ad hoc. Since the system contains localized (strongly correlated) d-electrons, we implement the GGA+U method in the form proposed by Dudarev et al.[66]. We add an on-site Coulomb interaction of U = 3.9 eV and J = 1.1 eV to the d-orbitals of the chromium atoms. The energy convergence criterion between two successive electronic iterations is set at 10^{-7} eV. Consequently, the convergence criterion between two successive ionic steps is 10^{-6} eV. For the electronic minimisation, we set ALGO = Fast in the INCAR file. This setting uses the Davidson iteration scheme for the first step in the minimization loop, and afterwards switches to the RMM-DIIS algorithm[59]. Due to the fact that our material is magnetic, we perform spin polarised calculations (non-collinear). Since we're also interested in magnetic anisotropies, we recommend setting the GGA_COMPAT tag to False in the INCAR file, this will prevent the automatic restoration of the full lattice symmetry that might be broken by the magnetic anisotropy. The plane-wave cutoff is set at 700 eV for monolayers and monolayer flakes and to 300 eV for bilayers and bilayer flakes.

In 4SM calculations on monolayers and bilayers, the number of k-points for the Brillouin zone integration is reduced to a $3 \times 3 \times 1$ grid to limit the calculation time. For flakes, we need to use a $1 \times 1 \times 1$ grid due to the lack of periodicity in all directions.

A.4 Computational Resources and Parallelization

The DFT calculations were performed on the *Leibniz* and *Vaughan* High-performance computing (HPC) clusters of the university of Antwerp. Leibniz (2017) is a NEC system consisting of 152 nodes with dual 14-core Intel E5-2680v4 Broadwell generation CPUs connected through an EDR InfiniBand network. Vaughan (2020) is a NEC system consisting of 152 nodes with two 32-core AMD Epyc 7542 generation CPUs connected through an HDR100 InfiniBand network. More information about these HPC clusters can be found in the documentation of the vlaams supercomputing center (VSC)[47].

The multicore architecture of clusters like Leibniz and Vaughan is ideal for parallel computing. The VASP software offers an option for parallelization over energy bands through the NPAR tag. This tag specifies the number of energy bands that should be treated in parallel. A good choice for NPAR can significantly reduce the required time for a certain calculation. Calculating multiple energy bands at the same time will reduce the required computational time, however, one should avoid the spread of a single band calculation over cores from multiple nodes, communication between different nodes will slow down the calculation. At the same time, one should always try to use all the cores of the reserved nodes as efficiently as possible, i.e. use all cores on a reserved node on any given time (remember that a node is always reserved in its entirety for one and only one user). One should always assign a certain amount of cores to a simulation so that the job scheduler can efficiently fill nodes entirely with only your jobs. Also, one should pick NPAR depending on the total number of nodes/cores you assigned to a single simulation. Usually, NPAR is chosen in such a way that the number of cores used to calculate one energy band is a divisor of the total number of cores on a node.

Appendix B

Computational Details (Spin Dynamics)

In this thesis, we study the dynamics of the spins in materials by solving the LLG equation. These calculations were done by using the Spirit magnetism simulation framework[61]. Spirit is an open-source C++ code with a Python API. The code solves the LLG equation numerically in a series of steps. To achieve a sufficiently converged result, we advice using at least 500 steps in this process. A second parameter that has an important influence on the convergence of the system is the size of the supercell. For the systems we investigated, a supercell containing $24 \times 24 \times 1$ unit cells suffices to get good results. One unit cell contains two chromium atoms in the monolayer case, and four chromium atoms in the bilayer case (two atoms in each layer). In most calculations, the damping parameter of LLG equation (2.85) is set equal to $\alpha = 0.001$.

The Spirit framework is a very useful tool to perform temperature dependent magnetic simulations. In a temperature dependent simulation we start from a randomly generated spin configuration at a relatively high temperature and decrease the temperature to absolute zero in a certain amount of steps. In each step, the LLG equation is solved for the spin configuration of the system. This solution is used as the initial configuration in the next step. To get good well-converged results, the steps between two consecutive temperatures can't be too big. For the systems we investigated, steps of 0.25 K were sufficient to achieve good results.

The Spirit code can also be used to study the propagation of spins waves in materials. We artificially create spin wave beams by introducing a sinusoidal in-plane oscillating magnetic field[41]:

$$\mathbf{B}_{\text{input}} = b_0 \sin\left(2\pi f_{\text{in}}\, t\right) \hat{k}, \tag{B.1}$$

that is applied in a narrow rectangular region. In this expression, f_{in} is the input frequency, b_0 the field amplitude and $\hat{k}$ the propagation direction[41]. In our simulations, we choose an amplitude of $b_0 = 0.1$ T and a frequencies between $f_{\text{in}} = 0.4 - 0.8 \times 10^{12}$ Hz. By studying the different Cartesian components of the spins as a function of time t we can study the propagation of spins waves through the material along different directions. The frequency and wavelength of the spin waves can be calulated by fitting a sine function to the osculations in the magnetization[41].

For the implementation of the magnetic parameters in Spirit, we need to diagonalize the exchange matrix. The eigenvalues and eigenvectors of the exchange matrix are used as input in the simulation. The diagonalization is done using the `eig()` function in MATLAB.

Appendix C

Layers Vs. Flakes

To reduce the unit cell size, we opt to perform calculations for the twisted bilayers on twisted flakes and not on actual twisted layers (see section 4.3.1 for more information). To justify this approach, we here list some tables that contain the magnetic parameters of the monolayer and bilayer flakes and compare them with the values for the regular monolayer and bilayer.

C.1 Monolayer

In table C.1, we see that the parameters of the monolayer flake differ a little from the values of the regular monolayer. However, the differences are only relatively small and they result in qualitatively the same behaviour of the spins. The negative diagonal elements assure the FM ground-state of the layer. The matrix is still symmetric which results in zero net DMI. The SIA parameter is still relatively small but negative and, thus, favours an out-of-plane orientation of the spins. These results confirm that the method is valid to qualitatively study the magnetism in monolayers.

TABLE C.1: **Comparison of the magnetic parameters of a monolayer CrI_3 flake and a regular monolayer.** Both the exchange matrix and the SIA parameter are depicted in the table.

	Layer			Flake		
	-4.34	0.00	0.00	-4.20	0.00	0.00
J_{i-j} (meV)	0.00	-3.24	-0.65	0.00	-3.07	-0.54
	0.00	-0.65	-3.96	0.00	-0.54	-3.63
A_{ii}^{zz} (meV)	-0.08			-0.13		

C.2 Bilayer

In table C.2, we list the magnetic parameters for one intra-layer spin pair and one inter-layer spin pair for both an LT- and an HT-bilayer flake in the FM phase. The latter since the Spirit calculations performed in chapter 4 suggest a FM ground-state for both phases. Just like for the monolayer, the parameters for the flakes differ only a little from the parameters of the regular bilayers. Therefore, the flakes will display qualitatively the same magnetic behaviour as the regular bilayers. All diagonal elements are still negative which indicates a FM interaction between the spins. Further, the off-diagonal elements also remain rather small, consequently, the DMI in the flakes will have more or less the same magnitude as in the regular bilayers. In all flakes, the SIA will be close to zero. This means that the SIA has no preferential direction for the spins. This is not a big issue since, as we've discussed earlier, the

TABLE C.2: **Comparison of the magnetic parameters of bilayer CrI$_3$ flakes and a regular bilayers.** Both the exchange matrix and the SIA parameter are depicted in the table. For both the LT- and the HT-phase, we compare the magnetic parameters that correspond to one intra-layer and one inter-layer interaction.

		Layer			Flake		
LT-phase		-4.61	0.00	0.12	-4.50	-0.02	0.09
	J_{intra} (meV)	0.05	-3.53	-0.64	0.00	-3.50	-0.61
		-0.12	-0.64	-4.23	-0.13	-0.59	-4.16
	A_{ii}^{zz} (meV)	-0.07			0.00		
		-0.26	0.06	0.01	-0.26	0.00	0.00
	J_{inter} (meV)	0.06	-0.27	0.01	0.00	-0.26	0.00
		0.02	0.01	-0.30	0.00	0.00	-0.18
	A_{ii}^{zz} (meV)	-0.07			0.00		
HT-phase		-4.61	0.00	0.12	-4.50	0.00	0.11
	J_{intra} (meV)	0.05	-3.53	-0.64	0.06	-3.42	-0.59
		-0.12	-0.65	-4.23	-0.12	-0.61	-4.09
	A_{ii}^{zz} (meV)	-0.07			-0.01		
		-0.26	-0.03	-0.05	-0.26	-0.02	-0.04
	J_{inter} (meV)	-0.06	-0.31	-0.02	-0.05	-0.31	-0.03
		0.00	0.06	-0.29	-0.01	0.05	-0.28
	A_{ii}^{zz} (meV)	-0.07			0.01		

anisotropy in the exchange interaction is the main source for the magnetic anisotropy in the system and not the SIA. These results confirm that the use of flakes is a valid approach for a qualitative study of the magnetic behaviour of bilayers and twisted bilayers.

Appendix D

Force Estimations

In section 2.2.1, we discussed the Hamiltonian that is used in our DFT calculations (equation 2.38). We argued that we could neglect several possible contributions to this Hamiltonian based on some simple estimations of forces. In this part of the appendix, we discuss how we obtained these estimations. Unless mentioned otherwise, all physical constants used in this section were looked up from reference [46].

To estimate the *electrostatic force* between a proton and an electron at a distance of 1 Å, we used Coulomb's law:

$$F = k_e \frac{q_1 q_2}{r^2}, \tag{D.1}$$

with a Coulomb constant of $k_e = 8.9875517923 \times 10^9$ N.m^2/C^2. The value of an elementary charge is equal to $e = 1.602176634 \times 10^{-19}$ C, the proton has a charge of $q_1 = +e$, the electron has a charge of $q_2 = -e$. With these values, we find a force of $|\mathbf{F}| = 2.30707755 \times 10^{-8}$ N.

The *gravitational force* between a proton and an electron at a distance of 1 Å was estimated with Newton's law of gravitation:

$$F = G \frac{m_1 m_2}{r^2}, \tag{D.2}$$

in which the gravitational constant is equal to $G = 0.667430 \times 10^{-10}$ N.m^2/kg^2, the mass of the proton is $m_1 = 1.67262192369 \times 10^{-27}$ kg and the mass of the electron is $m_2 = 9.1093837015 \times 10^{-31}$ kg. These inputs give us a value for the gravitational force of $|\mathbf{F}| = 1.0169334 \times 10^{-47}$ N.

The *strong- and weak nuclear interactions* are quite complicated processes and, thus, are way harder to capture in a single formula. We will, however, make some (crude) estimations on the order of magnitude in which these forces operate, by using a formula based on the Yukawa potential. The strong nuclear force between two protons at a distance of 1 Å is estimated by the so called 'nuclear force formula'[67]:

$$F = -H \frac{e^{-r/r_0}}{r^2}. \tag{D.3}$$

The constant pre-factor is equal to $H = 3.4 \times 10^{-26}$ N.m^2, constant r_0 has a value of $r_0 = 1.522 \times 10^{-15}$ m. We refer to reference [67] for more information about the origin of this formula and how the values of the constants were determined. With these input values, we get a force equal to zero, i.e. the result is smaller than 2.229×10^{-308} which is the smallest possible number that can be represented in MS Excel. Typically, the weak nuclear force will be even smaller[44], hence its name, and can, therefore, also be neglected in our Hamiltonian. The strong- and weak nuclear forces become significant only in the femtometer range or smaller[44].

Appendix E

Functional Derivatives

In this part of the appendix, we will briefly introduce the concept of *functional derivatives*. A functional can be thought of as a function takes one or more other functions as an argument. In contrast, a function takes one or more variables as an argument. We can extend this analogy to derivatives. A functional can be differentiated with respect to a function, just like a function can be differentiated with respect to a variable. The functional derivative of a functional F that depends on a function f can be defined as[43]:

$$\frac{\delta}{\delta f(x)} F[f(x)] = \lim_{\delta f(x) \to 0} \frac{F[f(x) + \delta f(x)] - F[f(x)]}{\delta f(x)}. \tag{E.1}$$

This definition is very similar to the definition of the derivative of a function. If we differentiate a functional F with respect to a variable x, we get[43]:

$$\frac{dF}{dx} = \int \frac{\delta F}{\delta f} \frac{df}{dx} df. \tag{E.2}$$

In the special case were $F = f$, this expression reduces to[43]:

$$\frac{df}{dx} = \int \frac{\delta f}{\delta f'} \frac{df'}{dx} df'. \tag{E.3}$$

This equation can be valid if and only if[43]:

$$\frac{\delta f}{\delta f'} = \delta(f - f'), \tag{E.4}$$

where $\delta(f - f')$ is a Dirac-delta function and, thus, not to be confused with the use of the greek letter δ in the notation of a functional derivative. This last identity is very useful, and has also been used in section 2.2.3 of chapter 2. For instance, to obtain expression (2.63), we implicitly did:

$$\begin{aligned} \frac{\delta}{\delta \rho(\mathbf{r})} \int V_{\text{ext}}(\mathbf{r}') \rho(\mathbf{r}') d\mathbf{r}' &= \int V_{\text{ext}}(\mathbf{r}') \frac{\delta \rho(\mathbf{r}')}{\delta \rho(\mathbf{r})} d\mathbf{r}' \\ &= \int V_{\text{ext}}(\mathbf{r}') \delta(\mathbf{r}' - \mathbf{r}) d\mathbf{r}' \\ &= V_{\text{ext}}(\mathbf{r}) \end{aligned} \tag{E.5}$$

In that same expression, we did exactly the same for the other terms.

Bibliography

[1] K. S. Novoselov et al. “Electric Field Effect in Atomically Thin Carbon Films”. In: *Science* ***306****, 666* (2004).

[2] M. Xu et al. “Graphene-Like Two-Dimensional Materials”. In: *Chem. Rev.* ***113****, 3766* (2013).

[3] S. Z. Butler et al. “Progress, Challenges, and Opportunities in Two-Dimensional Materials Beyond Graphene”. In: *ACS Nano* ***7****, 2898* (2013).

[4] K. F. Mak et al. “Probing and Controlling Magnetic States in 2D Layered Magnetic Materials”. In: *Nat. Rev. Phys.* ***1****, 646* (2019).

[5] N. D. Mermin and H. Wagner. “Absence of Ferromagnetism or Antiferromagnetism in One- or Two-Dimensional Isotropic Heisenberg Models”. In: *Phys. Rev. Lett.* ***17****, 1133* (1966).

[6] M. A. McGuire et al. “Coupling of Crystal Structure and Magnetism in the Layered, Ferromagnetic Insulator CrI_3”. In: *Chem. Mater.* ***27****, 612* (2015).

[7] J. L. Lado and J. Fernández-Rossier. “On the Origin of Magnetic Anisotropy in Two-Dimensional CrI_3”. In: *2D Mater.* ***4****, 035002* (2017).

[8] B. Huang et al. “Layer-Dependent Ferromagnetism in a van der Waals Crystal Down to the Monolayer Limit”. In: *Nature* ***546****, 270* (2017).

[9] J. Kerr. “On Rotation of the Plane of Polarization by Reflection from the Pole of a Magnet”. In: *Lond. Edinb. Dublin Philos. Mag. J. Sci.* ***3****, 321* (1877).

[10] N. Samarth. “Magnetism in Flatland”. In: *Nature* ***546****, 216* (2017).

[11] D. Zhong et al. “Van der Waals Engineering of Ferromagnetic Semiconductor Heterostructures for Spin and Valleytronics”. In: *Sci. Adv.* ***3****, e1603113* (2017).

[12] S. Jiang et al. “Spin Tunnel Field-Effect Transistors Based on Two-Dimensional van der Waals Heterostructures”. In: *Nature Electronics* ***2****, 159–163* (2019).

[13] D. J. O’Hara et al. “Room-Temperature Intrinsic Ferromagnetism in Epitaxial Manganese Selenide Films in the Monolayer Limit”. In: *Nano Lett.* ***18****, 3125* (2018).

[14] M. Bonilla et al. “Strong Room-Temperature Ferromagnetism in VSe_2 Monolayers on van der Waals Substrates”. In: *Nature Nanotechnology* ***13****, 289* (2018).

[15] A. K. Geim and I. V. Grigorieva. “Van der Waals Heterostructures”. In: *Nature* ***499****, 419–425* (2013).

[16] Q. Tong et al. “Skyrmions in The Moiré of van der Waals 2D Magnets”. In: *Nano Lett.* ***18****, 7194–7199* (2018).

[17] Encyclopaedia Britannica. *Moiré Pattern*. Consulted on 26/02/2021. URL: `https://www.britannica.com/science/moire-pattern`.

[18] Y. Cao et al. “Unconventional Superconductivity in Magic-Angle Graphene Superlattices”. In: *Nature* ***556****, 43* (2018).

[19] M. Andelkovic et al. “Double Moiré with a Twist: Supermoiré in Encapsulated Graphene”. In: *Nano Lett.* ***20****, 979* (2020).

[20] Jarillo-Herrero Group: Quantum Nanoelectronics @ MIT. *Research: Quantum Transport in Magic-Angle Graphene*. Consulted on 27/02/2021. URL: `http://jarilloherrero.mit.edu/research`.

[21] S. Blundell. *Magnetism in Condensed Matter*. Oxford University Press, 2001.

[22] J.M.D. Coey. *Magnetism and Magnetic Materials*. Cambridge University Press, 2009.

[23] M. Opel. “Spintronic Oxides Grown by Laser-MBE”. In: *J. Phys. D: Appl. Phys.* ***45****, 033001* (2012).

[24] I. E. Dzialoshinskii. “Thermodynamic Theory of "Weak" Ferromagnetism in Antiferromagnetic Substances”. In: *Sov. Phys. JETP* **5***, 1259* (1957).

[25] T. Moriya. “Anisotropic Superexchange Interaction and Weak Ferromagnetism”. In: *Phys. Rev.* ***120****, 91* (1960).

[26] X. Lu et al. “Meron-Like Topological Spin Defects in Monolayer $CrCl_3$”. In: *Nat. Commun.* ***11****, 4724* (2020).

[27] A. K. Behera et al. “Magnetic Skyrmions in Atomic Thin CrI_3 Monolayer”. In: *Appl. Phys. Lett.* ***114****, 232402* (2019).

[28] T. H. R. Skyrme. “A Unified Field Theory of Mesons and Baryons”. In: *Nucl. Phys.* ***31****, 556* (1962).

[29] A. Fert et al. “Skyrmions on the Track”. In: *Nature Nanotechnology* **8***, 152* (2013).

[30] G. Yin et al. “Topological Charge Analysis of Ultrafast Single Skyrmion Creation”. In: *Phys. Rev. B* **93***, 174403* (2016).

[31] Y. Tikhonov et al. “Controllable Skyrmion Chirality in Ferroelectrics”. In: *Sci. Rep.* ***10****, 8657* (2020).

[32] W. Jiang et al. “Skyrmions in Magnetic Multilayers”. In: *Phys. Rep.* ***704****, 1* (2017).

[33] S. Zhang et al. “Topological Computation Based on Direct Magnetic Logic Communication”. In: *Sci. Rep.* **5***, 15773* (2015).

[34] Z. Wu et al. “Strain-Tunable Magnetic and Electronic Properties of Monolayer CrI_3”. In: *Phys. Chem. Chem. Phys.* **21***, 7750* (2019).

[35] M. Pizzochero. “Atomic-Scale Defects in the Two-Dimensional Ferromagnet CrI_3 from First Principles”. In: *J. Phys. D: Appl. Phys.* **53***, 244003* (2020).

[36] F. Matsukura et al. “Control of Magnetism by Electric Fields”. In: *Nature Nanotechnology* ***10****, 209* (2015).

[37] S. Jiang et al. “Controlling Magnetism in 2D CrI_3 by Electrostatic Doping”. In: *Nature Nanotechnology* ***13****, 549* (2018).

[38] J. S. Moodera et al. “The Phenomena of Spin-Filter Tunnelling”. In: *J. Phys.: Condens. Matter* ***19*** *165202* (2007).

[39] IBM. *Racetrack Memory: The Future of Data Storage*. Consulted on 20/03/2021. URL: `https://www.ibm.com/ibm-/history/ibm100/us/en/icons/racetrack/`.

[40] W. Jin et al. “Raman Fingerprint of Two Terahertz Spin Wave Branches in a Two-Dimensional Honeycomb Ising Ferromagnet”. In: *Nature Communications* ***9****, 5122* (2018).

[41] R. M. Menezes et al. "Tailoring High Frequency Magnonics in Two-dimensional Chromium Trihalides". In: *Article hasn't been published yet.* (2021).

[42] D. Sabani et al. "Ab initio Methodology for Magnetic Exchange Parameters: Generic Four-State Energy Mapping on Heisenberg Spin Hamiltonian". In: *Phys. Rev. B* ***102****, 014457* (2020).

[43] M. Springborg. *Methods of Electronic Structure Calculations. From Molecules to Solids*. Wiley & Sons Ltd. (2000).

[44] Hyperphysics. *Fundamental Forces*. Consulted on 09/07/2021. URL: http://hyperphysics.phy-astr.gsu.edu/hbase/Forces/funfor.html#c4.

[45] Wikipedia.org. *Zitterbewegung*. Consulted on 09/07/2021. URL: https://en.wikipedia.org/wiki/Zitterbewegung.

[46] Wikipedia.org. *List of Physical Constants*. Consulted on 07/07/2021. URL: https://en.wikipedia.org/wiki/List_of_physical_constants.

[47] VSC (Vlaams Supercomputing Center). *VSC hardware (2020)*. URL: https://docs.vscentrum.be/en/latest/hardware.html.

[48] V. Y. Pan and Z. Q. Chen. "The Complexity of the Matrix Eigenproblem". In: *STOC '99: Proceedings of the thirty-first annual ACM symposium on Theory of Computing, 507-516* (1999).

[49] Wikipedia.org. *Electronic Correlation*. Consulted on 18/07/2021. URL: https://en.wikipedia.org/wiki/Electronic_correlation.

[50] A. D. Becke. "A New Mixing of Hartree–Fock and Local Density-Functional Theories". In: *J. Chem. Phys.* ***98****, 1372* (1993).

[51] J. P. Perdew et al. "Generalized Gradient Approximation Made Simple". In: *Phys. Rev. Lett.* ***77****, 3865* (1996).

[52] G. Kresse and J. Hafner. "Ab Initio Molecular Dynamics for Liquid Metals". In: *Phys. Rev.* ***47****, 558(R)* (1993).

[53] G. Kresse and J. Furthmüller. "Efficient Iterative Schemes for Ab Initio Total-Energy Calculations Using a Plane-Wave Basis Set". In: *Phys. Rev.* ***54****, 11169* (1996).

[54] G. Kresse and J. Furthmüller. "Efficiency of Ab-Initio Total Energy Calculations for Metals and Semiconductors Using a Plane-Wave Basis Set". In: *Comput. Mat. Sci.* ***6****, 15* (1996).

[55] C. Kittel. *Introduction to Solid State Physics*. John Wiley and Sons Inc., New York (1986).

[56] W. Setyawan and S. Curtarolo. "High-Throughput Electronic Band Structure Calculations: Challenges and Tools (Appendix)". In: *Comp. Mat. Sci. B* ***49****, 299* (2010).

[57] H. J. Monkhorst and J. D. Pack. "Special Points for Brillouin-Zone Integrations". In: *Phys. Rev. B* ***13****, 5188* (1976).

[58] P. E. Blöchl. "Projector Augmented-Wave Method". In: *Phys. Rev. B* ***50****, 17953* (1994).

[59] P. Pulay. "Convergence Acceleration of Iterative Sequences. The Case of SCF Iteration." In: *Chem. Phys. Lett.* ***73****, 393* (1980).

[60] W. H. Press et al. *Numerical Recipes*. Cambridge University Press, New York (1986).

[61] G. P. Müller et al. "Spirit: Multifunctional Framework for Atomistic Spin Simulations". In: *Phys. Rev. B* ***99***, *224414* (2019).

[62] C. Bacaksiz et al. "Distinctive Magnetic Properties of CrI_3 and $CrBr_3$ Monolayers Caused by Spin-Orbit Coupling". In: *Phys. Rev. B* ***103***, *125418* (2021).

[63] L. Webster et al. "Distinct Spin-Lattice and Spin-Phonon Interactions in Monolayer Magnetic CrI_3 (Supporting Documents)". In: *Phys. Chem. Chem. Phys.*, ***20***, *23546-23555* (2018).

[64] P. Jiang et al. "Stacking Tuneable Interlayer Magnetism in Bilayer CrI_3". In: *Phys. Rev. B* ***99***, *144401* (2019).

[65] S. Grimme. "Semiempirical GGA-type Density Functional Constructed With a Long-Range Dispersion Correction". In: *J. Comp. Chem.* **27**, *1787* (2006).

[66] S. L. Dudarev et al. "Electron-Energy-Loss Spectra and the Structural Stability of Nickel Oxide: An LSDA+U Study". In: *Phys. Rev. B* **57**, *1505* (1998).

[67] Thayer Watkins, San José State University (USA). *The Forces Between Protons at Nuclear Distances*. Consulted on 08/07/2021. URL: `https://www.sjsu.edu/faculty/watkins/protonforce.htm`.